

**SUB PERCOLATION THRESHOLD CARBON NANOTUBE BASED  
POLYVINYLIDENE FLUORIDE POLYMER-POLYMER COMPOSITES**

by

Cedric Antony Jacob

A dissertation submitted to the Faculty of the University of Delaware in partial fulfillment of the requirements for the degree of Doctor of Philosophy in Mechanical Engineering

Summer 2015

© 2015 Cedric Antony Jacob  
All Rights Reserved

ProQuest Number: 3730188

All rights reserved

INFORMATION TO ALL USERS

The quality of this reproduction is dependent upon the quality of the copy submitted.

In the unlikely event that the author did not send a complete manuscript and there are missing pages, these will be noted. Also, if material had to be removed, a note will indicate the deletion.



ProQuest 3730188

Published by ProQuest LLC (2015). Copyright of the Dissertation is held by the Author.

All rights reserved.

This work is protected against unauthorized copying under Title 17, United States Code  
Microform Edition © ProQuest LLC.

ProQuest LLC.  
789 East Eisenhower Parkway  
P.O. Box 1346  
Ann Arbor, MI 48106 - 1346

**SUB PERCOLATION THRESHOLD CARBON NANOTUBE BASED  
POLYVINYLIDENE FLUORIDE POLYMER-POLYMER COMPOSITES**

by

Cedric Antony Jacob

Approved: \_\_\_\_\_  
Suresh G. Advani, Ph.D.  
Chair of the Department of Mechanical Engineering

Approved: \_\_\_\_\_  
Babatunde Ogunnaike, Ph.D.  
Dean of the College of Engineering

Approved: \_\_\_\_\_  
James G. Richards, Ph.D.  
Vice Provost for Graduate and Professional Education

I certify that I have read this dissertation and that in my opinion it meets the academic and professional standard required by the University as a dissertation for the degree of Doctor of Philosophy.

Signed:

---

Erik T. Thostenson, Ph.D.  
Professor in charge of dissertation

I certify that I have read this dissertation and that in my opinion it meets the academic and professional standard required by the University as a dissertation for the degree of Doctor of Philosophy.

Signed:

---

Joshua L. Hertz, Ph.D.  
Member of dissertation committee

I certify that I have read this dissertation and that in my opinion it meets the academic and professional standard required by the University as a dissertation for the degree of Doctor of Philosophy.

Signed:

---

Chaoying Ni, Ph.D.  
Member of dissertation committee

I certify that I have read this dissertation and that in my opinion it meets the academic and professional standard required by the University as a dissertation for the degree of Doctor of Philosophy.

Signed:

---

Bingqing Wei, Ph.D.  
Member of dissertation committee



## **ACKNOWLEDGMENTS**

This work was supported in part by the Air Force Office of Scientific Research (AFOSR) Young Investigator Grant (FA9550-09-1-0218), Dr. Byung-Lip Lee, Program Director and the University of Delaware Graduate Fellows program. Additional support was given by CART cooperative agreement (W911NF-07-2-0026).

The 2011 EAPSI program contributed heavily to the simulation efforts through a collaborative agreement between the Korean National Science Foundation and the National Science Foundation. The University Fellows program helped to support graduate work for 2013-2014.

Special thanks goes to Preston McDaniel, Dr. Joseph Dietzel, and Dr. Steve Sauerbrunn their help with the fundamental theory and characterization of polymer chemistry; Dr. Woong Ryeol Yu for his contributions to finite element multiphysics simulation; and Professor David Young for his insight into high voltage physics.

This work would not have been possible without the assistance of Britannia Vondrasek, Peter Hauser, and David Wilson who contributed heavily to the study of electrospinning, and the polymer-polymer composite process through the University of Delaware Undergraduate Research Program.

Finally, the greatest thanks goes to Dr. Erik Thostenson, for his constant support; not only as an advisor and mentor, but as a friend.

## TABLE OF CONTENTS

|                       |       |
|-----------------------|-------|
| LIST OF TABLES .....  | viii  |
| LIST OF FIGURES ..... | ix    |
| ABSTRACT .....        | xviii |

### Chapter

|         |                                                                                                           |    |
|---------|-----------------------------------------------------------------------------------------------------------|----|
| 1       | INTRODUCTION AND MOTIVATION.....                                                                          | 1  |
| 1.1     | The Piezoelectric Effect .....                                                                            | 2  |
| 1.2     | Polyvinylidene Fluoride .....                                                                             | 5  |
| 1.3     | Carbon Nanotube Composites .....                                                                          | 8  |
| 1.4     | Electrospinning.....                                                                                      | 11 |
| 1.5     | Carbon Nanotube-Reinforced Polymer-Polymer Composite Concept....                                          | 13 |
| 1.6     | Motivation .....                                                                                          | 14 |
| 2       | MODELING OF CARBON NANOTUBE REINFORCED<br>PIEZOELECTRIC COMPOSITES USING FINITE ELEMENT<br>ANALYSIS ..... | 16 |
| 2.1     | 2-Dimensional Nanocomposite Model based on COMSOL<br>Mutliphysics .....                                   | 17 |
| 2.2     | 3-Dimensional Modeling of Nanocomposite Piezoelectric<br>Coefficients .....                               | 28 |
| 2.2.1   | Simulation Methodology .....                                                                              | 28 |
| 2.2.1.1 | Pre-Processing Architecture .....                                                                         | 32 |
| 2.2.1.2 | Carbon Nanotube Geometry: Waviness .....                                                                  | 33 |
| 2.2.1.3 | Carbon Nanotube Dispersion, Orientation and Mesh<br>Generation .....                                      | 36 |
| 2.2.1.4 | ANSYS Simulation .....                                                                                    | 38 |
| 2.2.2   | 3-D Simulation Results and Discussion .....                                                               | 40 |
| 2.3     | Conclusions .....                                                                                         | 46 |
| 3       | ELECTROSPINNING PVDF WITH CARBON NANOTUBE<br>REINFORCEMENT.....                                           | 49 |

|         |                                                                         |    |
|---------|-------------------------------------------------------------------------|----|
| 3.1     | Electrospinning with the Mark II System.....                            | 50 |
| 3.1.1   | Materials and Nanotube Dispersion .....                                 | 52 |
| 3.1.2   | Fiber Measurement Methodology .....                                     | 53 |
| 3.2     | Mark II Results and Discussion.....                                     | 54 |
| 3.2.1   | Faraday Tube Effectiveness .....                                        | 54 |
| 3.2.2   | Macro-scale Morphology .....                                            | 57 |
| 3.2.3   | Micro-scale Morphology .....                                            | 58 |
| 3.2.4   | Mark II Conclusions .....                                               | 61 |
| 3.3     | Electrospinning with the Mark III system .....                          | 62 |
| 3.3.1   | Materials and Processing .....                                          | 63 |
| 3.3.2   | Microscopy and Structure Characterization .....                         | 65 |
| 3.3.2.1 | Wide Angle X-Ray Scattering (WAXS) .....                                | 66 |
| 3.3.2.2 | Fourier Transform Infrared Spectroscopy (FTIR).....                     | 67 |
| 3.3.2.3 | Scanning Electron Microscopy (SEM).....                                 | 67 |
| 3.3.2.4 | Differential Scanning Calorimetry (DSC).....                            | 67 |
| 3.3.3   | Mark III Results and Discussion .....                                   | 68 |
| 3.3.3.1 | Polymorphism in Melt and Solution Processed<br>PVDF .....               | 71 |
| 3.3.3.2 | Influence of electrospinning variables on<br>polymorphism of PVDF ..... | 73 |
| 3.3.3.3 | Verification of Results by FTIR .....                                   | 76 |
| 3.4     | Conclusions .....                                                       | 77 |
| 4       | HIGH VOLTAGE CONSIDERATIONS.....                                        | 79 |
| 4.1     | High Voltage Electrical Breakdown.....                                  | 80 |
| 4.2     | Experimental.....                                                       | 82 |
| 4.2.1   | Materials .....                                                         | 82 |
| 4.2.2   | Electrospinning and Composite Processing .....                          | 83 |
| 4.2.3   | Electrical Property Characterization.....                               | 83 |
| 4.2.4   | Microscopy .....                                                        | 86 |
| 4.3     | Results and Discussion .....                                            | 86 |
| 4.3.1   | Corona Discharge and Electrical Surface Tracking .....                  | 86 |

|       |                                                                                           |     |
|-------|-------------------------------------------------------------------------------------------|-----|
| 4.3.2 | Dielectric Breakdown .....                                                                | 97  |
| 4.4   | Conclusions .....                                                                         | 99  |
| 5     | ELECTROSPINNING BASED POLYMER-POLYMER COMPOSITE<br>WITH INTEGRATED CARBON NANOTUBES ..... | 101 |
| 5.1   | Experimental.....                                                                         | 102 |
| 5.1.1 | Materials and Processing .....                                                            | 102 |
| 5.1.2 | Crystal Structure Characterization .....                                                  | 104 |
| 5.1.3 | Electron Microscopy .....                                                                 | 105 |
| 5.1.4 | Mechanical Testing .....                                                                  | 105 |
| 5.2   | Results and Discussion .....                                                              | 106 |
| 5.2.1 | Physical Microstructure .....                                                             | 106 |
| 5.2.2 | Composite Crystal Structure Characterization .....                                        | 113 |
| 5.2.3 | Mechanical Properties .....                                                               | 118 |
| 5.3   | Conclusions .....                                                                         | 121 |
| 6     | CONCLUSIONS AND RECOMMENDATIONS FOR FUTURE WORK ..                                        | 123 |
| 6.1   | Major Conclusions.....                                                                    | 123 |
| 6.2   | Recommendations for Future Work .....                                                     | 125 |
|       | REFERENCES .....                                                                          | 128 |
|       | Appendix                                                                                  |     |
| A     | EQUIPMENT DESIGN .....                                                                    | 135 |
| A.1   | Electrospinning Apparatus .....                                                           | 135 |
| A.2   | High Voltage and Poling .....                                                             | 141 |
| B     | DEVELOPMENT OF COMPUTER VISION FOR FIBER IMAGE<br>ANALYSIS .....                          | 146 |

## LIST OF TABLES

|            |                                                                                     |     |
|------------|-------------------------------------------------------------------------------------|-----|
| Table 1.1: | $\alpha$ , $\beta$ , and $\gamma$ polymorphs of PVDF and their attributes. ....     | 7   |
| Table 2.1  | List of meshing parameters used by ANSYS. ....                                      | 39  |
| Table 3.1  | Mark II electrospinning process conditions .....                                    | 52  |
| Table 3.2  | Processing conditions for solutions. ....                                           | 64  |
| Table 3.3  | Curve fitted $\beta$ fraction values as well as DSC melt onset and melt peaks ..... | 69  |
| Table 5.1  | $\beta$ fraction of the PVDF crystal structure .....                                | 115 |

## LIST OF FIGURES

|             |                                                                                                                                                                                    |    |
|-------------|------------------------------------------------------------------------------------------------------------------------------------------------------------------------------------|----|
| Figure 1.1  | Schematic representation of the basic piezoelectric physics. ....                                                                                                                  | 4  |
| Figure 1.2  | Schematic representation of the electrospinning process.....                                                                                                                       | 12 |
| Figure 2.1  | The fully defined piezoelectric problem with electrical boundary conditions and governing equations. ....                                                                          | 18 |
| Figure 2.2  | Deformation of a neat PVDF with 1V applied voltage and clamped boundary condition.....                                                                                             | 18 |
| Figure 2.3  | Electrical potential plot of carbon nanotubes with a high aspect ratio. Fewer nanotubes are present to keep the total weight-fraction constant.....                                | 20 |
| Figure 2.4  | Electrical potential plot of carbon nanotubes with a low aspect ratio. More nanotubes are present to keep the total weight-fraction constant.....                                  | 20 |
| Figure 2.5  | Influence of mass fraction of carbon nanotubes on the normalized displacement under an electric field.....                                                                         | 21 |
| Figure 2.6  | Influence of carbon nanotube alignment on the normalized displacement under an electric field.....                                                                                 | 22 |
| Figure 2.7  | Influence of carbon nanotube aspect ratio on the normalized displacement under an electric field (constant number of nanotubes). ...                                               | 23 |
| Figure 2.8  | Influence of carbon nanotube aspect on the normalized displacement under an electric field (constant volume fraction).....                                                         | 24 |
| Figure 2.9  | Influence of nanotube orientation on normalized displacement under an electric field (single nanotube). ....                                                                       | 25 |
| Figure 2.10 | Contour plots of electric potential of a single nanotube within a PVDF matrix at different rotations. Boundary conditions are 0V and 10V which set the scale for the contour. .... | 26 |

|             |                                                                                                                                                                                                                                                                                                                                                                                                                                                                                                                                              |    |
|-------------|----------------------------------------------------------------------------------------------------------------------------------------------------------------------------------------------------------------------------------------------------------------------------------------------------------------------------------------------------------------------------------------------------------------------------------------------------------------------------------------------------------------------------------------------|----|
| Figure 2.11 | Electric potential plots of a single various stochastically distributed geometries which resulted in abnormally high normalized displacements (normalized displacement shown under contour plot).....                                                                                                                                                                                                                                                                                                                                        | 27 |
| Figure 2.12 | Illustration of displacement produced on top and bottom surface due to the piezoelectric effect with a heterogeneous electric field. ....                                                                                                                                                                                                                                                                                                                                                                                                    | 31 |
| Figure 2.13 | Schematic description of information flow through software. MATLAB is used in order to fully describe the geometry of both individual carbon nanotubes, and the nanotube dispersion. CATIA then interprets the MATLAB produced description and generates a solid model. ANSYS uses the CATIA-produced model in order to use finite element analysis to calculate the electric field distribution. Lastly, MATLAB is used to interpret each data set and calculate the effect of the electric field on effective piezoelectric strength. .... | 33 |
| Figure 2.14 | Schematic showing the planes and coordinates used for extruding the carbon nanotube solid model. A spline is constructed through points (small squares) which are given as x-y coordinates on a series of planes (large squares) ensuring the nanotube does not twist over itself by restricting it to quarter turns (clockwise or anti-clockwise). b) Screenshot of a CATIA model used as an example of the as produced carbon nanotube solid model.....                                                                                    | 35 |
| Figure 2.15 | Radial histogram showing distribution of angles of each carbon nanotube in the dispersion with the associated standard deviation. A standard deviation of $\pi/16$ gives highly aligned carbon nanotubes and, as it is increased, the quality of the alignment degrades until reaching a standard deviation of $\pi$ , which generates a randomly oriented dispersion.....                                                                                                                                                                   | 37 |
| Figure 2.16 | Example of modeled geometry using a 0.1 wt% of carbon nanotubes with a maximum waviness of 4 times their diameter, an aspect ratio of 32, and fully random orientation. ....                                                                                                                                                                                                                                                                                                                                                                 | 38 |
| Figure 2.17 | Changes in effective piezoelectric coefficient with differing levels of mesh refinement. ....                                                                                                                                                                                                                                                                                                                                                                                                                                                | 39 |
| Figure 2.18 | Examples of electric potential (voltage) in the cross section of simulations with (a) PVDF matrix with fully randomly dispersed carbon nanotubes with an aspect ratio of 4 and a weight percent of 0.1% and (b) changing the aspect ratio to 32 with the same weight percent. ....                                                                                                                                                                                                                                                           | 41 |

|             |                                                                                                                                                                                                                                                                                                                                                                                    |    |
|-------------|------------------------------------------------------------------------------------------------------------------------------------------------------------------------------------------------------------------------------------------------------------------------------------------------------------------------------------------------------------------------------------|----|
| Figure 2.19 | Example of electric potential (voltage) on a cross section of a simulation for PVDF containing 0.1wt% of carbon nanotubes with a maximum waviness of 3 times the nanotube diameter.....                                                                                                                                                                                            | 41 |
| Figure 2.20 | Effective $d_{33}$ as influenced by aspect ratio with a weight percent of 0.1%, constant nanotube diameter, and fully unaligned dispersion. An increase can be seen as the aspect ratio becomes smaller and the number of carbon nanotubes increases.....                                                                                                                          | 42 |
| Figure 2.21 | Effective $d_{33}$ plotted against carbon nanotube (carbon nanotube) content in weight percent with constant aspect ratio and fully unaligned dispersion. An increase in carbon nanotube content (and number of carbon nanotubes) produces an increase in effective $d_{33}$ .....                                                                                                 | 43 |
| Figure 2.22 | Effective $d_{33}$ plotted against carbon nanotube in-plane orientation with constant weight percent and constant aspect ratio. Orientation is given as the standard deviation of carbon nanotube angles. ....                                                                                                                                                                     | 44 |
| Figure 2.23 | Waviness, as a ratio of amplitude to carbon nanotube diameter, is plotted from 1 to 4 with constant weight percent, constant cap-to-cap distance, and completely random dispersion.....                                                                                                                                                                                            | 44 |
| Figure 2.24 | Example of a transversely oriented spanning cluster demonstrating what happens if a carbon nanotube agglomerate exists in the film (a typical problem when solution casting). The potential field (voltage) is plotted in the brief moment prior to failure to show that this agglomerate would result in a short circuit and an inability to sustain the electric field. ....     | 46 |
| Figure 3.1  | Mark II electrospinning apparatus.....                                                                                                                                                                                                                                                                                                                                             | 51 |
| Figure 3.2  | Example of diameter distribution used to visualize fiber diameter in electrospun fiber mats .....                                                                                                                                                                                                                                                                                  | 54 |
| Figure 3.3  | Simulation results of electric field within the Faraday tube. The results go from a voltage bias on the injection needle (on the left) to neutral (middle) and voltage bias on the collector (right). The results show that the ground plane is shifted back and forth towards the side with the lower voltage. The field shape suggests focusing mechanisms may be possible. .... | 56 |
| Figure 3.4  | The difference index of the films with (first three) and without (last three) the Faraday tube .The results show a good improvement with implementation of the tube.....                                                                                                                                                                                                           | 56 |



|             |                                                                                                                                                                                                                                                                                                                    |    |
|-------------|--------------------------------------------------------------------------------------------------------------------------------------------------------------------------------------------------------------------------------------------------------------------------------------------------------------------|----|
| Figure 3.5  | Photographs showing macro film morphological changes due to Faraday focusing: (a) Single phase film (b) dual phase, unfocused, (c) single phase, focused.....                                                                                                                                                      | 58 |
| Figure 3.6  | Two main classes of micro-scale morphology: (a) with beads and (b) without beads.....                                                                                                                                                                                                                              | 59 |
| Figure 3.7  | Histograms of fiber diameter. (a) Diameter distribution of sample A and (b) diameter distribution of sample B. ....                                                                                                                                                                                                | 60 |
| Figure 3.8  | Fluorescent confocal microscopy of multi-phase twin injection co-electrospun fibers (a) fluorescent phase only (b) both phases, no fluorescence, (c) both phases with markers (NOTE: Figures b and c appear identical in black and white. See electronic copy for color).....                                      | 61 |
| Figure 3.9  | Schematic description of environmental process controls in Mark III system. ....                                                                                                                                                                                                                                   | 62 |
| Figure 3.10 | DSC thermograms for all specimens. ....                                                                                                                                                                                                                                                                            | 70 |
| Figure 3.11 | SEM micrographs showing (a) spherical structures representing $\beta$ spherulites in the film solution cast from DMF and (b) radial lamellae formation in $\alpha$ -phase film. ....                                                                                                                               | 71 |
| Figure 3.12 | (a) Full range scattering pattern of 20% PVDF cast from pure DMF demonstrating pure $\beta$ crystal structure. (b) Scattering pattern of PVDF injection molded PVDF showing pure $\alpha$ crystal structure. (c) Scattering pattern of PVDF extruded from melt demonstrating pure $\alpha$ crystal structure. .... | 72 |
| Figure 3.13 | (a) Scattering patterns of PVDF electrospun from 10%, 15% and 20%. ....                                                                                                                                                                                                                                            | 74 |
| Figure 3.14 | (a) Scattering patterns for fibers electrospun from 15wt% PVDF in DMF with 0.1% carbon nanotubes included in the PVDF and (b) electrospun from 20wt% PVDF in DMF with 0.25% carbon nanotubes showing that a larger concentration of nanotubes has a drastic effect on $\beta$ -phase content. ....                 | 75 |
| Figure 3.15 | (a) Scattering patterns of PVDF solution cast from 2:1 NMP:DMF mix (solcast-mix) and (b) PVDF electrospun from the same solution....                                                                                                                                                                               | 76 |
| Figure 3.16 | FTIR results confirming $\beta$ phase PVDF with absorption peaks at $840\text{cm}^{-1}$ and $1279\text{cm}^{-1}$ .....                                                                                                                                                                                             | 77 |

|            |                                                                                                                                                                                                                                                                                                                                                                                                                                                    |    |
|------------|----------------------------------------------------------------------------------------------------------------------------------------------------------------------------------------------------------------------------------------------------------------------------------------------------------------------------------------------------------------------------------------------------------------------------------------------------|----|
| Figure 4.1 | Illustration of the three possible ways of failing the poling process: (a) corona discharge occurs when the current passes through ionized air around the sample (b) electrical surface tracking is when the current conducts through the interphase between the sample and the air, and (c) dielectric breakdown is when the polymer itself fails under load and becomes conductive.....                                                          | 80 |
| Figure 4.2 | For testing of dielectric breakdown strength the electrodes of the custom electrical testing system support the sample horizontally. For corona discharge the sample is removed and the electrodes are tested at differing distances of separation.....                                                                                                                                                                                            | 84 |
| Figure 4.3 | For testing of electrical surface tracking initiation voltage the electrodes of the custom electrical testing system support rest on the sample, which is attached to a GPO3 platform. The voltage at which tracking initiates is tested for differing electrode separation distances.....                                                                                                                                                         | 85 |
| Figure 4.4 | Demonstration of the transition point between electrical surface tracking and corona discharge when the sample is cut intentionally short and placed in the sample holder for poling. ....                                                                                                                                                                                                                                                         | 87 |
| Figure 4.5 | Corona discharge behaves in a logarithmic fashion as described by Peak's Law. Experimental testing confirms this and takes into account geometric variables such as electrode type. ....                                                                                                                                                                                                                                                           | 87 |
| Figure 4.6 | Electrical tracking initiation voltage for various distances for all samples. All samples demonstrate having the same minimum initiation voltage relationship with distance with the exception of the solution cast and electrospun samples containing carbon nanotubes. This increase is due to proximity of the carbon nanotubes to the surface of the materials, which is higher for the solution cast and lower for the electrospun films..... | 89 |
| Figure 4.7 | Root mean square error between the minimum surface tracking initiation voltage of neat PVDF and all samples – higher values denote higher statistical likelihood of surpassing the surface tracking initiation voltage of the material. ....                                                                                                                                                                                                       | 90 |
| Figure 4.8 | SEM micrograph of the surface of commercial PVDF showing a homogenous surface with some roughness from manufacture .....                                                                                                                                                                                                                                                                                                                           | 91 |
| Figure 4.9 | SEM of the surface of solution cast PVDF showing a very smooth surface with few defects. ....                                                                                                                                                                                                                                                                                                                                                      | 92 |

|             |                                                                                                                                                                                                                                                                                                                                                                                                                                                   |     |
|-------------|---------------------------------------------------------------------------------------------------------------------------------------------------------------------------------------------------------------------------------------------------------------------------------------------------------------------------------------------------------------------------------------------------------------------------------------------------|-----|
| Figure 4.10 | Optical micrograph showing the surface of solution cast PVDF with agglomerated carbon nanotubes. ....                                                                                                                                                                                                                                                                                                                                             | 93  |
| Figure 4.11 | SEM micrograph of electrospun PVDF. The fibrous morphology is unchanged by the addition of carbon nanotubes, .....                                                                                                                                                                                                                                                                                                                                | 93  |
| Figure 4.12 | SEM micrograph of the electrospun/solution cast PVDF composite.....                                                                                                                                                                                                                                                                                                                                                                               | 94  |
| Figure 4.13 | Electrospun/solution cast PVDF with carbon nanotubes integrated in the electrospun phase. The composite with carbon nanotubes has slightly better wetting and a more homogenous surface. ....                                                                                                                                                                                                                                                     | 95  |
| Figure 4.14 | Illustration of the electrode/sample configuration.....                                                                                                                                                                                                                                                                                                                                                                                           | 96  |
| Figure 4.15 | The results of corona discharge and electrical surface tracking initiation voltage. The minimum sample overlap length to prevent both effects can be determined by ensuring the distance is large enough that the voltage does not exceed either curve. ....                                                                                                                                                                                      | 96  |
| Figure 4.16 | Measured dielectric breakdown of PVDF films compared to reported poling voltage. Both composite samples are above the threshold of dielectric breakdown strength and are able to be poled, whereas carbon nanotube infused solution cast samples and electrospun samples are below the threshold and cannot sustain a high enough electric field to pole. As expected both the commercial and solution cast exceed the poling threshold.....      | 97  |
| Figure 4.17 | Freeze fracture SEM micrograph of the composite PVDF film with carbon nanotubes demonstrating the near-fully dense internal structure which allows the composite to sustain higher electric fields while maintaining the advantage of integrated carbon nanotubes. ....                                                                                                                                                                           | 99  |
| Figure 5.1  | The composite processing layup for production of PVDF polymer-polymer thin films includes aluminum tooling and caul plate to produce tooling-quality finish on the film, distribution media connected to a vacuum line to vacate the air and solvents, and a vacuum bag to ensure a proper seal. They layup is left under vacuum for 48 hours and subsequently left in ambient pressure for 24 hours to ensure complete solvent evaporation. .... | 104 |
| Figure 5.2  | Solution cast PVDF is shown to have an (a) micro-porous structure formed of (b) $\beta$ -phase spherulites.....                                                                                                                                                                                                                                                                                                                                   | 107 |

|             |                                                                                                                                                                                                                                                                                                                                                              |     |
|-------------|--------------------------------------------------------------------------------------------------------------------------------------------------------------------------------------------------------------------------------------------------------------------------------------------------------------------------------------------------------------|-----|
| Figure 5.3  | Electrospun morphology is nearly identical with or without carbon nanotubes with fibers approximately 200 nm, though some larger fibers and beads also exist. ....                                                                                                                                                                                           | 108 |
| Figure 5.4  | Surface of PVDF polymer-polymer composite showing (a) a textured surface and voids from trapped air and solvent and (b) evidence of fully dense electrospun composite structure just under the surface .....                                                                                                                                                 | 109 |
| Figure 5.5  | Freeze fracture of neat PVDF polymer-polymer composite processed at room temperature (a) having a layered brittle structure and very heterogeneous internal microstructure and processed at 60°C (b) demonstrating a higher degree of polymer chain diffusion between the matrix and fiber phase allowing for a more homogenous internal microstructure..... | 111 |
| Figure 5.6  | PVDF composite with electrospun phase containing 0.1wt% carbon nanotubes (a) and 0.25% carbon nanotubes (b). Both samples show a brittle fracture with layer by layer delamination along electrospun planes. The composites have very good consolidation and few small scale voids. ....                                                                     | 112 |
| Figure 5.7  | Thermal analysis of composite and solution cast PVDF films – DSC curves showing the onset of melting and peak endotherm positions are similar regardless of processing parameters.....                                                                                                                                                                       | 113 |
| Figure 5.8  | Integral of the melt endotherm showing that the heated composite process results in slightly higher crystallinity. ....                                                                                                                                                                                                                                      | 114 |
| Figure 5.9  | WAXS patterns for each type of composite film showing that regardless of process conditions the micro infusion system consistently produces films with high $\beta$ -phase content. (a) Neat Composite (b) Heated Composite (c) Composite with 0.1% carbon nanotube (d) Composite with 0.25% carbon nanotube .....                                           | 115 |
| Figure 5.10 | FTIR data confirming the existence of $\beta$ phase PVDF.....                                                                                                                                                                                                                                                                                                | 116 |
| Figure 5.11 | DSC results appended with the composite data. Note that the DSC curve of the composite is almost identical to that of the solution cast film. ....                                                                                                                                                                                                           | 117 |
| Figure 5.12 | Stress-strain curve for composite samples .....                                                                                                                                                                                                                                                                                                              | 118 |

|             |                                                                                                                                                                                                                             |     |
|-------------|-----------------------------------------------------------------------------------------------------------------------------------------------------------------------------------------------------------------------------|-----|
| Figure 5.13 | SEM micrograph showing a composite polymer-polymer film containing 0.25wt% carbon nanotube reinforcement in the fiber phase. The micrograph shows fibers spanning the cracks formed in the matrix prior to failure. ....    | 119 |
| Figure 5.14 | Calculated elastic modulus for each film. ....                                                                                                                                                                              | 121 |
| Figure A.1  | Mark I, very rudimentary electrospinning apparatus ....                                                                                                                                                                     | 135 |
| Figure A.2  | Carriages for electrospinning injection needles ....                                                                                                                                                                        | 136 |
| Figure A.3  | Mark II electrospinning apparatus with Faraday cage ....                                                                                                                                                                    | 137 |
| Figure A.4  | Polycarbonate environmental chamber enclosing Mark III electrospinning system ....                                                                                                                                          | 138 |
| Figure A.5  | Desiccation, heating, and air flow regulation in support of the Mark III electrospinning system ....                                                                                                                        | 138 |
| Figure A.6  | The Mark III electrospinning system is equipped with articulated arms for injection needles held to the chamber by gantry sliders. The collection plate is also suspended by the gantry system and is fully adjustable..... | 139 |
| Figure A.7  | External thermal management of the collector plate using infrared heat.....                                                                                                                                                 | 141 |
| Figure A.8  | High Voltage system, engineered to precisely control the distance between both electrodes for accurate measurement and control of electric field strength .....                                                             | 142 |
| Figure A.9  | High Voltage system suspended in oil for thermal management and prevention of short circuits.....                                                                                                                           | 143 |
| Figure A.10 | Gen 2 high voltage system positioned horizontally for dielectric breakdown, corona discharge or poling .....                                                                                                                | 144 |
| Figure A.11 | Gen 2 high voltage system positioned for electrical surface tracking test .....                                                                                                                                             | 145 |
| Figure B.1  | Example SEM micrograph used as input for the computer vision code.....                                                                                                                                                      | 147 |
| Figure B.2  | Histogram generated from image .....                                                                                                                                                                                        | 148 |

|             |                                                                                                                             |     |
|-------------|-----------------------------------------------------------------------------------------------------------------------------|-----|
| Figure B.3  | Smoothed histogram derivative used for finding the correct threshold .....                                                  | 149 |
| Figure B.4  | Adaptive thresholding to convert to shape image .....                                                                       | 150 |
| Figure B.5  | Perimeter detection used to find edges in shape image.....                                                                  | 151 |
| Figure B.6  | Unit edge cell vs. unit shape cell .....                                                                                    | 151 |
| Figure B.7  | Illustration of line parameterization .....                                                                                 | 152 |
| Figure B.8  | Unit edge cell transformed into Hough Space and rendered .....                                                              | 154 |
| Figure B.9  | Depiction of unit edge cell line detection.....                                                                             | 155 |
| Figure B.10 | Depiction of analyses for determining fiber candidates and graphical representation of new variables $\alpha$ and $D$ ..... | 156 |
| Figure B.11 | Parameterized line (red) overlaid on unit edge cell.....                                                                    | 158 |
| Figure B.12 | Visualization of boolean test for connectedness. (a) shows a passing case while (b) shows a failing case. ....              | 159 |
| Figure B.13 | Correct identification of lines overlaid over the unit shape cell.....                                                      | 161 |
| Figure B.14 | Fiber diameter histogram as outputted by the computer vision code....                                                       | 161 |

## **ABSTRACT**

The study of piezoelectric materials has traditionally focused largely on homogeneous crystalline or semi-crystalline materials. This research focuses on the concept of piezoelectric composites using selective microstructural reinforcement in the piezoelectric material to improve the piezoelectric properties. This is done using a polyvinylidene fluoride (PVDF) and carbon nanotube composite as the model system. A multi-tiered engineering approach is taken to understand the material (experimental and computational analyses) and design a composite system which provides an effective platform for future research in piezoelectric improvement.

A finite element analysis is used to evaluate the ability of carbon nanotubes to generate a heterogeneous electric field where local improvements in electric field produce an increase in the effective piezoelectric strength. The study finds that weight percent and aspect ratio of the carbon nanotubes are of key importance while formations of percolating networks are detrimental to performance.

This motivates investigation into electrospinning into a method of producing sub percolation threshold composites with large carbon nanotube content. However, the electrospun fabrics have too low of a dielectric strength to sustain high strength electric fields. This is studied within the context of high voltage physics and a solution inspired by traditional composites manufacturing is proposed wherein the electrospun fiber mat is used as the fiber reinforcing component of a polymer-polymer composite.

This composite is thoroughly analyzed to show that it allows for a high dielectric strength combined with high carbon nanotube content. It is also shown that

the PVDF contains the proper crystal structure to allow for piezoelectric properties. Furthermore, the addition of carbon nanotubes greatly improves the strength and stiffness of the composite, as well as affecting the internal electric field response to an applied voltage. These qualities make the composite material an ideal platform for future work in polymer ferroelectric research.



## **Chapter 1**

### **INTRODUCTION AND MOTIVATION**

Over the past several years there has been broad interest in developing smart materials, where materials have the capability to sense and respond to external stimuli. A number of materials show piezoelectric behavior when electrical charge accumulates when the material is deformed. Piezoelectric materials can be utilized as sensors, where applied strain results in a measurable voltage, as well as actuators, where an applied electric field results in mechanical strain. Nanomaterials offer unique potential in tailoring both the mechanical and electrical properties of materials. Previous experimental results [1,2] show that the properties of piezoelectric polymers can be enhanced with the addition of carbon nanotubes.

This research focuses on understanding the fundamental role of the carbon nanotube reinforcement on the overall piezoelectric effect in these nanocomposites and developing appropriate processing techniques capable of producing the desired material structure to enhance the piezoelectric coupling effect. In this chapter the fundamentals of piezoelectricity and piezoelectric polymers are discussed and the opportunities of tailoring material properties using carbon nanotubes are reviewed. The technique of electrospinning, which is adopted in this research as a means to disperse nanotubes and prevent them from re-agglomerating while producing the desired crystal structure is also presented.

The theoretical foundation of piezoelectricity involves the constitutive relationship between the electrical and mechanical properties of the material and is

utilized in the computational modeling approach presented in Chapter 2. The properties of piezoelectric polymers and carbon nanotube-based composites are each introduced in order to understand how the carbon nanotubes may improve the coupling behavior of piezoelectric polymers. Chapters 3-5 detail processing and characterization of novel carbon nanotube-reinforced polymer-polymer composites with an aim at producing nanocomposites with a high degree of dispersion below the electrical percolation threshold in the preferred crystal structure.

## **1.1 The Piezoelectric Effect**

The piezoelectric effect (coupling of mechanical and electrical properties) was discovered in March of 1880 when Pierre and Jacques Curie [3] delved into a thorough investigation into the theoretical possibility of effect alluded to by studying the pyroelectric effect (coupling of thermal and electrical properties) [4]. Shortly after, mathematician Gabriel Lippmann demonstrated that an inverse piezoelectric effect should exist [5], which the Curie brothers quickly proceeded to demonstrate [6]. During World War II, in the hunt for materials to build a better capacitor, Barium Titanate – the first discovered piezoelectric ceramic – was confirmed to have an exceptionally high dielectric constant which under further investigation was shown to be due to its ferroelectric properties [7].

With this discovery also came introduction of the technique of “poling” – using a strong electric field to align the dipoles in a crystalline material so that the bulk material exhibited a piezoelectric effect. This broadened the scope of the search for piezoelectric materials to include many more crystalline materials. The first polymer to exhibit the piezoelectric effect was in cellulose in 1963 [8]. In 1969 it was

discovered by Kawai [9] that through appropriate processing steps, poly(vinylidene fluoride) (PVDF) could be made to have piezoelectric properties. Since then PVDF, along with its copolymers, has been among the prime candidates for modern piezoelectric polymers. The piezoelectric effect, in essence, represents a material's ability to couple mechanical response or stimuli (strain) to electrical response or stimuli. There are four main mathematical representations of this effect [10]: strain-charge form, stress-charge form, strain-voltage form, and stress-voltage form.

Perhaps the most illustrative of these is the strain-charge form. Coupling terms are added to the constitutive equations for electric displacement and strain field, respectively.

$$S = s_{dE=0} T + d^t E \quad (1.1)$$

and

$$D = dT + \epsilon_{dT=0} E \quad (1.2)$$

where  $d$  can be represented in matrix form as:

$$d = \begin{bmatrix} 0 & 0 & 0 & 0 & d_{15} & 0 \\ 0 & 0 & 0 & d_{24} & 0 & 0 \\ d_{31} & d_{32} & d_{33} & 0 & 0 & 0 \end{bmatrix} \quad (1.3)$$

$S$  is the strain tensor,  $s$  represents the stiffness matrix,  $T$  represents the stress tensor,  $d$  and  $d^t$  represent the direct and indirect piezoelectric coupling matrices,  $\epsilon$  represents the electrical permittivity matrix and  $E$  is the electric field vector. The strain is mapped to the electric field via the piezoelectric coupling matrix. The equations and boundary conditions are as illustrated in Figure 1.

For a homogenous piezoelectric film the electric field is quite simple and results in an extension in two directions and a contraction in the third (or the inverse).

If there are no mechanical boundary conditions the electric field is completely linear.

If a mechanical boundary condition is present, a system of equations (Equation 1.3) must be solved in order to determine both the displacement and field shape.

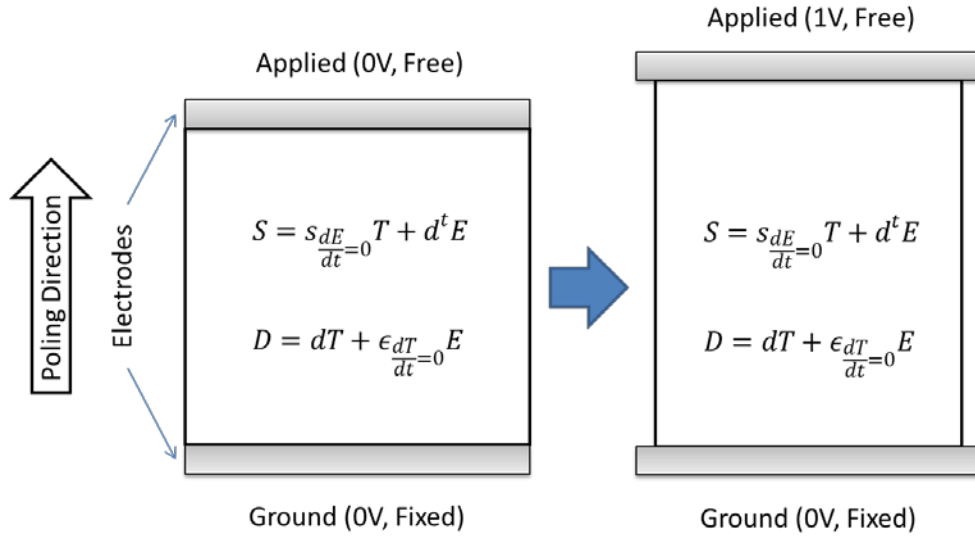


Figure 1.1 Schematic representation of the basic piezoelectric physics.

$$\begin{bmatrix} S_1 \\ S_2 \\ S_3 \\ S_4 \\ S_5 \\ S_6 \\ D_1 \\ D_2 \\ D_3 \end{bmatrix} = \begin{bmatrix} s_{11} & s_{12} & s_{13} & 0 & 0 & 0 & 0 & 0 & d_{31}^t \\ s_{21} & s_{22} & s_{23} & 0 & 0 & 0 & 0 & 0 & d_{32}^t \\ s_{31} & s_{32} & s_{33} & 0 & 0 & 0 & 0 & 0 & d_{33}^t \\ 0 & 0 & 0 & s_{44} & 0 & 0 & 0 & d_{24}^t & 0 \\ 0 & 0 & 0 & 0 & s_{55} & 0 & d_{15}^t & 0 & 0 \\ 0 & 0 & 0 & 0 & 0 & s_{66} & 0 & 0 & 0 \\ 0 & 0 & 0 & 0 & d_{15} & 0 & \epsilon_{11} & 0 & 0 \\ 0 & 0 & 0 & d_{24} & 0 & 0 & 0 & \epsilon_{22} & 0 \\ d_{31} & d_{32} & d_{33} & 0 & 0 & 0 & 0 & 0 & \epsilon_{33} \end{bmatrix} \begin{bmatrix} T_1 \\ T_2 \\ T_3 \\ T_4 \\ T_5 \\ T_6 \\ E_1 \\ E_2 \\ E_3 \end{bmatrix} \quad (1.3)$$

In composite materials the electrical properties of the reinforcement alter the local permittivity, stiffness and piezoelectric coefficient, making the above matrix a function of space. The problem ceases to be Laplacian and can be represented by Equation 1.4.

$$\nabla \cdot (\epsilon(x, y)) \nabla V = 0 \quad (1.4)$$

This means that the coupling relationship can not only be affected by the intrinsic material properties (represented by  $d^t$ ,  $d$ ,  $\epsilon$  and  $s$ ) but also by the potential field  $V$  throughout the material. This forms the basis for improvements in the piezoelectric strength through the addition of nanoscale reinforcements.

## 1.2 Polyvinylidene Fluoride

Poly(vinylidene fluoride) (PVDF) is a thermoplastic fluoropolymer with common applications as a structural material and as electrical insulation. PVDF has good mechanical and dielectric properties; it is thermally and chemically stable and is relatively inexpensive. Since its discovery by Kawai it has been used in a variety of cutting edge applications such as batteries [11], capacitors [12], biomedical applications [13] and, exploiting its piezoelectric properties, sensors and actuators [14]. The piezoelectric properties of PVDF are dependent on two main factors – first the polymer must exhibit the proper crystal structure [15] and secondly that structure must be polarized under a high strength electric field [16].

During polymerization, the monomers link to each other along the carbon backbone with several differing types of rotational conformations; for PVDF these are combinations of trans (T), gauche (G) and gauche' (G'). There are four known crystal structures of PVDF: Phase I (colloquially known as the  $\beta$ -phase) is highly polar (and

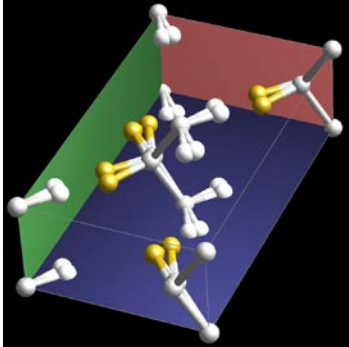
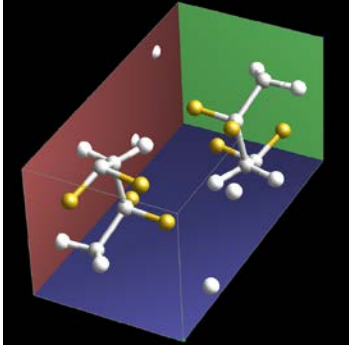
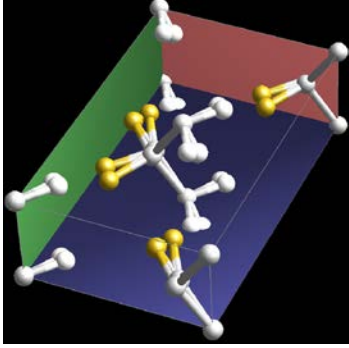
thus piezoelectric). It takes an all trans conformation TTTT with a Cm2m space group in an orthorhombic structure. Phase II (colloquially known as the  $\alpha$ -phase) is non polar and takes a trans-gauche TGTG conformation with a P21 space group on a monoclinic crystal lattice. Phase III (colloquially known as  $\gamma$ -phase) is moderately polar and takes a TTTGTTTG' configuration with a C2cm space group in an orthorhombic structure [17]. Phase IV (colloquially known as  $\delta$ -phase) is the polar version of the  $\alpha$ -phase and has the same conformation but also has piezoelectric properties [18]. Table 1.1 shows a summary of the attributes of the different polymorphs of PVDF as well as a graphical representation of their unit cell configuration.

The crystal structure of PVDF has been subject to a great deal of study. As early as 1972, Hasegawa and Takahashi [17] thoroughly investigated the first three crystal polymorphs. Since then, a multitude of studies relating process conditions to crystal form have been produced. In general, PVDF is formed either from melt or through solution casting. Produced from melt at room temperature, the PVDF results in an  $\alpha$ -phase polymorph. It has also been shown that if  $\alpha$ -phase PVDF is drawn at a ratio above 5, the crystals are transformed into the  $\beta$ -phase [19]. Conversion is also possible through application of high electric field [20], and the combination of the two (high temperature during corona poling) resulted in even higher piezoelectric constant [21].  $\beta$ -phase generation was also seen during processing from melt at very high pressures [22].

When casting from solution, the polymorph present has shown a strong dependence on solvent evaporation rate [23] with low rates of evaporation favoring the  $\beta$ -phase and higher rates favoring the  $\alpha$ -phase. Some researchers have shown  $\gamma$ -production from solvent casting using dimethyl sulfoxide as the solvent [24].

However, Gregario [23] disproves claims that  $\gamma$ -phase PVDF is produced and acknowledges that phase differentiation between the  $\beta$  and  $\gamma$  polymorphs is quite difficult without having broad enough spectrum data. When an appropriate solvent is used,  $\beta$ -phase PVDF is reliably produced from solution casting at less than 70°C.

Table 1.1:  $\alpha$ ,  $\beta$ , and  $\gamma$  polymorphs of PVDF and their attributes.

|                                                                                     |                 |                     |
|-------------------------------------------------------------------------------------|-----------------|---------------------|
|    | Name            | Phase-I: $\beta$    |
|                                                                                     | Configuration   | TTTT                |
|                                                                                     | Space Group     | Cm2m                |
|                                                                                     | Crystal Lattice | Orthorhombic        |
|   | Name            | Phase-II: $\alpha$  |
|                                                                                     | Configuration   | TGTG                |
|                                                                                     | Space Group     | P2 <sub>1</sub> /c  |
|                                                                                     | Crystal Lattice | Monoclinic          |
|  | Name            | Phase-III: $\gamma$ |
|                                                                                     | Configuration   | TTTGTTTG'           |
|                                                                                     | Space Group     | C2cm                |
|                                                                                     | Crystal Lattice | Orthorhombic        |

Production of both  $\alpha$ -phase and  $\beta$ -phase was shown to occur through different annealing conditions of the  $\gamma$ -phase polymorph – producing primarily  $\beta$ -phase at lower temperatures and  $\alpha$ -phase at higher temperatures. Dissolution temperature was also shown to have an effect on polymorph type and content [25], with lower dissolution temperatures favoring the  $\beta$ -polymorph. The primary method of producing  $\gamma$ -phase polymorph is through high temperature (near the melting point) crystallization for extended periods of time. Adding nanomaterials to PVDF has also shown promise for improving the piezoelectric properties [2,26–28]. For example, adding nanoclays to PVDF induced formation of the  $\beta$ -phase polymorph regardless of loading or processing conditions, although higher concentrations of nanoclays reduced the overall crystallinity [29].

### **1.3 Carbon Nanotube Composites**

Carbon nanotubes have become an increasingly important material [30]. Among their many impressive attributes, carbon nanotubes have very high thermal and electrical conductivities, high stiffness and strength and large aspect ratios (length/diameter). When processed correctly, these properties can be used to alter the anisotropic mechanical and physical properties of composite material systems [31]. Carbon nanotubes have also shown to have sensing and actuation properties [32], however scalability and durability of nanotube-based sensors and actuators are still critical issue that must be addressed before practical implementation.

It has been demonstrated that carbon nanotubes can be used to form electrically conducting networks that can be embedded in fiber composites in order to change the bulk electrical properties, and these composites show a strong dependence



of the electrical properties on the composite micro-structure [33]. More significantly, it was shown that the electrical properties of the composite part can be drastically changed through the addition of a very low concentration of carbon nanotubes – as low as 0.025% [34]. At the percolation threshold, where conducting networks are formed in the polymer matrix, the electrical conductivity changes several orders of magnitude. Li and co-workers [35] have shown through Monte Carlo simulations that both nanotube waviness and aspect ratio significantly affect the percolation thresholds of these nanocomposites – both increases in aspect ratio and waviness reduce the concentration of carbon nanotubes required to achieve percolation.

Percolating networks of carbon nanotubes have been demonstrated for sensing of both strain and damage in advanced composites [31,36]. The composites show piezoresistivity, where the electrical resistance of the specimen changes significantly with applied strain. When cracks form in the polymer matrix, conducting pathways are severed. It has been shown that grading the structure at both the micro- and nano-levels can improve sensing response.[37]

Laxminarayana *et al.* [2] have produced electrospun composite fabrics composed of PVDF copolymers with carbon nanotube inclusions which achieved significantly higher degrees of sensing (voltage output) than neat PVDF. The films were produced over a range of differing carbon nanotube concentrations and showed a significant improvement in response as much as 35-fold. The effect was attributed to the alignment of dipoles as well as increased Young's modulus due to the carbon nanotube reinforcement. Owens and co-workers [38] have investigated the inclusion of single walled carbon nanotubes in a PVDF nanocomposite and have found that it had a significant impact on the processing and properties of the polymer. The

nanocomposite was studied by Raman and NMR spectroscopy. The results strongly suggest bonding interactions between the polymer and the nanotubes, most likely through the fluorine groups. The inclusion of the single walled carbon nanotubes also increased the conductive and ferromagnetic properties while also resulting in an improvement in hardness.

A number of researchers have examined the processing of carbon nanotube-reinforced PVDF composites formed through solution casting [39, 40]. Their work looked at techniques for dispersing carbon nanotubes in solution and characterizing the resulting material properties. It was determined that the carbon nanotubes acted as nucleation points for the crystal growth but the overall crystallinity decreased. The actuation strain was increased while the required DC voltage for actuation was decreased. It was determined that the nanocomposite had a relatively low percolation threshold of 0.23 vol %. This represents a unique challenge because tailoring the process to form  $\beta$ -phase crystallites (longer processing time) also causes high degrees of agglomeration in the carbon nanotubes; this agglomeration allows for the existence of spanning clusters which cause a short circuit in the PVDF film. Percolation makes PVDF unable to sustain an electric field and the piezoelectric utility of the film is lost.

The benefits of adding carbon nanotubes on the piezoelectric properties are only realized when below the percolation threshold. Even if the carbon nanotubes are well dispersed they are able to form conductive pathways due to their large aspect ratios. As a result, it is important to establish techniques for manufacture that allow for increasing the carbon nanotube content without forming percolating networks.

## 1.4 Electrospinning

As highlighted in previous sections the piezoelectric properties of PVDF are influenced by both the crystal structure and the morphology of the nanoscale reinforcement. It is beneficial to add well dispersed carbon nanotubes so long as the percolation threshold is not exceeded. Solution casting of PVDF can be a slow process, and carbon nanotubes tend to re-agglomerate in solution. This re-agglomeration forms spanning clusters in the polymer, reducing the percolation threshold. Electrospinning is used in this research as a method of achieving high quality dispersions of carbon nanotubes where the resulting composites are below the percolation threshold. The electrospun fibers are formed very rapidly, preventing nanotubes from re-agglomerating in solution.

Electrospinning is a widely utilized technique that can produce micro and nano-scale polymer fibers. The process was popularized by Taylor in 1964 but was not fully understood until 1993 when high speed imaging technology was first able to observe the process [41, 42]. Since then a large body of research has examined the effects of electrospinning process variables on the structure and properties of the films they produce [43]. Fluid viscosity, electric field strength and length, temperature, and evaporation rate all play key roles in the micro-scale morphology and nano-scale surface texture of the fibers. Depending on the evaporation rate (solvent content, relative humidity, temperature) the fibers transition from spray, to fibers with beads, to uniform fibers [44].

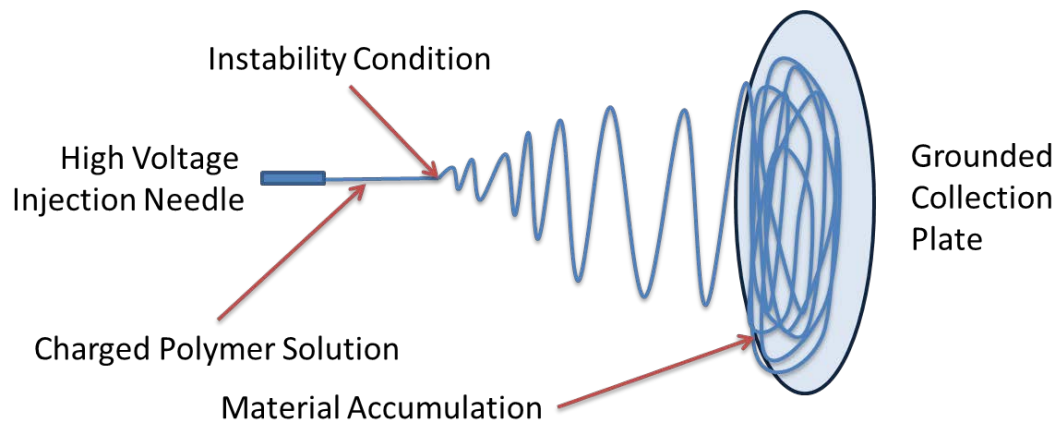


Figure 1.2 Schematic representation of the electrospinning process

Electrospinning is a process where fibers are spun in the presence of a high-power electric field [45]. The polymer is dissolved in solution and fed through a positively charged injector needle; a negatively charged (or grounded) collector plate is placed at some distance from the needle (see Figure 1.2). The electric field causes charge accumulation in the polymer which draws it towards the collector in a steady stream straight line flow [46], counterbalanced by the fluid viscosity. At some point this stream reaches an instability condition and begins to spin, during which the stream elongates and experiences proportional reduction in diameter [46, 47]. When electrospinning from solution the solvent evaporates, leaving a randomly oriented non-woven fabric composed of micro- or nano-scale polymer fibers.

Electrospun PVDF has found various uses; such as polymer electrolytes [49], nano-scale actuators and sensors [50], and filtration media [51]. The technique still poses a problem to the production of macroscopic piezoelectric films because of the surface morphology and porosity of the fabric. The surface morphology makes electrode placement very difficult and the porosity results in a drastic reduction in

dielectric breakdown strength, due to the air gaps creating pathways for the electric current [52].

Carbon nanotubes can be added to the solution before electrospinning [53] in order to create nanocomposite fibers. The electrospun fibers effectively act as a scaffold holding the nanotubes in place while keeping them separate. In order to integrate nanotubes into nanocomposites for the benefit of enhanced sensing and actuation, it is necessary to develop techniques to avoid the re-agglomeration of nanotubes which results in the formation of electrical spanning clusters and can drastically decrease the dielectric breakdown strength.

### **1.5 Carbon Nanotube-Reinforced Polymer-Polymer Composite Concept**

In order to solve the poor dielectric strength the carbon nanotube reinforced electrospun fabric the concept of this research is to utilize electrospinning to first create nanocomposite fibers where nanotubes are uniformly dispersed and then consolidate the fibers to form a novel self-reinforced micro-composite. Capiati and Porter [54] introduced the concept of self-reinforced composites by using two different blends of polyethylene – one with a higher melting point. This extends the concept of fiber-reinforced polymer to polymer fibers reinforced with a matrix of the same polymer. Since then, self-reinforcing polymer composites have been widely studied using a variety of processing methodologies. Self-reinforced composites have been manufactured by extrusion, rolling, hot compaction, and re-dissolution along with as many other techniques [55–57]. Thermoplastic polymer-polymer composites are almost exclusively manufactured by heat treatment. For piezoelectric PVDF composites the heat treatment would convert the crystal structure to the  $\alpha$  form and erase the piezoelectric properties.

## 1.6 Motivation

This work focuses on the addition of carbon nanotubes to PVDF in order to improve its properties while avoiding drawbacks typically attributed to poor dispersion of the reinforcement (carbon nanotubes) in the matrix (PVDF). The motivation of this work is to use carbon nanotube reinforced PVDF as a platform for future research in polymer ferroelectrics by meeting all of the basic requirements of the production of a piezoelectric composite in the form of a thin film. For PVDF based composites improvements can be in the chemical structure (co-polymers), crystal structure (crystallinity and crystal polymorphs), physical structure (microstructural changes) and electrical morphology (addition of conductive nanoparticles). All these mechanisms are studied herein with the exception of co-polymers.

First the mechanisms of electrical morphology and physical structure are investigated computationally in Chapter 2, showing that carbon nanotubes can have a positive impact due to their high electrical conductivity. It is demonstrated that the primary mechanism of improving the piezoelectric properties of PVDF are in the carbon nanotubes modulation of the internal electric field; proving that a large concentration of non-percolating carbon nanotubes is optimal.

In Chapter 3 the crystal structure and physical structure are investigated. Electrospinning is studied as a manufacturing method for formation of the non-percolating carbon nanotube networks motivated by Chapter 2. Carbon nanotube reinforced electrospun PVDF is shown to meet the polymorphic requirements of manufacturing of a piezoelectric material. The preferred  $\beta$  phase is formed rapidly during electrospinning and the addition of carbon nanotubes further enhances  $\beta$  phase formation.

Chapter 4 demonstrates that the high porosity of the electrospun film inhibits the materials ability to sustain a high strength electric field, reducing its practicality, therefore a novel engineering solution is proposed which uses the carbon nanotube reinforced electrospun PVDF as a the fiber reinforcement phase of a polymer-polymer composite with a PVDF matrix. The as-produced nanocomposites show very good dielectric breakdown.

Chapter 5 fully investigates the carbon nanotube reinforced polymer-polymer composite by characterizing the crystalline structure and nanocomposite morphology. The infusion process used to form the composite also results in the production of the proper piezoelectric polymorph of PVDF and the nanocomposite retains its fibrous morphology.

## **Chapter 2**

### **MODELING OF CARBON NANOTUBE REINFORCED PIEZOELECTRIC COMPOSITES USING FINITE ELEMENT ANALYSIS**

As discussed in Chapter 1, several mechanisms have been proposed for the improvement in piezoelectric response, including changes in the crystal structure and morphology, mechanical reinforcement, and alteration of internal electrical fields. In order to understand how the carbon nanotubes and their morphology in a nanocomposite (dispersion, orientation, aspect ratio, waviness, etc.) affect the piezoelectric coupling a series of simulations were conducted to understand the parameters that most significantly influence the response.

First, 2-dimensional finite element analysis (FE) simulations are presented using COMSOL Mutliphysics to examine the influence of alignment, aspect ratio and nanotube concentration on the piezoelectric response. One limitation of the 2-dimensional simulations is that there is no differentiation between carbon nanotubes and carbon platelets, and the carbon nanotube geometry was forced to be very simplistic, modeled by rectangles. The dispersion of the carbon nanotubes was also artificial, in that the nanotubes were added to specific locations and any overlap of nanotubes resulted in local conduction.

To overcome the limitations of both the 2-dimensional simulations and pre- and post-processing capability of the COMSOL software a more advanced FE simulation approach was developed. This simulation is improved by expanding to 3 dimensions and adding a substantial amount of flexibility in the creation of the



geometries. Here control over the 3-dimensional orientation and individual nanotube waviness was added in order to directly measure the contribution of the geometric effects (aspect ratio, weight percent loading, in-plane orientation, and waviness) to the enhancement in piezoelectric strength. MATLAB is utilized to generate carbon nanotube geometries and then CATIA is used to generate the scaffold and build the model. ANSYS is then used to solve the governing equations and electrical potential.

## **2.1 2-Dimensional Nanocomposite Model based on COMSOL Mutliphysics**

The 2-dimensional simulation utilizes the COMSOL solver to calculate the piezoelectric response based on the theory described in Chapter 1 using the strain-charge form to solve the constitutive equations. Figure 2.1 demonstrates the boundary conditions applied. A 10  $\mu\text{m}$  square unit cell is constructed with a grounded (electrical) and fixed (mechanical) boundary condition while a voltage of 1V is applied at the free boundary condition. The chosen poling direction is from the base to the top and in post-processing the results are normalized relative to the displacement simulated for pure PVDF. Figure 2.2 shows the displacement of pure PVDF under the applied boundary conditions.

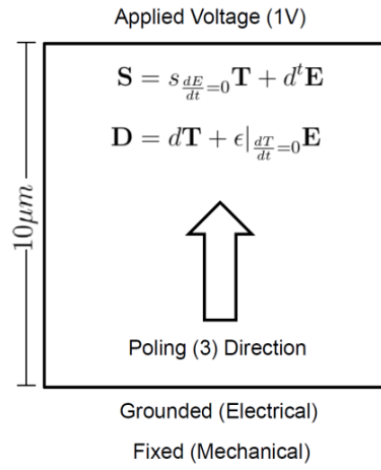


Figure 2.1 The fully defined piezoelectric problem with electrical boundary conditions and governing equations.

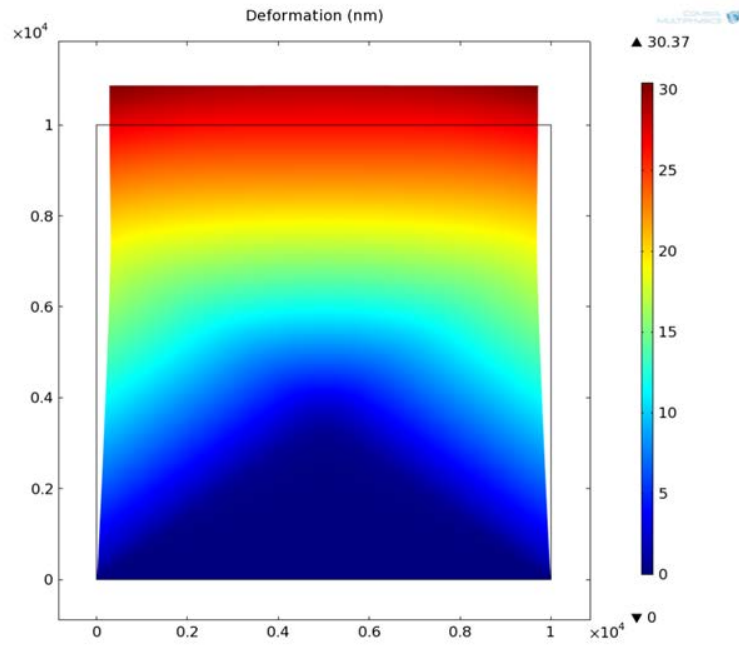


Figure 2.2 Deformation of a neat PVDF with 1V applied voltage and clamped boundary condition.

For adding carbon nanotubes to the model the simulation inputs are the number of carbon nanotubes and well as their dimensions. The nanotube geometry is generated by a random seed generator in a MATLAB® script and then imported into COMSOL using Live Link and solved with the COMSOL piezoelectric package. It is possible to run multiple tests using the same random seed. The weight fractions are converted from volumes by using a unit thickness assumption. The material inputs for the simulation are the compliance matrix, piezoelectric properties, electrical permittivity as well as densities to convert from areas to masses. The model uses fine mesh refinement using the free triangular method.

The electric field interaction within the film is the enabling phenomenon for improvements in the piezoelectric response. Through introducing potential concentrations through the addition of carbon nanotubes the local electric field can be increased, thus increasing the local strain. The net gain from these locally induced strain concentrations should result in a larger net displacement. Figures 2.3 and 2.4 show examples of the potential fields for both low and high aspect ratios which resulted in high deformations; the distinguishing features are the very large changes in potential with multiple maxima and minima. This produces large internal electric fields which correspond to higher displacements. The smaller aspect ratio case shows promise because if the carbon nanotube's can be controlled during manufacture it would allow for duplication of the effect and even higher enhancement of the piezoelectric effect.

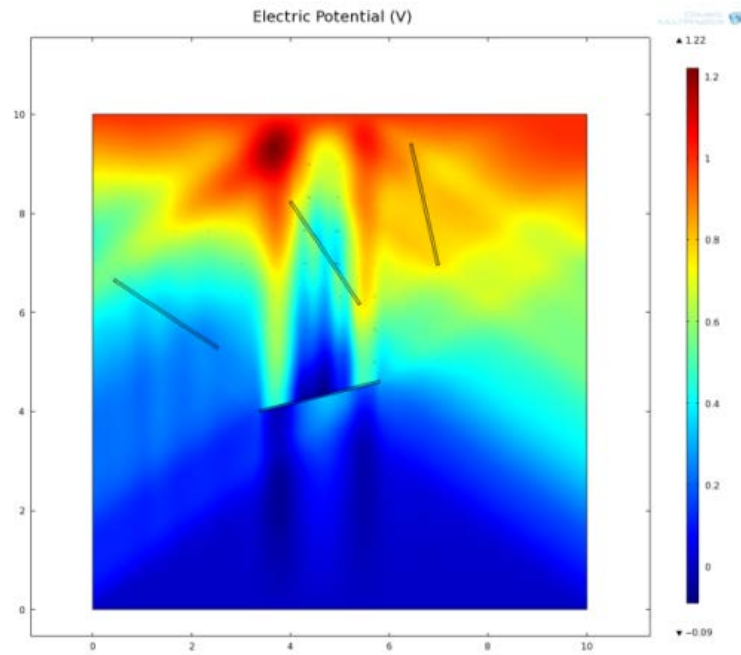


Figure 2.3 Electrical potential plot of carbon nanotubes with a high aspect ratio. Fewer nanotubes are present to keep the total weight-fraction constant.

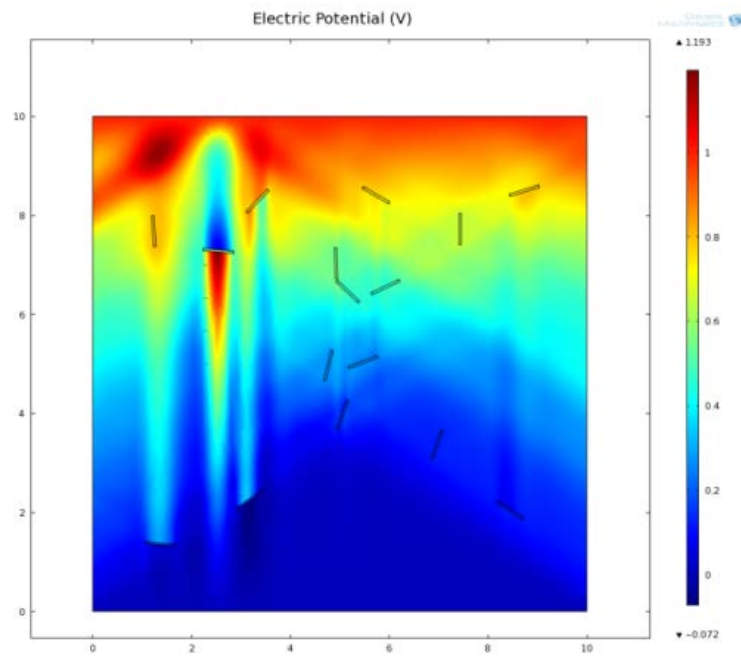


Figure 2.4 Electrical potential plot of carbon nanotubes with a low aspect ratio. More nanotubes are present to keep the total weight-fraction constant.

This effect has varying degrees of success in the enhancement of the piezoelectric effect depending on the geometry of the reinforcement. A series of simulations were conducted to examine the influence of concentration, alignment and aspect ratio. Although the simulation size is limited, the results highlight the importance of morphology on the piezoelectric response.

In order to see the effect of increasing nanotube concentration (by weight) the model was tested at with different number of carbon nanotubes. On the  $10\mu m \times 10\mu m$  unit cell, 1wt% corresponds to 20 carbon nanotubes with widths of  $50nm$  and lengths of  $1000nm$  giving an aspect ratio of 20. The results (Figure 2.5) show an overall possible increase in deformation that correlates to an increase in the amount of

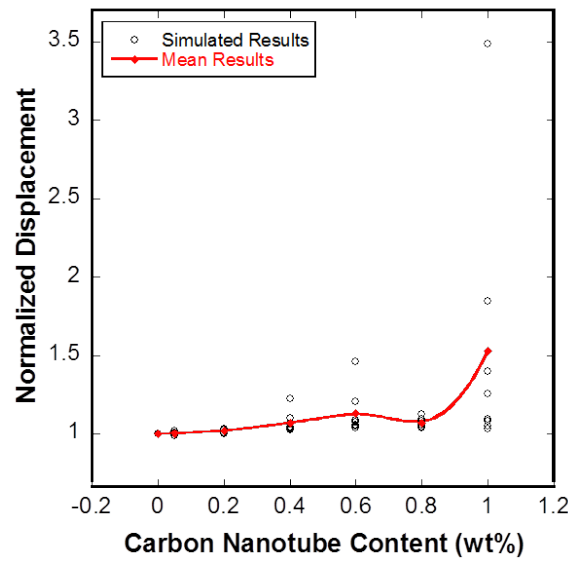


Figure 2.5 Influence of mass fraction of carbon nanotubes on the normalized displacement under an electric field.

carbon nanotubes included, suggesting a preference for higher concentrations of nanotubes. The test shows a strong dependence on geometric configuration, which, due to the random nature of the simulation results in a distribution of possible improvements.

The alignment of the nanotubes with respect to the poling direction was thought to have a significant effect on the effective increase in piezoelectric coefficient. The simulation used the same randomly distributed seed while defining a spread angle which represents the degree of freedom in rotation in each nanotube. The spread angle is increased from  $0^\circ$  to  $180^\circ$ , with  $0^\circ$  representing a perfectly aligned

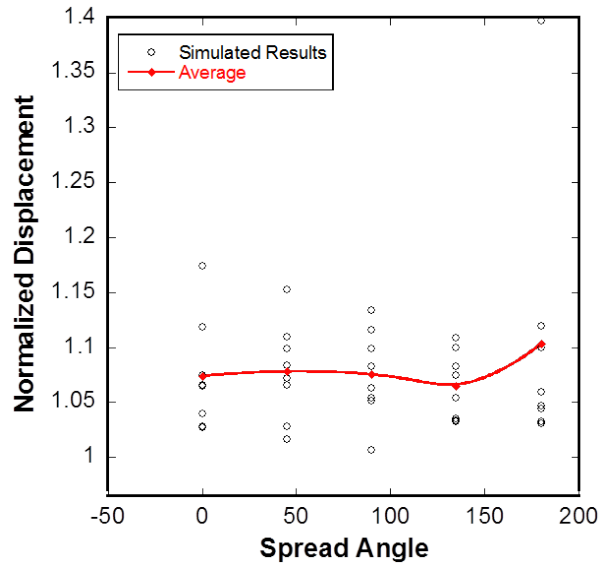


Figure 2.6 Influence of carbon nanotube alignment on the normalized displacement under an electric field.

composite and  $180^\circ$  a completely random composite. The rotation of each nanotube is determined by a second random seed. The results, shown in Figure 2.6, suggest that

constriction of the spread angle results in an increase larger numerical scatter, allowing for both larger and smaller displacements. The driving effect on the normalized displacement is the geometric configuration with nanotube-nanotube interactions having the largest influence on displacement.

There are two approaches taken in order to evaluate the effect of aspect ratio on the improvement of the piezoelectric properties. The first is a sweep of aspect ratios while keeping the total number of nanotubes constant and the second is a sweep of aspect ratios while keeping the volume fraction of nanotubes constant. The first method has two types of data associated with it: data which have a random seed for each aspect ratio, and data which use a consistent seed for differing aspect ratios.

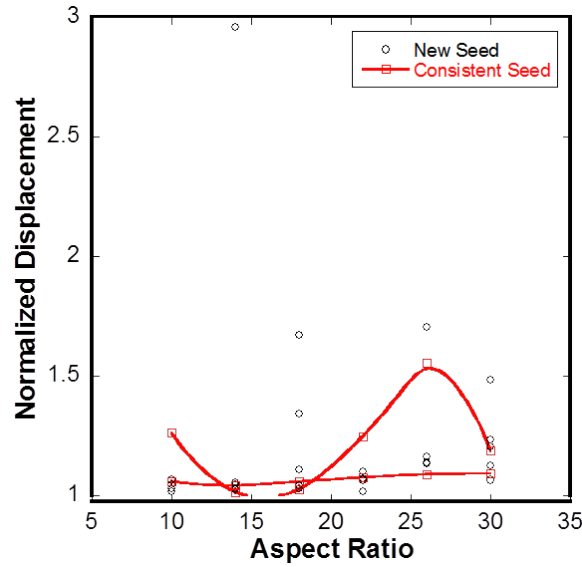


Figure 2.7 Influence of carbon nanotube aspect ratio on the normalized displacement under an electric field (constant number of nanotubes).

The first data set exhibits a high dependence on general geometry, shown in Figure 2.7. There is a slight trend in higher aspect ratios achieving higher displacement but in general the displacement seems to have a complex dependence on both aspect ratio and weight percent. It is shown that there is not a very significant difference between keeping a consistent random seed and refreshing it each time.

The second case, shown in Figure 2.8, maintains a constant volume fraction and demonstrates the ability of both low and high aspect ratio materials to achieve high degrees of improvement on the piezoelectric effect. There is a range in which the probability of high improvement is lowered. The improvements associated with electrical interactions between the nanotubes which are increased through having many smaller nanotubes or a few very few large nanotubes.

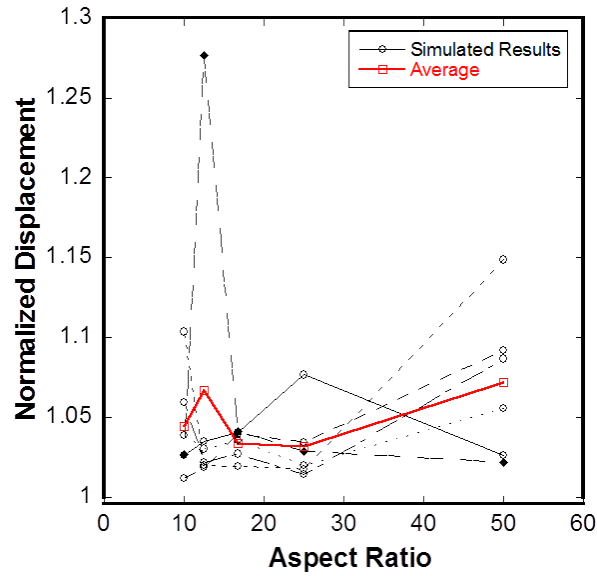


Figure 2.8 Influence of carbon nanotube aspect on the normalized displacement under an electric field (constant volume fraction).



Given the relatively large numerical scatter in the simulations of nanotube alignment, the rotation of a single carbon nanotube in an electric field was investigated to better understand the orientation effect on the electric field interactions. In addition, several cases that show the highest displacements were examined to visualize their internal electric fields. The piezoelectric effect was found to be highly dependent on the carbon nanotube orientation and has strong peak when the carbon nanotube is aligned  $10^\circ$  off-axis. When the carbon nanotube is rotated past  $35^\circ$  the composite begins to have a reduction in piezoelectric effect. The normalized displacements observed are relatively low, suggesting that nanotube-nanotube interaction effects play a much more important role than the orientation effects.

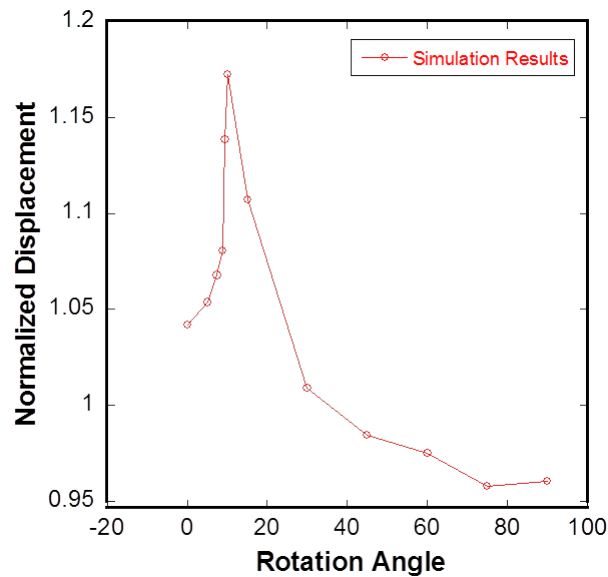


Figure 2.9 Influence of nanotube orientation on normalized displacement under an electric field (single nanotube).

Figure 2.10 shows potential plots at various different carbon nanotube rotation angles. When the carbon nanotube is closer to the aligned direction the large change in potential occurs along its length; while when it is closer to the perpendicular direction the large change in potential occurs across the carbon nanotube, itself. Because the displacement is proportional to the change in potential in the matrix, having most of the change occur across the carbon nanotube results in a loss, which corresponds to the reduced displacement at angles larger than  $35^\circ$ .

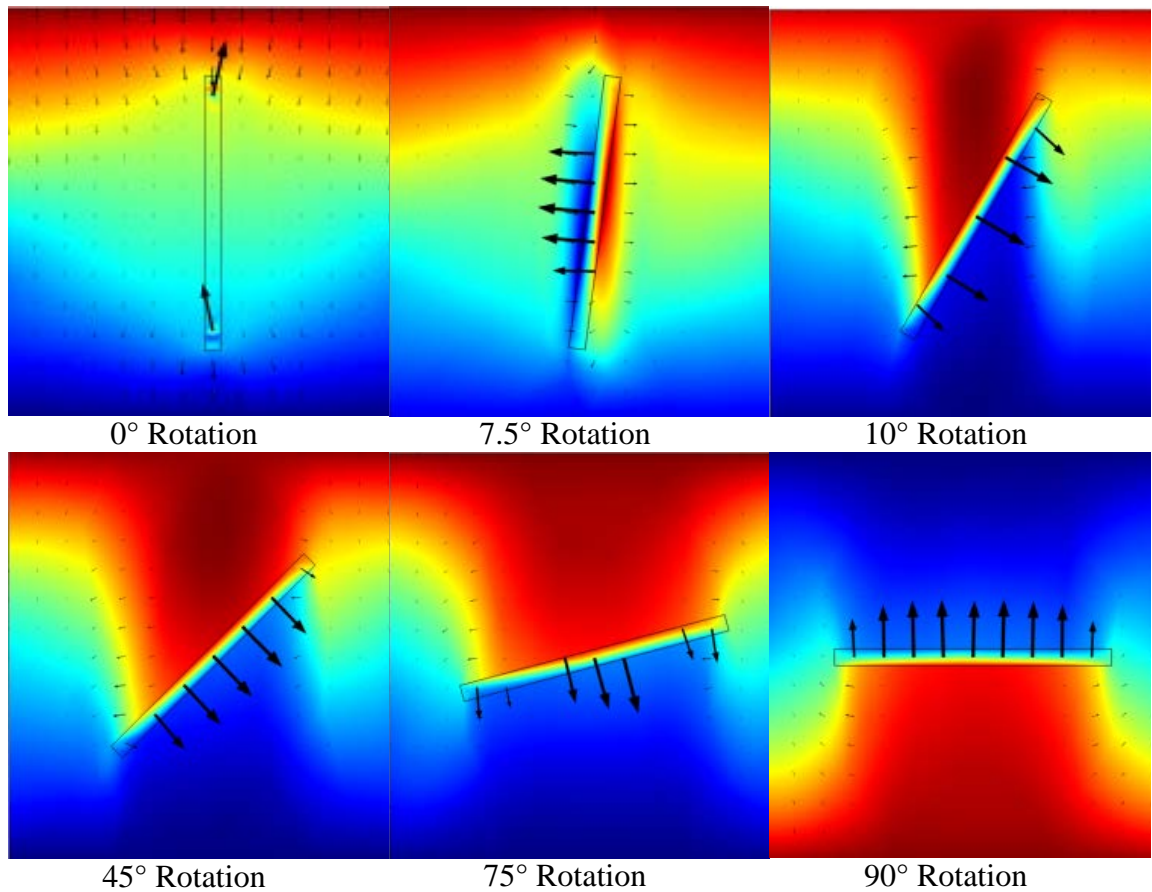


Figure 2.10 Contour plots of electric potential of a single nanotube within a PVDF matrix at different rotations. Boundary conditions are 0V and 10V which set the scale for the contour.

The numerical results show that some of the stochastically generated geometries outperform the others by far. Analysis into these geometries can lead to insights in what forms of microstructures produce the best increase in the piezoelectric effect. Several cases were singled out from the data and their potential plots are shown Figure 2.11. Underneath each contour plot shows the normalized displacement. The

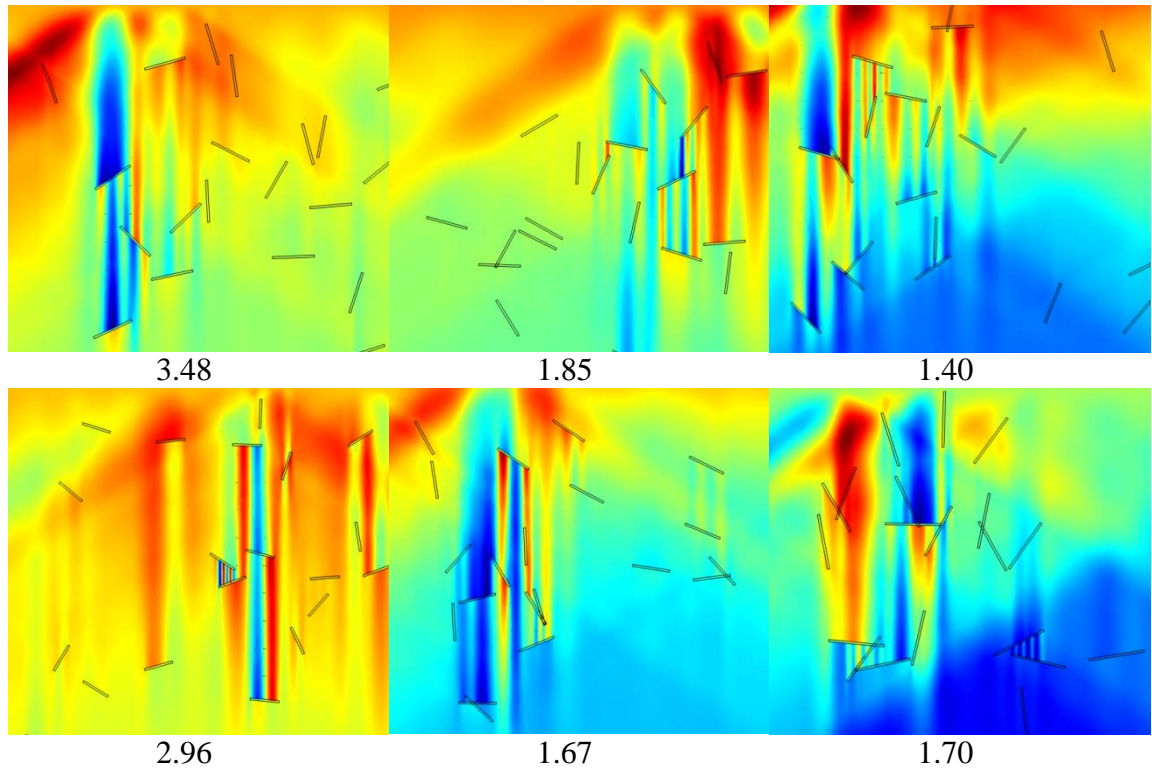


Figure 2.11 Electric potential plots of a single various stochastically distributed geometries which resulted in abnormally high normalized displacements (normalized displacement shown under contour plot).

highest effect on normalized displacement comes from distributions where the carbon nanotubes are arranged slightly off axis from the perpendicular direction in quasi-parallel strips. This causes banding in the potential field and as a result very large

spikes in electrical field (and deformation). These simulations also confirm that nanotube-nanotube interactions play the most important role in the enhancement of the piezoelectric effect.

The benefits of adding carbon nanotubes are clear, and while the fundamental physics are well understood, the way that they interact is much more complicated. The simulations shed light on the interactions between nanotubes and builds intuition into how they can be optimally organized for improvement of the matrices piezoelectric properties. The evaluation of the most-optimal geometries gives insight into which manufacturing processes (in this case, electrospinning) can be used to manufacture such a system.

## **2.2 3-Dimensional Modeling of Nanocomposite Piezoelectric Coefficients**

While the 2-dimensional simulations shed light on some of the key parameters that influence the piezoelectric response they are limited in terms of their size and also cannot account for other factors, such as nanotube waviness. In order to evaluate the complex 3-dimensional shapes while being computationally efficient and thorough a different modeling approach is taken. Here the electric fields are calculated for the 3-dimensional model at all points, this is then used as the basis for calculating an effective piezoelectric coefficient and allows for isolation of the electrical effects from the stiffness effects.

### **2.2.1 Simulation Methodology**

The constitutive equations can be expressed in the strain-charge form:

$$S = sT + d^t E \quad (2.1)$$

$$D = dT + \epsilon E \quad (2.2)$$

where  $S$  is the strain tensor,  $T$  is the stress tensor, and  $E$  is the electric field. The material properties are represented as the compliance matrix  $s$ , the electrical permittivity  $\epsilon$ , and the direct piezoelectric coefficient  $d$ . In the ideal case, the inverse piezoelectric effect is described as the transpose of the direct piezoelectric coefficient  $d^t$ . Because the piezoelectric coefficient relates electric field (a 1<sup>st</sup> order tensor) to strain field (a 2<sup>nd</sup> order tensor), it can be written as a 3 x 6 matrix:

$$d = \begin{bmatrix} 0 & 0 & 0 & 0 & d_{15} & 0 \\ 0 & 0 & 0 & d_{24} & 0 & 0 \\ d_{31} & d_{32} & d_{33} & 0 & 0 & 0 \end{bmatrix} \quad (2.3)$$

In the majority of practical applications the most important value is  $d_{33}$ , relating strain generated in the direction of the applied electric field strength. The  $d_{33}$  coefficient is also commonly the largest of the piezoelectric coefficients so it is often used as the primary metric of piezoelectric performance. For homogenous materials, the only way of directly improving the piezoelectric effect of the material is by changing the structure in order to improve  $d$  – the electric field is constant throughout the material. However, for a heterogeneous structure,  $E$  is a function of space and can vary within the structure and becomes another way of improving the material.

The focus of this work is in understanding the impact of mico-scale geometric configuration on the influence of the piezoelectric properties of PVDF via the introduction of carbon nanotubes. Typically, increasing the geometric complexity has a large penalty on computation time and difficulty of simulation; however, because the primary interest is in the impact of carbon nanotubes as electrical reinforcement (rather than structural reinforcement) the simulations are formulated to calculate the stress-free equivalent piezoelectric coefficient due to carbon nanotube enhanced electric field. Equivalently, this study is concerned with studying piezoelectric

improvement due to electric field enhancement. The piezoelectric component of the equation is:

$$S = d^t E \quad (2.4)$$

For a material with heterogeneous conductivity, the carbon nanotubes greatly affects  $E$ , making it a function of space in the PVDF, whereas the  $d$  values remain the same (throughout the PVDF). The strain induced in the direction of the electric field, correlating with the  $d_{33}$  coefficient is of great importance.

$$S_3 = d_{33} E_3 \quad (2.5)$$

A simple metric for the improvement gained through enhancement of the electric field is to calculate the “effective piezoelectric coefficient” required to treat the system with a uniform electric field:

$$d_{33,eff} E_u = d_{33} E_3 \quad (2.6)$$

or

$$d_{33,eff} = \frac{S_{cnt}}{E_u} \quad (2.7)$$

where  $S_{cnt}$  is the stress-free-strain generated with a carbon nanotube reinforced PVDF. Application of a stress-free boundary condition results in the strain induced in the 3-direction generating a displacement on the top and bottom surfaces  $D_1$  and  $D_2$  (see Figure 2.13).

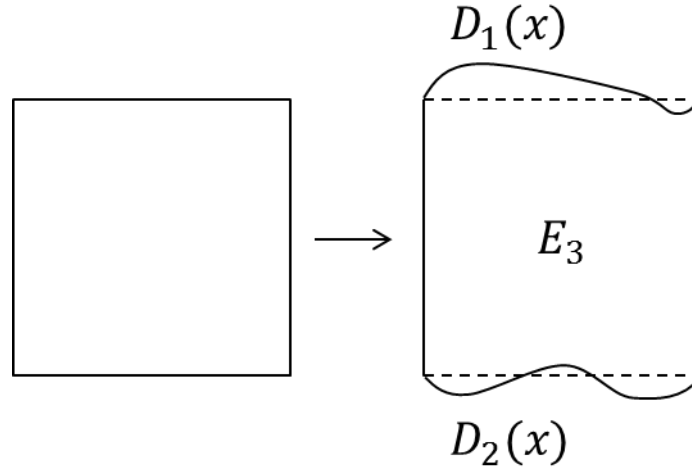


Figure 2.12 Illustration of displacement produced on top and bottom surface due to the piezoelectric effect with a heterogeneous electric field.

The total deformation as a function of  $x$  is:

$$D(x) = D_1(x) + D_2(x) \quad (2.8)$$

The deformation is related to the strain in the PVDF:

$$D_y(x) = \int \epsilon(x, y) dy \quad (2.9)$$

Then the volume change  $V$  can be calculated as:

$$\Delta V = \iint \epsilon(x, y) dy dx \quad (2.10)$$

Simplifying to:

$$\Delta V = \int \epsilon(x, y) dV \quad (2.11)$$

and discretized to:

$$\Delta V = \sum_{i=1}^n \epsilon_i V_i \quad (2.12)$$

Expressing strain in terms of electric field and piezoelectric coefficient:

$$\Delta V = \sum_{i=1}^n E_i d_{33} V_i \quad (2.13)$$

and calculating volumetric strain:

$$S_{cnt} = \frac{\Delta V}{V} = \frac{1}{V} \sum_{i=1}^n E_i d_{33} V_i \quad (2.14)$$

$$S_{cnt} = \frac{d_{33}}{V} \sum_{i=1}^n E_i V_i \quad (2.15)$$

which can be used in conjunction with Equation # to solve for the effective piezoelectric coefficient:

$$d_{33,eff} = \frac{d_{33}}{V_{Eu}} \sum_{i=1}^n E_i V_i \quad (2.16)$$

### 2.2.1.1 Pre-Processing Architecture

Designing and creating the geometry for the carbon nanotube infused PVDF film is broken up into three main components: 1) the geometry of the individual carbon nanotubes are described using a MATLAB script which describes carbon nanotube diameter, length, and waviness, 2) the dispersion of the carbon nanotubes is described by a MATLAB script which prescribes the position and rotation of each carbon nanotube, 3) creation of the parts for simulation is done via interpreting the MATLAB generated parameters in CATIA solid modeling software. These models are then transferred to ANSYS for finite element analysis, and the results are post processed in MATLAB in order to understand the effect of heterogeneous electric field on the piezoelectric strength, and to reduce data from multiple experiments in order to account for the stochastic distribution of carbon nanotubes. Figure 2.14 schematically describes the flow of information through the various software components.



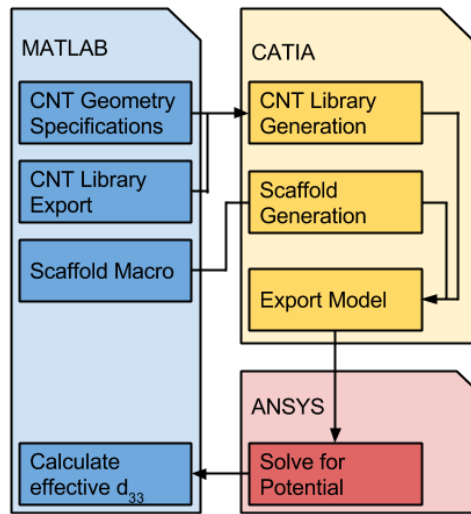


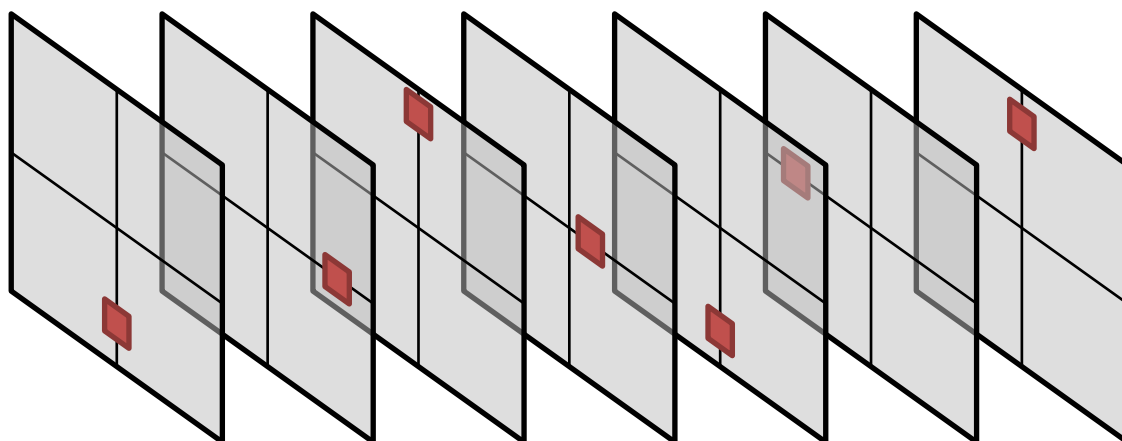
Figure 2.13 Schematic description of information flow through software. MATLAB is used in order to fully describe the geometry of both individual carbon nanotubes, and the nanotube dispersion. CATIA then interprets the MATLAB produced description and generates a solid model. ANSYS uses the CATIA-produced model in order to use finite element analysis to calculate the electric field distribution. Lastly, MATLAB is used to interpret each data set and calculate the effect of the electric field on effective piezoelectric strength.

#### 2.2.1.2 Carbon Nanotube Geometry: Waviness

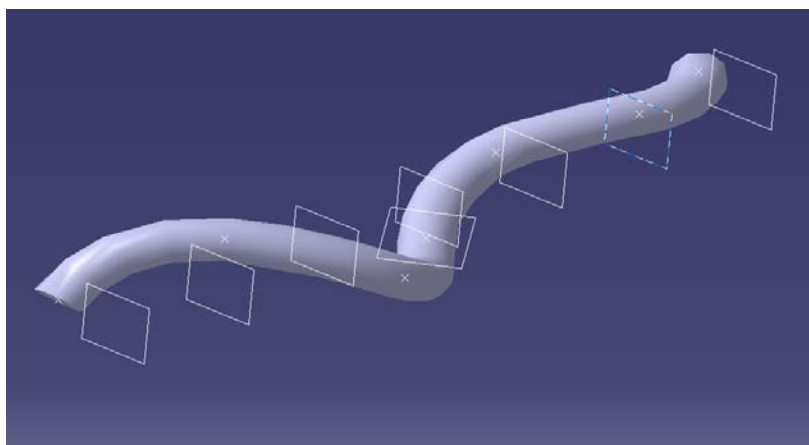
For the studies involving weight percent, aspect ratio, and alignment, straight carbon nanotubes were used. The diameter was maintained at a constant 50nm, and the length was changed to affect the aspect ratio. In order to convert from volumes to weight percent's densities of 2.26 g/cc and 1.78 g/cc were used for carbon nanotubes and PVDF respectively.

It is widely known that nanotubes are not straight rods, but rather have an overall waviness – acting more like small non-continuous fibers. In order to evaluate the effect of this waviness it is essential to design a methodology for constructing wavy nanotubes in three dimensions. In order to generate fully three dimensional

carbon nanotubes, a series of 7 planes were placed in parallel for construction. The waviness is controlled by extruding a circle (the nanotube profile) along a spline through points defined by coordinates on each plane (see Figure 2.15a). The point positions are defined by a Matlab script, which ensures that the carbon nanotube only makes quarter turns and stochastically assigns a value for the distance between the points and the center of each plane. The waviness of the carbon nanotube is determined by the maximum distance the points are allowed to position from the center of the planes, and is given as a ratio to the diameter of the carbon nanotube. Waviness ratios range from 1 being a straight carbon nanotube with no waviness to 4 meaning that the carbon nanotube waviness is allowed to be up to 4 times the carbon nanotube diameter. These points are all controlled in CATIA using a design table, and a library of carbon nanotubes is generated for each waviness ratio. Figure 2.15b is an example of a generated wavy carbon nanotube using this approach.



(a)



(b)

Figure 2.14 Schematic showing the planes and coordinates used for extruding the carbon nanotube solid model. A spline is constructed through points (small squares) which are given as x-y coordinates on a series of planes (large squares) ensuring the nanotube does not twist over itself by restricting it to quarter turns (clockwise or anti-clockwise). b) Screenshot of a CATIA model used as an example of the as produced carbon nanotube solid model.

### 2.2.1.3 Carbon Nanotube Dispersion, Orientation and Mesh Generation

In order to describe the position of each carbon nanotube within the matrix there are six degrees of freedom, three special coordinates and three orientation coordinates. First, a cloud of point-pairs is generated:  $p1_n$  and  $p2_n$ . The location of each carbon nanotube is given by  $p1_n$  by simply assigning spatial coordinates by a random number generator. The location of  $p2_n$  is restricted in the z-axis (electrospun composite would force the carbon nanotubes to be pseudo-parallel with the surface of the film) and its planar location is given as a rotation in reference to the position of  $p1_n$ . In order to define the orientation of each carbon nanotube, they are given an angle profile which models a normal distribution with a mean representing perfect alignment using the probability distribution function [58]. Using standard deviations to characterize this distribution, a deviation of 0 represents perfect alignment, whereas a standard deviation of  $\pi$  represents the fully random case. To visualize alignment dispersion, it is helpful to plot them on a rose plot (see Figure 2.16); these are effectively radial histograms showing the frequency of the angles of each carbon nanotube as generated by the positioning algorithm.

Once the scaffold is created, it is populated with carbon nanotubes from the carbon nanotube library, and subsequently placed and oriented based on the point-pair cloud using it as a scaffold to arrange the nanotubes. A matrix is built as a homogenous thin film with the carbon nanotubes subtracted from it using Boolean operations, and the carbon nanotubes themselves are added as a separate part so they can be easily assigned different material properties in ANSYS Figure 2.17 shows an example of the generated carbon nanotube-PVDF model, demonstrating a random dispersion of wavy carbon nanotubes.

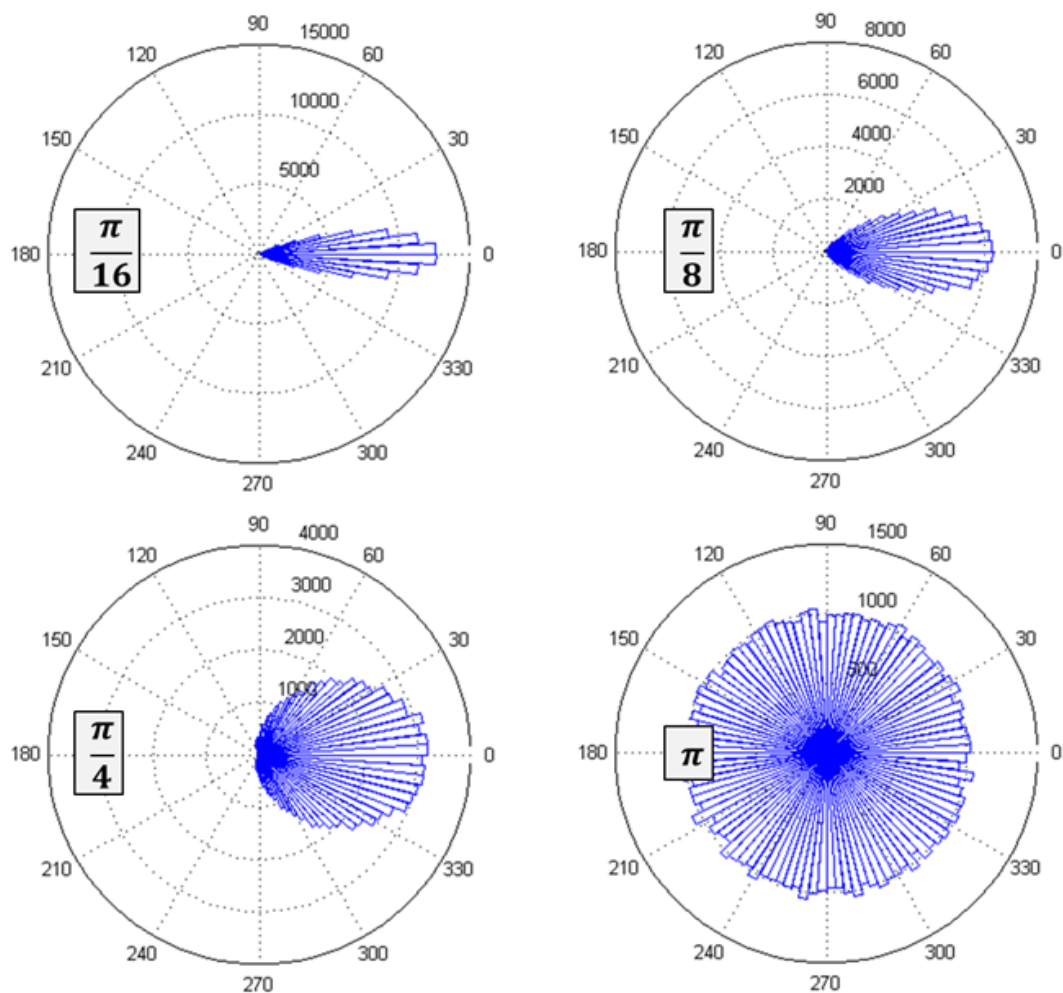


Figure 2.15 Radial histogram showing distribution of angles of each carbon nanotube in the dispersion with the associated standard deviation. A standard deviation of  $\pi/16$  gives highly aligned carbon nanotubes and, as it is increased, the quality of the alignment degrades until reaching a standard deviation of  $\pi$ , which generates a randomly oriented dispersion.

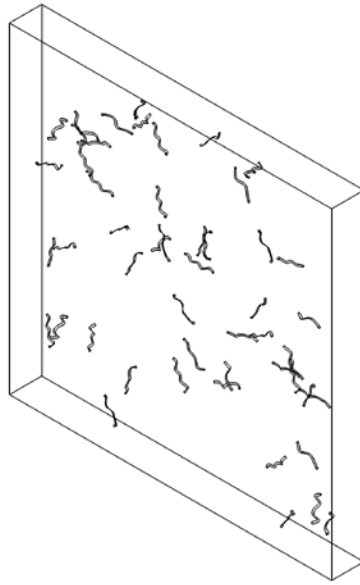


Figure 2.16 Example of modeled geometry using a 0.1 wt% of carbon nanotubes with a maximum waviness of 4 times their diameter, an aspect ratio of 32, and fully random orientation.

#### 2.2.1.4 ANSYS Simulation

After importing the geometry into ANSYS the PVDF is assigned a resistivity of  $10^{11}$  ohm-m and the carbon nanotubes, a resistivity of  $10^{-5}$  ohm-m. As boundary conditions a voltage of 10V was applied to one face and the other was grounded. A mesh refinement study was done to determine the minimum necessary meshing parameters for simulation (Figure 2.18), however, due in part to ANSYS' dynamic mesh refinement algorithm, the results for all but the coarsest meshes were unaffected. The mesh parameters used are summarized in Table 2.1. Because of the stochastic nature of carbon nanotube dispersion, 5 simulations were run for each parameter change in the study in order to reliably portray each effect, each simulation contains between 0.4M and 1M elements.

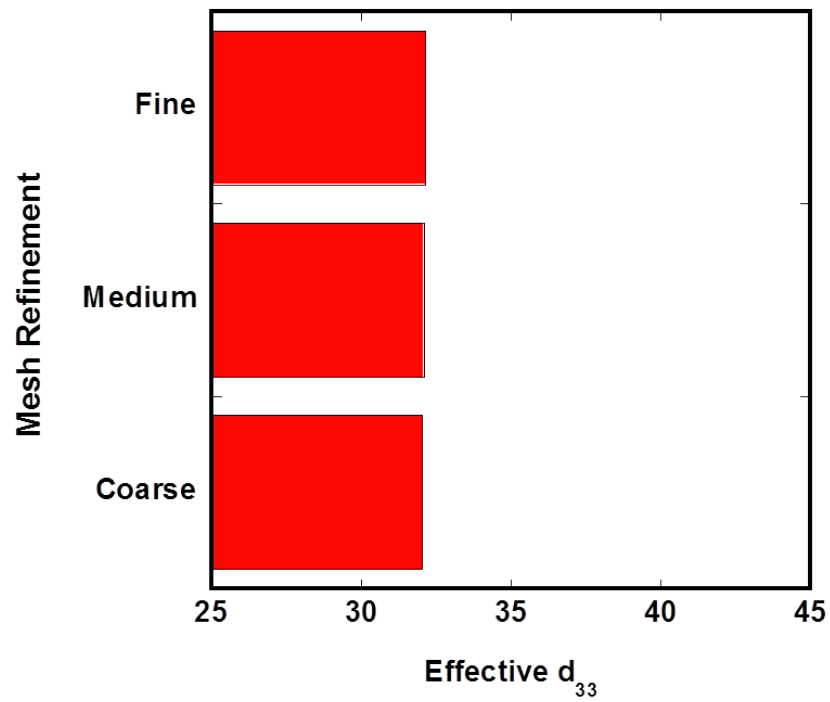


Figure 2.17 Changes in effective piezoelectric coefficient with differing levels of mesh refinement.

Table 2.1 List of meshing parameters used by ANSYS.

| Parameter                      | Value                   |
|--------------------------------|-------------------------|
| Adaptive Mesh Refinement Loops | Max of 3, depth of 2    |
| Relevance                      | 0 (default)             |
| Advanced Size Function         | Proximity and Curvature |
| Relevance Center               | Medium                  |
| Initial Size Seed              | Active Assembly         |
| Smoothing                      | Medium                  |
| Transition                     | Slow                    |
| Span Angle Center              | Coarse                  |

### 2.2.2 3-D Simulation Results and Discussion

After all of the models are created and boundary conditions are initiated the results for each study are plotted. Once the model is solved, the easiest way to visualize the electric field is by plotting the 3D voltage potential. In order to show the effect of the carbon nanotubes, it is essential to slice the matrix in order to reveal the internal structure; this can be done for several test cases to help visualize the solver output. Figure 2.19a shows a PVDF matrix with fully randomly dispersed carbon nanotubes with an aspect ratio of 4 and a weight percent of 0.1%, while Figure 2.19b shows the problem where the nanotubes have an aspect ratio of 32 and have the same weight percent or 0.1%.

While studies pertaining to dispersion and weight percent are very similar, it is also useful to visualize the internal electric field topology when the carbon nanotubes are wavy. Figure 2.20 shows a configuration with a weight percent of 0.1%, a cap-to-cap distance of 800nm and maximum waviness amplitude of 3 times the carbon nanotube diameter.

The first parametric study is an analysis on the influence of aspect ratio. In order to isolate aspect ratio, the length of the added nanotubes is controlled and the number of carbon nanotubes adjusted in order to keep the weight percent constant at 0.1% because of its commonality in research involving carbon nanotubes dispersed in a polymer. The results (Figure 2.21) show an increase in effective  $d_{33}$  as the nanotubes become shorter (reduced aspect ratio), and a local maximum when the aspect ratio is at 32.



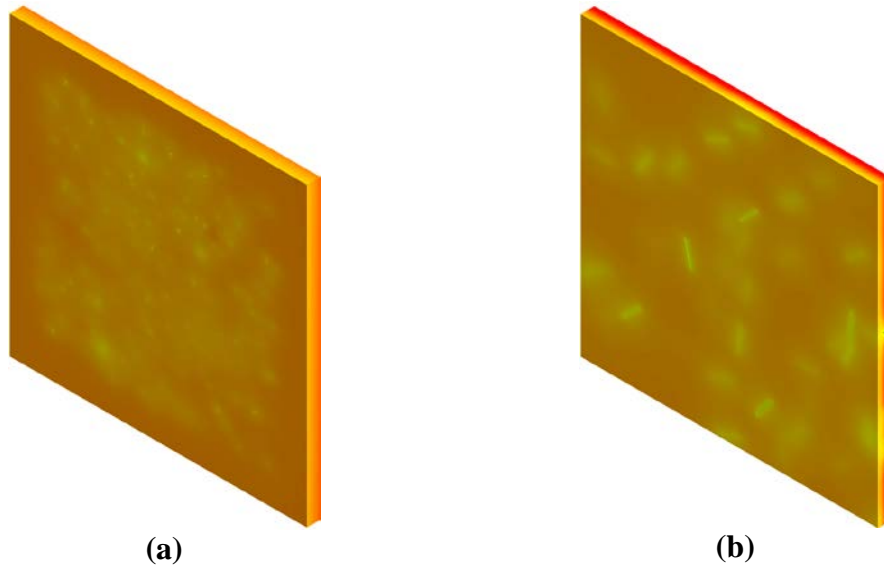


Figure 2.18 Examples of electric potential (voltage) in the cross section of simulations with (a) PVDF matrix with fully randomly dispersed carbon nanotubes with an aspect ratio of 4 and a weight percent of 0.1% and (b) changing the aspect ratio to 32 with the same weight percent.

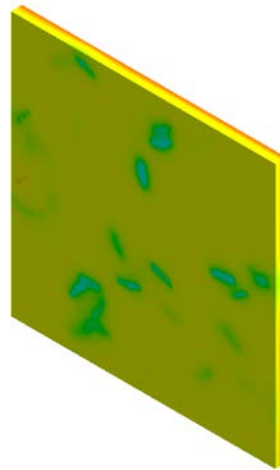


Figure 2.19 Example of electric potential (voltage) on a cross section of a simulation for PVDF containing 0.1wt% of carbon nanotubes with a maximum waviness of 3 times the nanotube diameter.

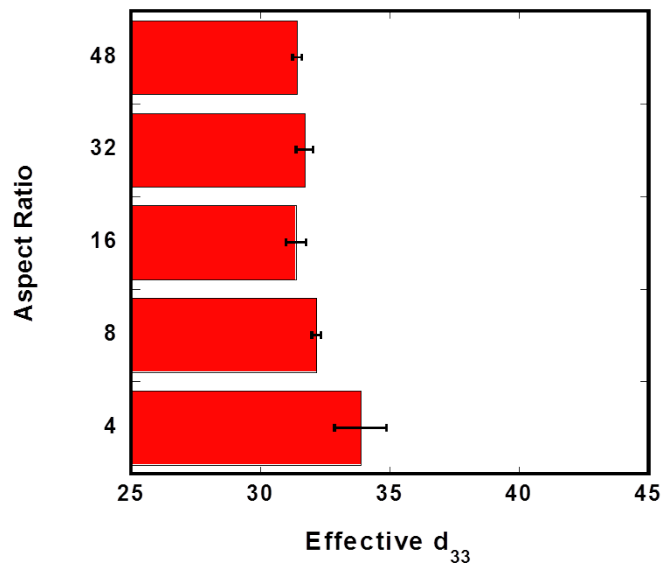


Figure 2.20 Effective  $d_{33}$  as influenced by aspect ratio with a weight percent of 0.1%, constant nanotube diameter, and fully unaligned dispersion. An increase can be seen as the aspect ratio becomes smaller and the number of carbon nanotubes increases.

The next parametric study is an analysis of the influence of the amount of carbon nanotube reinforcement on the effective  $d_{33}$  of the film. The weight percent is increased by adding carbon nanotubes, keeping the aspect ratio fixed at 16 (the local maximum from the previous study), and calculated so that it increases from 0 to 0.25wt%. The results, shown in Figure 2.22, show both an increase in effective  $d_{33}$  as well as an increase in variability for each experiment. It is important to note that as the weight percent approaches 0.25wt% it becomes statistically far more likely for the material to “short out”; in which case the simulation fails (as would the real-world material). This is caused by the formation agglomerates which form clusters and cause the material to be above the percolation threshold and is further looked at in the last part of this study.

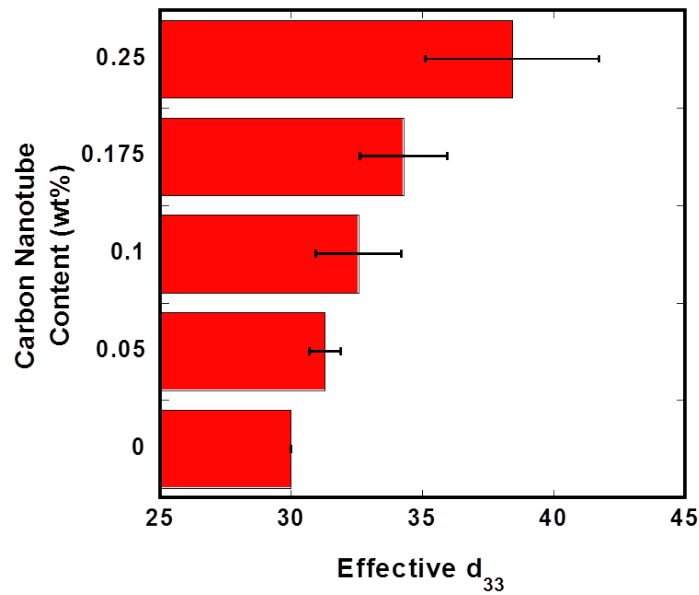


Figure 2.21 Effective  $d_{33}$  plotted against carbon nanotube (carbon nanotube) content in weight percent with constant aspect ratio and fully unaligned dispersion. An increase in carbon nanotube content (and number of carbon nanotubes) produces an increase in effective  $d_{33}$ .

Next, the orientation angle is varied while again keeping the weight percent fixed at 0.1% with an aspect ratio of 16. The standard deviation is shifted from 0 (perfectly aligned) to  $\pi$  (fully random). The results, shown in Figure 2.23, indicate that there is little change in effective  $d_{33}$  with respect to orientation. Because the orientation shift is in-plane, this is expected.

Lastly, the waviness of the carbon nanotubes is studied; the waviness is adjusted as a ratio to the carbon nanotube diameter, starting with flat nanotubes and progressing to nanotubes that are allowed to undulate up to 2, 3, and 4 times their diameters. Once again (Figure 2.24), there are only marginal changes in the effective  $d_{33}$  when the waviness amplitude is changed.

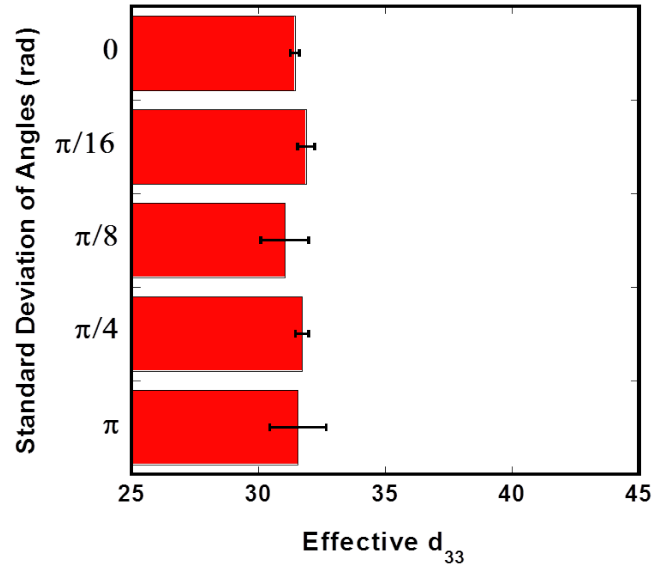


Figure 2.22 Effective  $d_{33}$  plotted against carbon nanotube in-plane orientation with constant weight percent and constant aspect ratio. Orientation is given as the standard deviation of carbon nanotube angles.

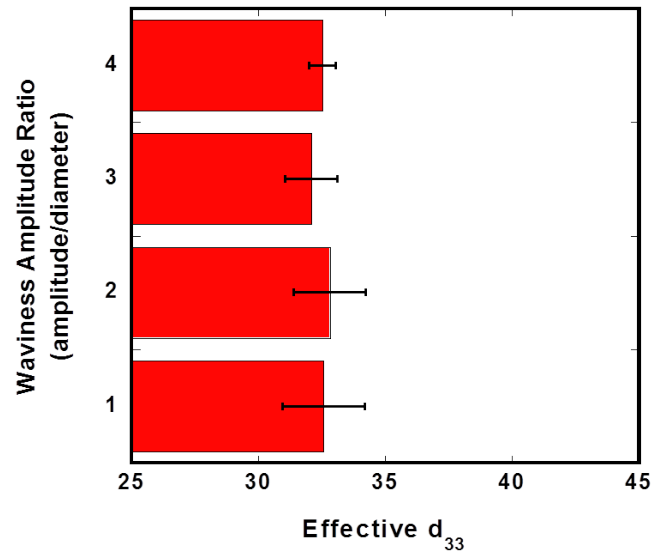


Figure 2.23 Waviness, as a ratio of amplitude to carbon nanotube diameter, is plotted from 1 to 4 with constant weight percent, constant cap-to-cap distance, and completely random dispersion.

Because there are the large changes with respect to aspect ratio and weight percent and small changes due to waviness and orientation, the current hypothesis is that the driving characteristic for improving the effective  $d_{33}$  is the number of well distributed carbon nanotube ends. Both increase in weight percent (constant aspect ratio) and decrease in aspect ratio (constant weight percent) result in an increase in the number of carbon nanotube ends, which can act as electric field concentrators – creating localized areas of high voltage gradients. Because of the applied voltages, the average electric field of the whole film must always be constant, but by adding more end caps, the areas of lower electric field strength are sequestered to within the carbon nanotubes between the end caps. This means that the high strength electric field must exist in the piezoelectric PVDF component.

The enhanced  $d_{33}$  is wholly dependent on maintaining a planar high quality dispersion of carbon nanotubes; if the nanotubes begin to agglomerate, then they can create a short-circuit between both surfaces, resulting in the entirety of the voltage gradient existing within the carbon nanotubes. This causes the average electric field within the PVDF to drop to near-zero along with the effective  $d_{33}$ . Figure 2.25 shows an example of a transversely oriented carbon nanotube agglomerate forming a spanning cluster and shorting out the film. In this case the bounding box of carbon nanotube distribution was heavily reduced and simulation tweaked in order to force an agglomeration and allow the finite element software to handle it without crashing.

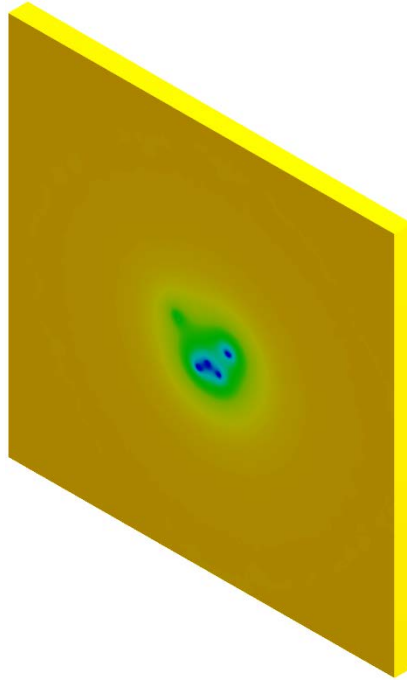


Figure 2.24 Example of a transversely oriented spanning cluster demonstrating what happens if a carbon nanotube agglomerate exists in the film (a typical problem when solution casting). The potential field (voltage) is plotted in the brief moment prior to failure to show that this agglomerate would result in a short circuit and an inability to sustain the electric field.

### 2.3 Conclusions

This work was completed in two separate studies. The initial study was a 2-dimensional finite element analyses (FEA) study using the COMSOL Mutliphysics platform which was used to study the effect of carbon nanotubes on the piezoelectric response and found a strengthened effect from the manipulation of the electric field. This study included the effects of both mechanical and electrical properties of the material. The study shows an improvement in piezoelectric strength when the carbon nanotubes were aligned perpendicular to the electric filed, a strong improvement when increasing the weight percent of carbon nanotubes, and demonstrated that response to

changes in aspect ratio were bimodal. Improvements were also achieved for both very small and very large aspect ratios. The effect was demonstrated to work by locally increasing the electric field strength and thus producing more strain in those areas, however there were a few limitations in the study – because the model was two dimensional, there was no differentiation between carbon nanotubes and carbon platelets; the carbon nanotube geometry was forced to be very simplistic, modeled by rectangles (no waviness), and the dispersion of the carbon nanotubes was very rigid.

To overcome these limitations a 3-D simulation methodology was employed. These simulations showed that lowering the aspect ratios of the carbon nanotubes was found to result in an improvement of the piezoelectric properties of the PVDF film. Similarly an increase of weight percent carbon nanotubes resulted in increases in piezoelectric coefficient. Both the in-plane alignment and waviness of the carbon nanotubes were studied; however, neither of these parameters had a significant effect on the piezoelectric coefficient of the PVDF film.

The effect of electric field enhancement on piezoelectric strength can be explained by observing that increases in piezoelectric strength are related to the number of carbon nanotube end-caps; this may be due to each carbon nanotube ending producing an electric field discontinuity which locally increases the strain produced by the piezoelectric material. Decreasing the aspect ratio while maintaining the weight content of carbon nanotubes results in a large increase of carbon nanotube end caps, as does increasing the number of carbon nanotubes when studying the effects of increased weight percent. Conversely, neither the alignment nor the waviness affects the number of nanotube end-caps, and as a result, the improvements in piezoelectric

coefficient are small compared to normal variation due to the stochastic nature of the carbon nanotube dispersion.

Here it is demonstrated that the driving phenomenon in improvement of the piezoelectric effect within the material is the number of carbon nanotube “ends” – translating into high weight percent content and low aspect ratios. It is also demonstrated that reaching the percolation threshold is detrimental to piezoelectric performance in the film. These results motivate further study by suggesting that the optimal platform for improvements in piezoelectric properties can be found by using a high loading but below the electrical percolation threshold method by embedding carbon nanotubes in a PVDF matrix.



### **Chapter 3**

#### **ELECTROSPINNING PVDF WITH CARBON NANOTUBE REINFORCEMENT**

There are several noteworthy results from the finite element simulations which are of key importance when developing a method to disperse carbon nanotubes. The simulation results showed that in order for the conductivity of the carbon nanotubes to impart the largest positive effect on the piezoelectric coefficient of the material, the number of carbon nanotubes must be as high as possible while staying below the percolation threshold. Electrospinning was chosen as a method of processing the reinforced material because the submicron fibers are large enough to fully encapsulate the carbon nanotubes. The spinning process is also rapid enough such that the nanotubes do not re-agglomerate in solution. At the same time, it is hypothesized that the fibrous morphology will separate the nanotubes from each other and prevent the formation of spanning clusters, thereby raising the percolation threshold.

Three generations of electrospinning systems were used for this work (see Appendix A). The first generation system was very simplistic and was not consistent enough to be used for a rigorous study; however it did play a part in informing the design of the second, Mark<sup>1</sup> II system. The Mark II included flow rate control, significantly improved voltage control, and a Faraday cage for noise reduction and

---

<sup>1</sup> The “Mark” designation is a commonly used method of designating a version of product.

focusing. Subsequently, the Mark II system informed the design of the Mark III system, which added highly articulate injection needle arms and a full environmental control chamber. This chapter is therefore organized by electrospinning results between the Mark II and Mark III electrospinning system.

### **3.1 Electrospinning with the Mark II System**

The focus of the MARK II electrospinning system is to implement improvements in the level of control over the process variables in order to improve sample-to-sample consistency. An emphasis was placed on computer control and automation of the data acquisition process in order to ensure that all process variables were recorded and any process was repeatable. In-house computer software was written which oversees the entire process while recording all variables (dynamic, static and characteristic). The same software controls the dynamic variables during the electrospinning process. In addition, a Faraday cage was added around the apparatus in order to provide a potential ground plane; the cage keeps a consistent electric field within the electrospinning apparatus, as well as inhibiting unintended fiber collection on nearby surfaces. These variables (along with their respective control schemes) are listed in Table 3.1.

As shown in Figure 3.1 the electrospinning equipment consists of a two-pole computer controlled high voltage power supply (ES Series, Gamma High Voltage Research) with negative and positive from a reference ground and a pair of computer controlled syringe pumps (Dual-NE-1000, New-Era Pump Systems) which feed the fluid and power into the electrospinning apparatus. The apparatus itself is constructed using acrylic for its high stiffness and electrical isolation. Geometric parameters are controlled by a series of set screws on pieces which can slide relative to one another.

Two injector needles are held by sliders which allow for independent change in the projected distance between the center point of the collector plate and each needle. The distance-to-target can be adjusted in a similar matter. In addition the apparatus is surrounded by a tubular Faraday cage which allows for focusing through the use of collector/injection voltage disparity. For more details on the configuration of the mark II electrospinning apparatus, refer to Appendix A.

Rigid control over static variables and high tolerance on dynamic variables allows for greater consistency in processing as well as added capability for multi-jet electrospinning. During testing of the Mark II system it was also observed that environmental conditions, most notably humidity, had a very large effect on the consistency of samples produced. In order to mitigate these effects the results were gathered during the same time of day during the same season (summer in Delaware). This knowledge heavily informed the design of the Mark III system.

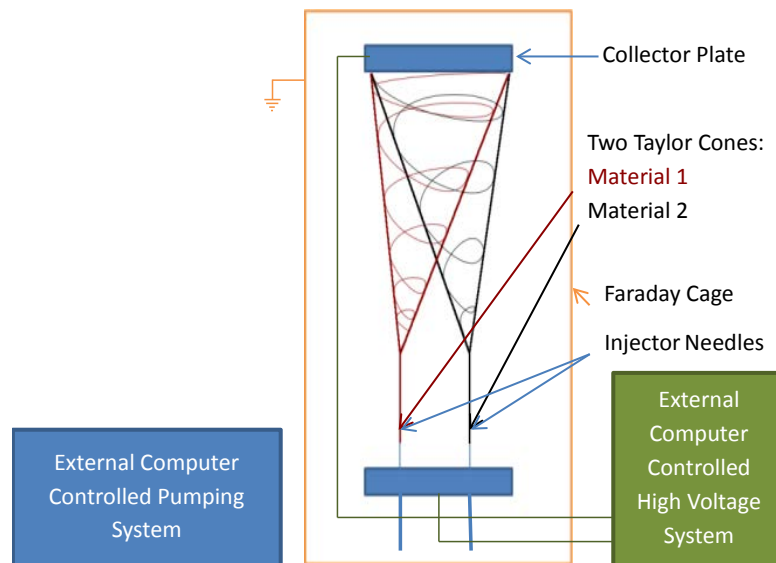


Figure 3.1 Mark II electrospinning apparatus.

Table 3.1 Mark II electrospinning process conditions

| <b>Variable</b>                                  | <b>Control Scheme</b>                             |
|--------------------------------------------------|---------------------------------------------------|
| <b>Weight Concentration of PVDF in DMF</b>       | Characteristic: Recorded (typ: 25 wt%)            |
| <b>Weight Concentration of Nanotubes in PVDF</b> | Characteristic: Recorded (typ: 0.1wt%)            |
| <b>Sonication Time (when applicable)</b>         | Characteristic: Recorded (typ: 15 minutes)        |
| <b>Extrusion Time (when applicable)</b>          | Characteristic: Recorded (typ: 15 minutes)        |
| <b>Extrusion Temperature (when applicable)</b>   | Characteristic: Recorded (typ: 170 C)             |
| <b>Mixing Temperature</b>                        | Characteristic: Recorded (typ: 100 C)             |
| <b>Electric Field Length</b>                     | Static: Set screw between operations (typ: 20 cm) |
| <b>Field Vertical Alignment</b>                  | Static: Set screw between operations (typ: 0 cm)  |
| <b>Field Horizontal Alignment</b>                | Static: Set screw between operations (typ: 0 cm)  |
| <b>Twin Injection Spacing</b>                    | Static: Set screw between operations (typ: 4 cm)  |
| <b>Faraday Cage Placement</b>                    | Static: Adjusted between operations               |
| <b>Collector Plate Voltage</b>                   | Dynamic: Computer Control (typ: 10kV)             |
| <b>Injection Needle Voltage</b>                  | Dynamic: Computer Control (typ: -10kV)            |
| <b>Flow Rate (Both Needles Independent)</b>      | Dynamic: Computer Control (typ: 0.05 ml/min)      |
| <b>Run Time</b>                                  | Dynamic: Computer Controlled (typ: 15 minutes)    |

### 3.1.1 Materials and Nanotube Dispersion

The materials used for the model nanocomposite system were PVDF (Kynar 761, Arkema) as the matrix and multi-walled carbon nanotubes (CM-95, Hanwha Nanotech) as the reinforcement. Fluorescein (ACROS Organics) was added to select PVDF solutions as both a visible (yellow) and fluorescent marker (494nm wavelength) for characterizing film morphology. N,N-Dimethylformamide (DMF, Fischer Chemical 99.9% purity) was used as a solvent for the dissolution of the PVDF and dispersion of both the nanotubes and fluorescein.

Both the fluorescein and nanotubes were dispersed using the same technique. First, the PVDF was metered and mixed with the DMF in a sealable glass container.

The solution was then placed on a hot plate at 100°C and mixed until homogeneous. The ratio of solutes to solvent in the solution dictates the viscosity of the fluid being electrospun. Therefore, the amount of DMF can be used to directly control the viscosity of the fluid. At the same time, the amount of carbon nanotubes in the solution directly affects the electrical properties of the fluid, which changes how the fluid interacts with the potential field.

Key to proper nano and microstructuring of the polymer is the homogenization of the particulate dispersions. In order to disperse the carbon nanotubes in the PVDF the PVDF and nanotubes are mixed in a hermetically sealed container in a solution of DMF. The solvent is then oven evaporated to leave bulk PVDF which contains highly agglomerated nanotubes. This material is fed through a twin screw extruder, and the high shear rates cause the nanotubes to disperse and align [59]. The resulting polymer is pelletized and dissolved in DMF once more to achieve the proper viscosity. For electrospinning nanofibers the DMF solutions are drawn into a syringe and placed in the syringe pump. The electrical field is then activated and the fluid is pumped through the syringes. Both the potential field and flow rates can be adjusted in order to improve the ability to spin high quality fibers – these have a significant impact on fiber morphology.

### **3.1.2 Fiber Measurement Methodology**

In order to analyze the fiber morphologies SEM images were processed with ImageJ® image processing software. The software allows you to set the scale and make digital measurements on each image. Here 200 measurements were taken of various fibers on each image. Figure 3.2 shows an example of a diameter distribution plot used in order to statistically measure mean and standard deviation. This was done

by using the MATLAB normfit function and evaluating the mean within 95% confidence bounds.

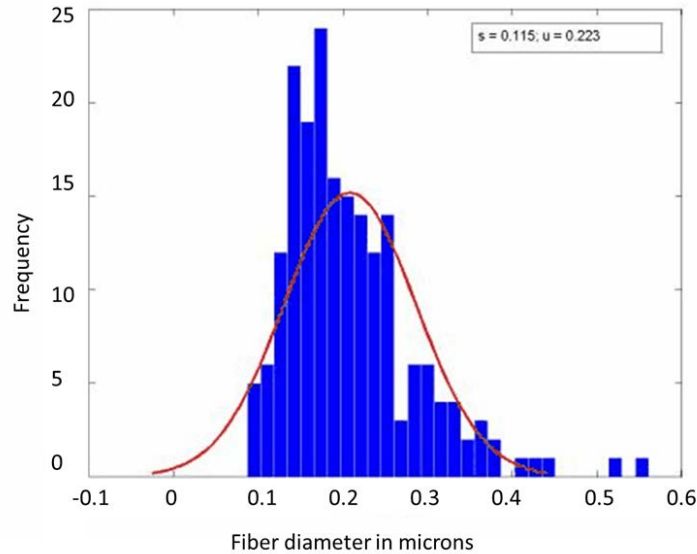


Figure 3.2 Example of diameter distribution used to visualize fiber diameter in electrospun fiber mats

## 3.2 Mark II Results and Discussion

### 3.2.1 Faraday Tube Effectiveness

As the fluid is being spun it experiences a force because it is carrying charge and moving through an electric field. In a laboratory environment large amounts of electrical noise can be generated by nearby equipment. Geometries in grounded surfaces can also greatly affect the shape of the electric field. These factors cause the field to be inconsistent, which are further magnified due to the chaotic nature of the process resulting in a much larger effect on the morphology of the produced

composite. In order to mitigate this problem a Faraday cage (in tubular form) was built to surround the electrospinning apparatus. This provides a consistent ground reference plane and ensures consistency from sample to sample. The Faraday tube also allows for greater control of the electric field by varying the voltages of the collector plate and injection needles separately. The injection needles are electrified with a positive polarity while the collector plate is electrified with a negative polarity. The voltage disparity is the ratio of the absolute value of each voltage with respect to the ground.

During multi jet electrospinning another problem is jet divergence – each jet of fluid is similarly charged, and as such they repel each other. The Faraday cage provides a voltage reference plane and can be used to mitigate the effect of jet divergence through careful control of the ground plane. In order to illustrate this phenomenon a COMSOL™ simulation was used to calculate the potential field within the chamber. Figure 3.3 shows how the electric field changes through alteration of the voltages on the cage, collector plate, and injection needles. As the disparity is changed the ground plane moves in the field direction and suggests focusing-like behavior.

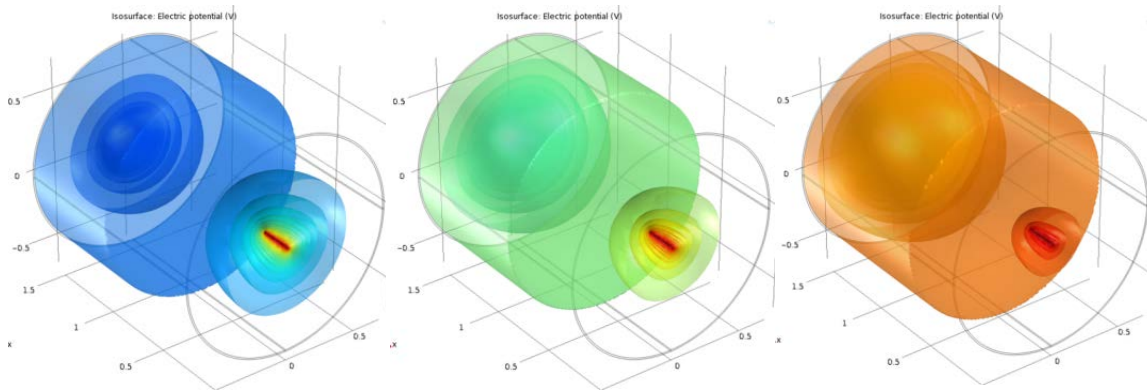


Figure 3.3 Simulation results of electric field within the Faraday tube. The results go from a voltage bias on the injection needle (on the left) to neutral (middle) and voltage bias on the collector (right). The results show that the ground plane is shifted back and forth towards the side with the lower voltage. The field shape suggests focusing mechanisms may be possible.

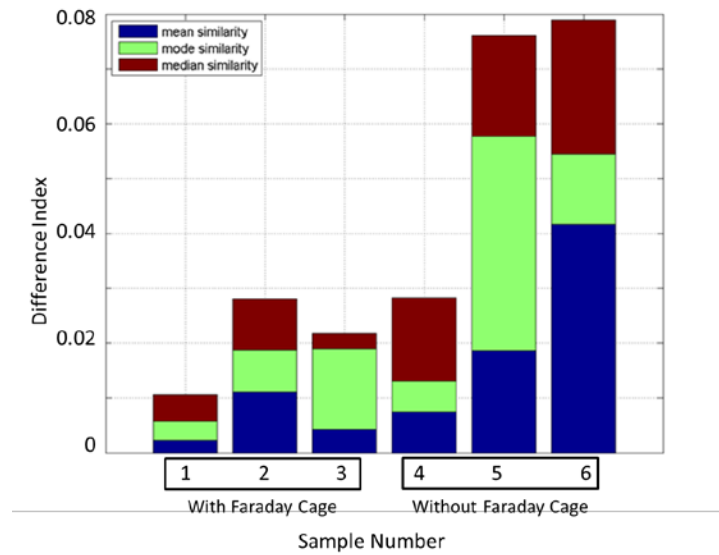


Figure 3.4 The difference index of the films with (first three) and without (last three) the Faraday tube. The results show a good improvement with implementation of the tube.



The implementation of the Faraday tube was tested in contrast to an empty fume hood – which represents the best “typical” environment for electrospinning tests. The fume hood has three grounded walls and an opening to the environment which acts as a zero flux boundary condition. The results were then characterized by a “difference index” which represents a combination of mean, mode, and median standard deviations of fiber diameter, shown in Figure 3.4). The result was a significant improvement in test to test consistency across various voltage disparities. The data are taken from 18 samples, 9 with the Faraday tube, and 9 without. There are 3 different voltage disparities. Fiber diameter data were collected using ImageJ, with 200 samples per image; the outliers were removed using statistical analysis. In addition the Faraday tube tends to reduce the divergence angle of the jets.

### **3.2.2 Macro-scale Morphology**

The macro-scale film morphology is largely dictated by the twin injection co-electrospinning process. Through the use of fluorescein, which acts as a pigment additive, the spinning overlap can be observed. Figure 3.5 shows the various levels of overlap attained through changing injection needle spacing and electrical field shape. In Figure 3.5a a single phase film is produced, in Figure 3.5b two phases are present but not co-mingled, and after focusing Figure 3.5c shows co-mingled phases. The level of control allows for prescribed gradient properties through the thickness and length of the processed film.

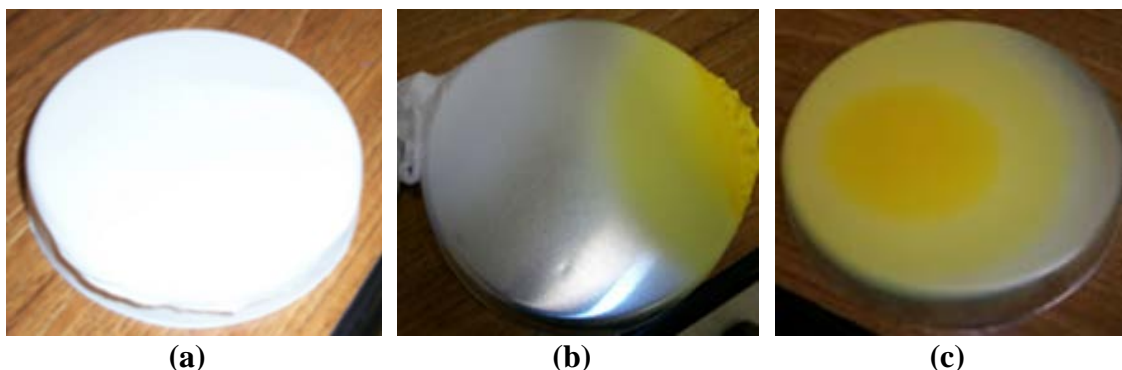
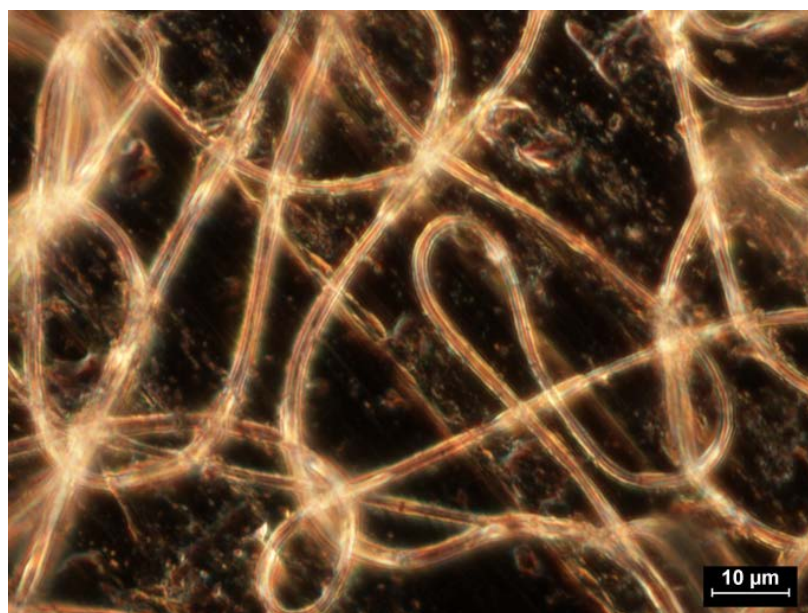


Figure 3.5 Photographs showing macro film morphological changes due to Faraday focusing: (a) Single phase film (b) dual phase, unfocused, (c) single phase, focused

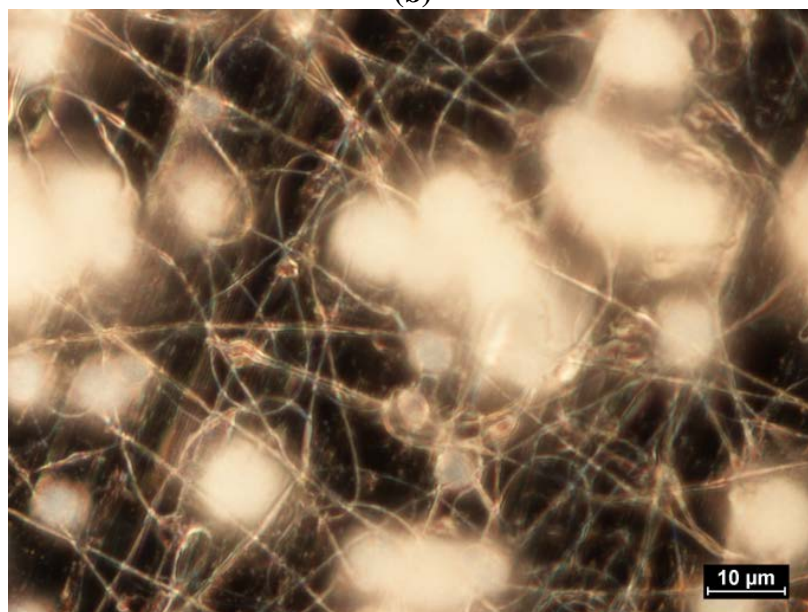
### 3.2.3 Micro-scale Morphology

The micro-scale morphology consists of the fibers generated through the electrospinning process. There are multiple forms of fiber morphology that can be generated through the electrospinning process; for single-phase fibers the two main types of generated morphologies are beaded and non-beaded. These morphologies change with increase in viscosity- with increasing viscosity the process transitions from spraying to spinning, the intermediate being beaded fibers. Figure 3.6 shows the two most typical microstructures. Figure 3.6a (Sample A) was a 20 wt% PVDF in DMF solution with no voltage disparity, while Figure 3.6b (Sample B) was a 25 wt% solution of PVDF in DMF with a voltage disparity of 15/17. These fibers can also be characterized statistically on the basis of individual fibers. Through altering the processing conditions both the average diameter and standard deviation of the diameter can be controlled. Figure 3.7a shows a histogram generated through analysis of the diameters of Sample A while Figure 3.7b represents Sample B. Sample A has an

average fiber diameter of  $0.412\ \mu\text{m}$  and a standard deviation of  $0.109\ \mu\text{m}$  while Sample B has an average fiber diameter of  $1.18\ \mu\text{m}$  and standard deviation of  $0.324\ \mu\text{m}$ .



(b)



(a)

Figure 3.6 Two main classes of micro-scale morphology: (a) with beads and (b) without beads.

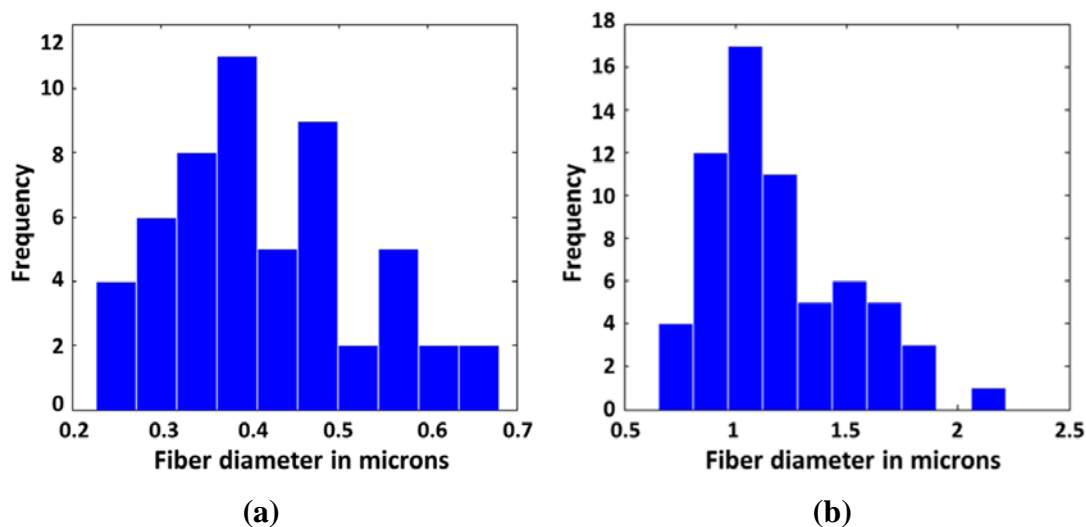


Figure 3.7 Histograms of fiber diameter. (a) Diameter distribution of sample A and (b) diameter distribution of sample B.

To examine the micro-scale co-mingling of the fibers in the twin injection co-electrospinning process fluorescein was dispersed into a single phase of the co-mingled microstructure but was imaged using a fluorescence confocal microscope. Figure 3.8 shows selective images of both phases. Figure 3.8a only shows the first phase while Figure 3.8b both phases without the marker. Figure 3.8c is a composite of the two phases and shows the efficient co-mingling of the two fibers.

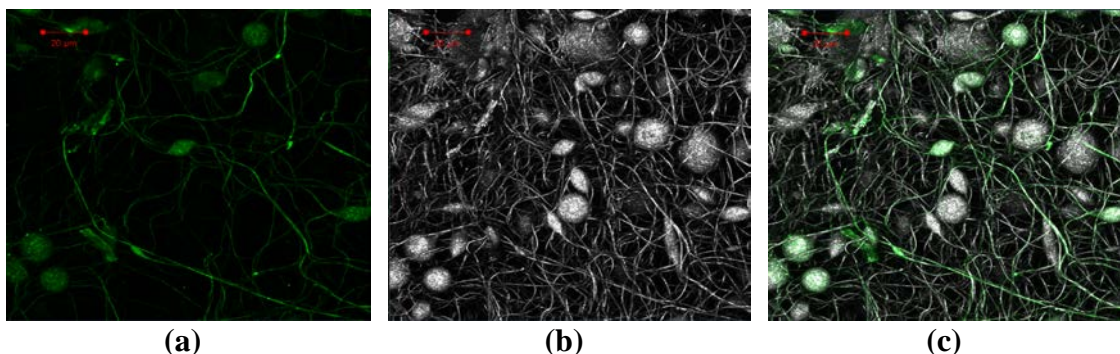


Figure 3.8 Fluorescent confocal microscopy of multi-phase twin injection co-electrospun fibers (a) fluorescent phase only (b) both phases, no fluorescence, (c) both phases with markers (NOTE: Figures b and c appear identical in black and white. See electronic copy for color).

### 3.2.4 Mark II Conclusions

These results demonstrate several techniques which allow for successful control in yielding consistent results. Faraday focusing using voltage disparity allow for microstructural changes and co-mingling of fibers to be customized while allowing for an effect on both the mean diameter and standard deviation. Likewise, solution viscosity control is a key parameter in achieving various microstructures, in this case differentiating between beaded and non-beaded, across different polymer solutions. Twin injection co-electrospinning, in combination with focusing techniques described above allow for horizontal and through-thickness gradient changes in microstructure in multiple dimensions due to computer control .Of fundamental importance in informing the design of the Mark III system, it was also noticed that environmental effects, most notably humidity, play a very important role in the evaporation of the solvent, and thus the parameters used when electrospinning.

### 3.3 Electrospinning with the Mark III system

Motivated by lessons learned from results of the Mark II system, the Mark III variant was constructed in order to have the greatest possible flexibility for current and future work. The largest improvement was the addition of an environmental control and conditioning system. This allowed for the control of humidity, temperature and air flow rate, as well as constant highly accurate measurement of these variables on the exhaust side. Figure 3.9 shows a schematic representation of the engineering controls used for environmental control. Note that temperature control was primarily added for future research potential and was not used in the current study.



Figure 3.9 Schematic description of environmental process controls in Mark III system.

The gantry system used for controlling the position of the injection needles was greatly enhanced, giving each injection point full articulation giving further capability for use with multi-jet electrospinning. In the Mark III system each injection needle is electrified with a different power supply – with three separate power supplies sharing a common ground a large amount of control can be achieved over the potential

field within the chamber. Because of the isolated nature of the environmental chamber the Faraday tube was reduced to a Faraday ring which was placed in between the injection needles and the collector plate and mounted on its own gantry system in order to assert further control over the ground plane tuning mechanism.

### **3.3.1 Materials and Processing**

Two forms of PVDF are used: for all solution cast, electrospun and injection molded samples high molecular weight Kynar 761 was used, and to verify these results, a second baseline film (Kynar/Solef comparable, McMaster-Carr supply, denoted PVDF-EXT) extruded from melt was used as purchased. The melt-process baseline was tested directly in as-received form and compared with literature. For both electrospinning and solution casting the PVDF was dissolved in a solvent containing Dimethylformamide (DMF), or a mixture of DMF and N-methylpyrrolidone (NMP). Both the DMF and NMP were obtained from Sigma Aldrich; the DMF with a purity of 99.9% and the NMP with a purity of 99.0%. The PVDF was dissolved in the solvent at temperatures of 100°C in a hermetically sealed glass bottle with a plastic snap-lid on a hot plate with a magnetic stir bar used to agitate the solvent.

Table 3.2 summarizes the different processing conditions for the composites. Solutions were kept at temperature, mixed until homogenous, and stored at temperature until shortly before electrospinning or solution casting. For the injection molded samples, the polymer was melted using a micro-scale twin screw extruder (DSM MICRO15) at 300°C for 5 minutes and then fed into a micro-scale injection molding machine (DSM X-plore). Upon injection into the mold, the PVDF is quickly cooled to room temperature. Samples were cut from the edge of the molded sample.

Table 3.2 Processing conditions for solutions.

| <b>Sample name(s)</b> | <b>Solvent</b> | <b>Process Type</b>      | <b>PVDF (wt. %)</b> | <b>CARBON NANOTUBE (wt. %)</b> |
|-----------------------|----------------|--------------------------|---------------------|--------------------------------|
| <b>SC-DMF</b>         | DMF            | Solution Cast            | 20                  | None                           |
| <b>SC-DMF-NMP</b>     | 2:1 NMP:DMF    | Solution Cast            | 20                  | None                           |
| <b>ES-10</b>          | DMF            | Electrospun              | 10                  | None                           |
| <b>ES-15</b>          | DMF            | Electrospun              | 15                  | None                           |
| <b>ES-20</b>          | DMF            | Electrospun              | 20                  | None                           |
| <b>ES-20-CNT0.1</b>   | DMF            | Electrospun              | 20                  | 0.1%                           |
| <b>ES-20-CNT0.25</b>  | DMF            | Electrospun              | 20                  | 0.25%                          |
| <b>ESHV-20</b>        | DMF            | High Voltage Electrospun | 20                  | None                           |
| <b>ES-DMF-NMP</b>     | 2:1 NMP:DMF    | Electrospun              | 20                  | None                           |
| <b>PVDF-INJ</b>       | None           | Injection Molded         | 100%                | None                           |

Solution cast specimens (denoted SC) were manufactured by deposition of the solution onto a glass substrate and the solvent evaporated by natural convection in a fume hood with an average face velocity of 170 ft/min and an internal air velocity reproducibly between 80 and 120 ft/min. Electrospun specimens were prepared in a custom built computer automated environmentally controlled electrospinning system (ES-30 high voltage power supplies – Gamma High Voltage Research, NE-1000 syringe pumps - New Era Pump Systems). Temperature and humidity were monitored and the air intake to the environmental chamber was both regulated and desiccated. A Labview program was used to control all subsystems. For all specimens electrospun using pure DMF as the solvent, the humidity was kept under 5% relative humidity whereas the 2:1 NMP:DMF were spun at 60% relative humidity. For all specimens, the temperature was kept to 25°C with a solution flow rate of 0.03 ml/min through a 24 gauge needle. Injector and collector voltages were kept to 13kV and -13kV for



most electrospun samples (denoted ES), and 24kV and -24kV for the high voltage electrospun samples (ESHV-20).

For the inclusion of carbon nanotubes (samples ES-20-CNT0.1 and ES-20-CNT0.25) in the electrospinning process, the nanotubes are first mixed with the Kynar 761 in a 20% PVDF in DMF solution until homogenized. Next, they are solution cast and pelletized. After solution casting, they are fed back through a twin-screw extruder<sup>35</sup> for 15 minutes at 80RPM and 300°C in order to break-up carbon nanotube agglomerates and achieve a good dispersion. The resulting extrusion is pelletized and used in exactly the same way as the Kynar powder in the standard electrospinning solution preparation process.

The porous nature of electrospun PVDF films makes it difficult to utilize them as sensors or actuators since the films are difficult to pole due to the dielectric breakdown in the porous pockets (air). The application of flexible electrodes on the film from a solvent based process is similarly difficult due to the rough surface morphology and the capillary effect, which pulls the solvent through the film and spreads the conductive material through the thickness.

### **3.3.2 Microscopy and Structure Characterization**

In order to fully characterize the structure of the electrospun PVDF an array of analyses techniques are used. Wide angle X-ray scattering (WAXS) and Fourier transform infrared microscopy (FTIR) are used to gather insight on the polymorphic nature of the material, differential scanning calorimetry (DSC) is used to interrogate the crystallinity, and scanning electron microscopy (SEM) is used to characterize the as-spun structure.

### 3.3.2.1 Wide Angle X-Ray Scattering (WAXS)

The specimens were characterized using wide angle x-ray scattering to determine the crystal phase structures present in the material. An x-ray diffractometer (Bruker DAVINCI II) equipped with a 2-D detector (VANTEC 500) was used to investigate the crystal structures. The x-ray source was operated at 40 kV and 35 $\mu$ A achieving a  $\lambda_1$  of 1.54060 Å and a  $\lambda_2$  of 1.54439 Å. The detector was placed at an angle of 25° with an angle of incidence of 0° at a working distance of 200 mm. This field of view was widened for select samples in order to confirm presence of the  $\beta$ -phase, which can be further differentiated from other polymorphs at higher angles. Scans were taken in transmission mode at standard temperature and pressure and run for 1 hour.

Scattering patterns were analyzed using Bruker® total pattern analysis (TOPAS®) profiling software. The background was fitted using an 8<sup>th</sup> order chebychev polynomial fit and the fundamental parameters (FP) approach was used to identify differences in crystal structure. The FP method is constructed using functions that can represent aberration functions inherent to the diffractometer as well as specimen contributions. Error due to sample thickness is calculated and quantified geometrically [60]. Typical sample thickness is approximately 2 mm with the exception of the melt extruded thin film, which is 0.3mm. For thicker samples, Bragg angle shift can be up to -0.25° (measured angle is lower than predicted value).

Using the peak fitting analysis, it was possible to quantitatively compare the  $\beta$  content for each processed film; this was done by adding the area under the curves of all the unique fitted  $\beta$  peaks and dividing by all the non-shared peaks (the peaks at 18.4° and 38.8°). The resulting value is a quantitatively valid representation of the total  $\beta$  content in each sample.

### **3.3.2.2 Fourier Transform Infrared Spectroscopy (FTIR)**

Fourier transform infrared spectroscopy (FTIR) uses the infrared spectrum scattering properties of a material to measure how well a material absorbs light at different wavelengths. The different phases of PVDF have chemical configurations which are dissimilar enough that FTIR can be used for partial phase identification. With PVDF, FTIR is typically used to identify differences in  $\beta$  phase and  $\gamma$  phase. In the current work this is done using the larger angles in the WAXS measurement, but FTIR is still included in order to have a secondary confirmation of the data which can be more readily referenced in literature [61]. Here all scans reported were run in MIR mode, in reflectance, with a range of 6000-600  $\text{cm}^{-1}$ .

### **3.3.2.3 Scanning Electron Microscopy (SEM)**

Scanning electron microscopy (SEM) is used to image the surface of the samples as well as a cross sectional image after freeze fracture. Images are taken with an Zeiss AURIGA™ 60 Crossbeam™ FIB-SEM using an accelerating voltage of 3kV and sputter coated with 60:40 Au:Pd target for 60s. Images were taken with a SESI (secondary electrons secondary ions) for lower magnifications and an in-lens detector for higher magnifications.

### **3.3.2.4 Differential Scanning Calorimetry (DSC)**

Differential scanning calorimetry with a Mettler-Toledo™ DSC-1 with a heat ramp from 30 to 180 degrees at 5 degrees per minute and integrated to determine onset and peak melting temperatures. A second heating was done on each sample as a post-melt baseline to ensure quality control of DSC results.

### 3.3.3 Mark III Results and Discussion

In order to carry out the analysis, each type of material was studied via x-ray scattering and the scattering pattern analyzed to study the polymorphism of PVDF. The baselines are used to better understand the distinctions between  $\alpha$  and  $\beta$ -phase PVDF which allows for a proper comparative study using peak fitting software. Using DSC to investigate the onset and peaks of melt is another way of gaining insight into the crystal structure of various samples. When multiple polymorphs are present, there are distinct melting peaks for each polymorph. Table 3.3 contains the  $\beta$ -fraction from the peak fitting and the DSC peaks for each sample type and the DSC curves are given in Figure 3.10.

DSC provides a good companion to the crystallography data. It is best to compare the samples that were processed using the same precursor (the Kynar 761); otherwise, differences in polymer chain length will affect the results. The integration and first peak of melting were recorded for all samples. Table 3.3 also contains sample type, integration, and peak of melt for each sample. Generally speaking, samples with higher  $\beta$ -phase content have higher melting points, but it is also affected by thermal history and how perfectly the crystal structures formed are. These two effects can have significant overlap, which is why the technique cannot be used reliably for phase analysis.

Table 3.3 Curve fitted  $\beta$  fraction values as well as DSC melt onset and melt peaks

| Sample Name  | $\beta$ -fraction | Normalized DSC Integral ( $\text{Jg}^{-1}$ ) | DSC 1st Melt Peak $^{\circ}\text{C}$ |
|--------------|-------------------|----------------------------------------------|--------------------------------------|
| PVDF-EXT     | 0.00              | (different precursor)                        | (different precursor)                |
| PVDF-INJ     | 0.00              | $-45.13 \pm 4.70$                            | $167.89 \pm 0.09$                    |
| ES-10        | 0.37              | $-36.72 \pm 1.29$                            | $165.16 \pm 0.07$                    |
| ES-15        | 0.47              | $-42.95 \pm 1.59$                            | $165.64 \pm 0.27$                    |
| ES-20        | 0.48              | $-48.02 \pm 6.37$                            | $165.67 \pm 0.12$                    |
| ESHV-20      | 0.60              | $-46.16 \pm 4.40$                            | $165.25 \pm 0.09$                    |
| ES-20CNT0.1  | 0.42              | $-49.17 \pm 11.36$                           | $166.21 \pm 0.04$                    |
| ES-20CNT0.25 | 0.95              | $-40.99 \pm 0.79$                            | $164.24 \pm 0.17$                    |
| ES-DMF-NMP   | 0.96              | $-45.99 \pm 1.77$                            | $163.87 \pm 0.20$                    |
| SC-DMF       | 1.00              | $-65.41 \pm 3.47$                            | $167.44 \pm 1.26$                    |
| SC-DMF-NMP   | 1.00              | $-57.88 \pm 5.38$                            | $170.17 \pm 0.62$                    |

The DSC results show higher melting points for the electrospun samples, and higher still for the solution cast samples – agreeing well with the scattering results. The DSC integration is used to represent the degree of crystallinity. The electrospun sample with 0.25% carbon nanotubes has a very similar DSC curve to the films solution cast from DMF sample, suggesting it has a similar structure as well as very high  $\beta$ -fraction, however, it has a slightly lower normalized integral than other electrospun samples showing lower crystallinity. This agrees well with past studies but shows that there exists a threshold concentration of nanotubes below which adding carbon nanotubes does not improve the  $\beta$  polymorph content. The primarily  $\alpha$ -phase injection molded sample shows a curve distinctly different from all  $\beta$ -phase containing samples.

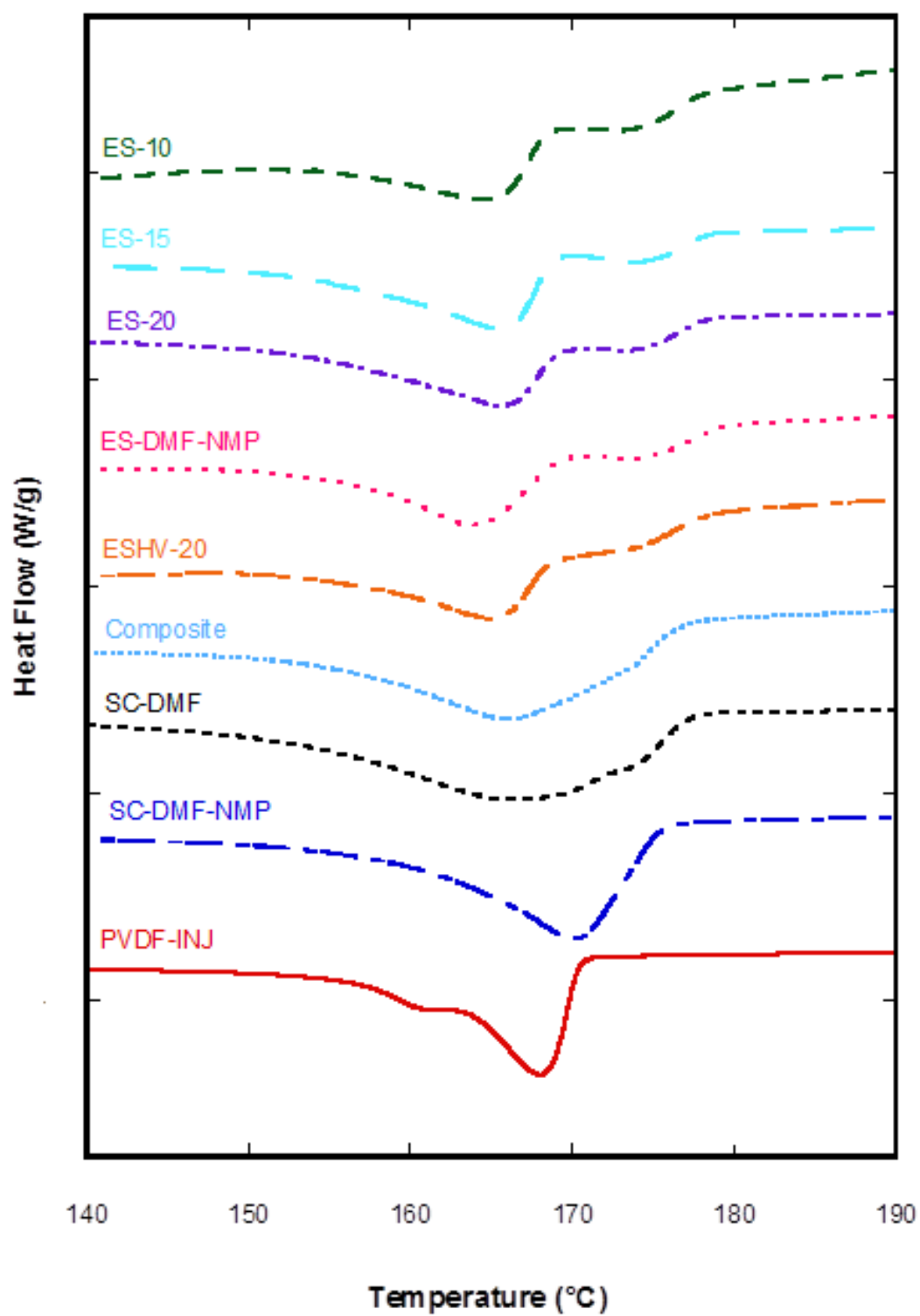


Figure 3.10 DSC thermograms for all specimens.

### 3.3.3.1 Polymorphism in Melt and Solution Processed PVDF

As a baseline (SC-DMF) is solution cast from 20% PVDF in DMF. The WAXS scan is taken at a larger angle to have a confident full characterization of a primarily  $\beta$ -phase sample. The peak at  $26^\circ$  is a strong reflection based for both  $\alpha$  and  $\gamma$ -phases while the peak at  $57^\circ$  is nonexistent in the  $\gamma$ -phase, confirming that the phase does not exist in our samples. Figure 3.11a shows its SEM micrograph, while Figure 3.12a shows its scattering pattern. The primary peak at  $20.18^\circ$  correlates with the  $20.26^\circ$  peak reported in literature when incorporating left-biased thickness shift due to transmission and the  $36^\circ$  peak is also present. The micrograph shows formation of well-formed  $\beta$ -phase crystal spherulites [23] in the range of 2-3  $\mu\text{m}$  in diameter.

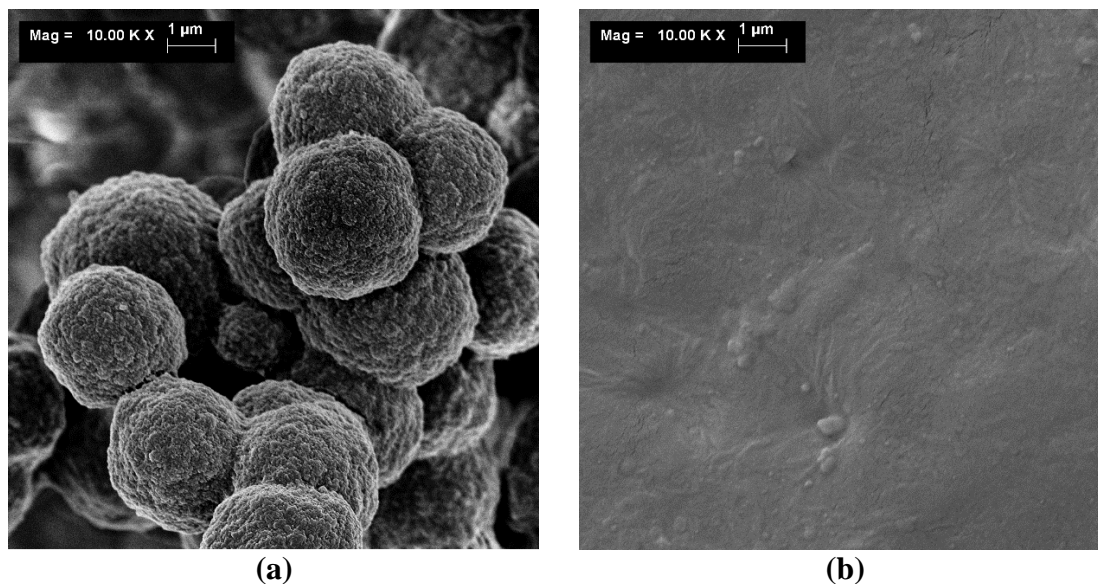


Figure 3.11 SEM micrographs showing (a) spherical structures representing  $\beta$  spherulites in the film solution cast from DMF and (b) radial lamellae formation in  $\alpha$ -phase film.

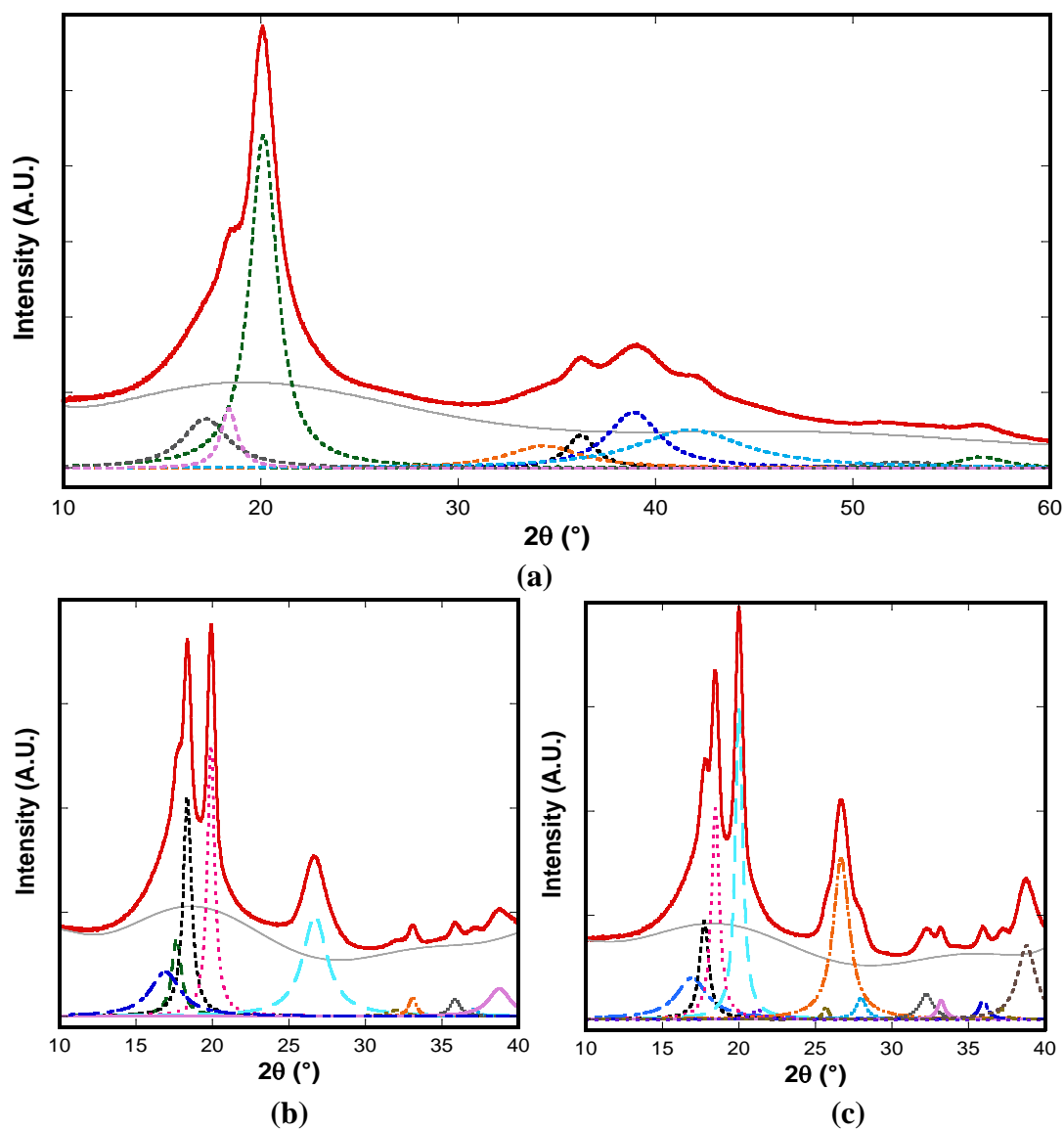


Figure 3.12 (a) Full range scattering pattern of 20% PVDF cast from pure DMF demonstrating pure  $\beta$  crystal structure. (b) Scattering pattern of PVDF injection molded PVDF showing pure  $\alpha$  crystal structure. (c) Scattering pattern of PVDF extruded from melt demonstrating pure  $\alpha$  crystal structure.



PVDF-EXT is the film extruded from melt. It can be seen from Figure 3.11b that radial lamellae are formed, which have been shown to be indicative of  $\alpha$ -phase crystal structure. Figure 3.12b shows predictably yielding strong peaks for  $\alpha$ -phase PVDF at  $16.7^\circ$ ,  $17.7^\circ$ ,  $19.9^\circ$ ,  $26^\circ$ , and  $38^\circ$  from the injection molding of Kynar761. Because the film is non-porous and very consistent, the peaks have very little variability in position. Figure 3.12c shows that the extruded film has a comparable  $\alpha$ -phase scattering pattern demonstrating consistency between various processing techniques in producing pure  $\alpha$ -phase PVDF.

### **3.3.3.2 Influence of electrospinning variables on polymorphism of PVDF**

Electrospinning from DMF was shown to produce the highest quality electrospun thin films with a very evenly spun distribution of smooth fibers. The scattering results (Figure 3.13) indicate mixed phases of crystal structure between the  $\alpha$  and  $\beta$ -phase. Samples ES-10, ES-15, and ES-20 were electrospun by varying the electrospinning solution concentration from 10 wt% to 20wt%. The increase in PVDF concentration has only a small effect on the  $\beta$ -fraction with values of 0.37, 0.47, and 0.48 respectively.

During electrospinning, the viscoelastic stream undergoes a very complicated solvent evaporation process. The polymerization mechanics are a balance between thermal stability and polymer kinematics – the  $\alpha$ -phase is kinematically more favorable and the  $\beta$ -phase is thermodynamically more favorable. Thus, the polymorph formed is largely dependent on evaporation rate [23] and its relation to surface area and volume. During electrospinning the evaporation rate and surface area to volume ratio are constantly changing, which is why a mixture of both phases is expected.

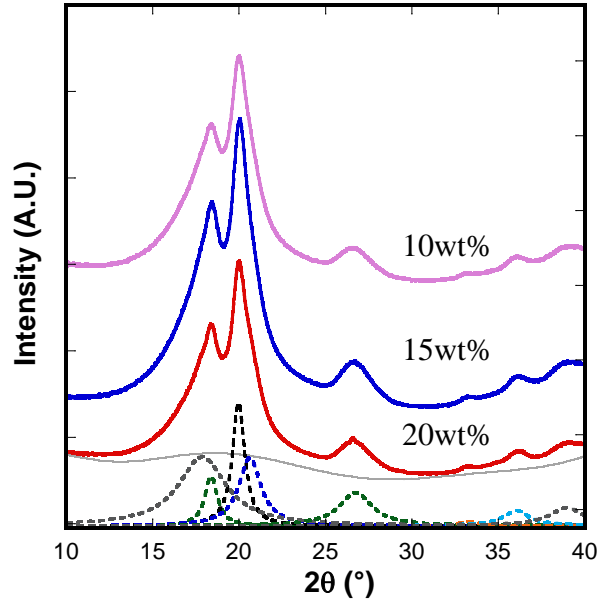


Figure 3.13 (a) Scattering patterns of PVDF electrospun from 10%, 15% and 20%.

As a test-case, sample ES-20-CNT0.1 was electrospun with a low percentage of carbon nanotubes (0.1%); Figure 3.14a shows that the inclusion still resulted in a mix of  $\alpha$  and  $\beta$  phase when spun from a 20% PVDF in DMF solution. The resulting  $\beta$ -fraction was 0.42 and is a negligible difference from other electrospun samples. While macroscopically, the electrospun films with nanotubes have a gray color, under SEM, they are visually identical to neat electrospun films, implying that the nanotubes are well dispersed within the fibers. When the concentration of nanotubes is increased to 0.25%, the dispersion quality is maintained, but the crystal structure becomes predominantly  $\beta$ -phase with a  $\beta$ -fraction of 0.95, as shown in 3.14b. The existence of high  $\beta$ -phase content suggests that there is a critical threshold of carbon nanotube addition which results in the promotion of  $\beta$  polymorph crystal growth.

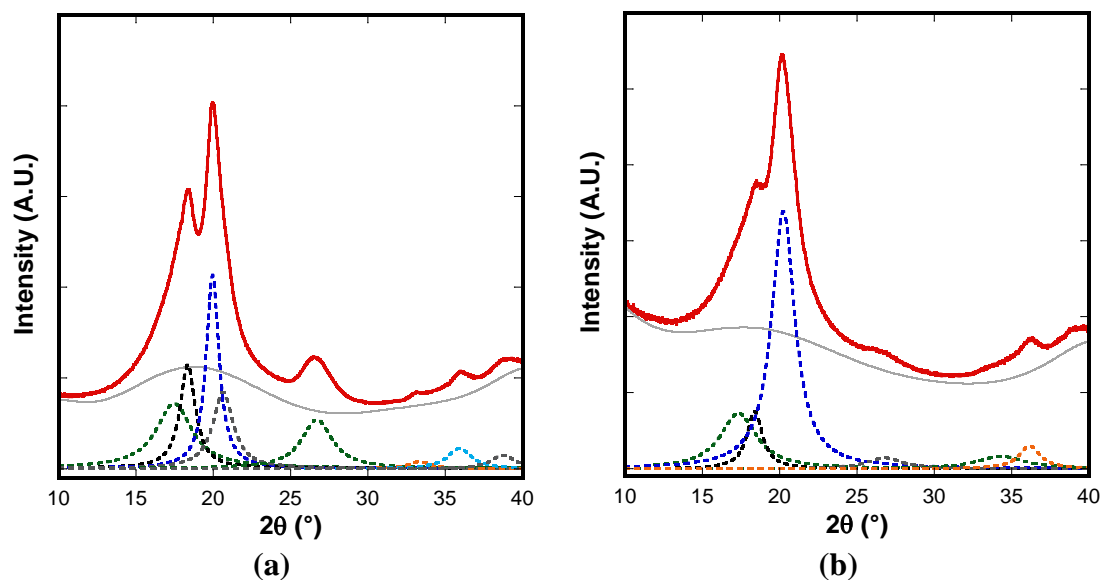


Figure 3.14 (a) Scattering patterns for fibers electrospun from 15wt% PVDF in DMF with 0.1% carbon nanotubes included in the PVDF and (b) electrospun from 20wt% PVDF in DMF with 0.25% carbon nanotubes showing that a larger concentration of nanotubes has a drastic effect on  $\beta$ -phase content.

A solution cast (SC-DMF-NMP) and electrospun sample (ES-DMF-NMP) were both produced from a 2:1 NMP:DMF mix for comparison (see Figure 3.15). This is of interest because the NMP tends to slow the evaporation rate. The solution cast resulted in pure  $\beta$ -phase formation, identical to the DMF solution cast baseline. The electrospun sample had a  $\beta$ -ratio of 0.96 and a  $2\theta$  angle of 20.76 for primary  $\beta$  peak, showing a much higher content of the  $\beta$  phase, as well as a higher degree of polarization. The primary challenge is that electrospinning from this mixture produces a much less consistent film topology, which is difficult to post-process.

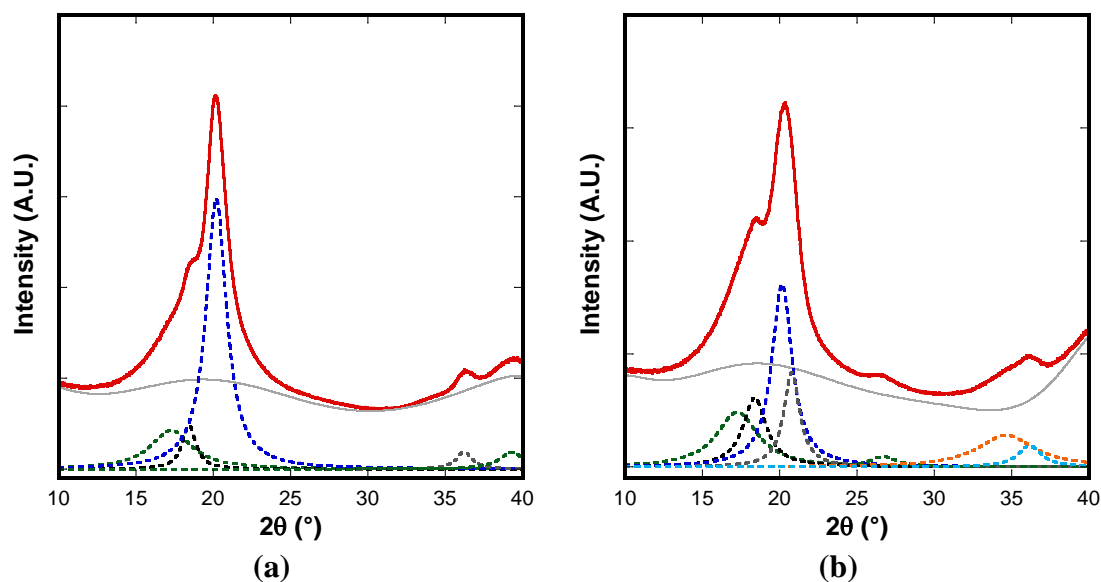


Figure 3.15 (a) Scattering patterns of PVDF solution cast from 2:1 NMP:DMF mix (solcast-mix) and (b) PVDF electrospun from the same solution.

### 3.3.3.3 Verification of Results by FTIR

Because it is useful for comparison to other similar studies FTIR scans were collected in order to confirm that the  $\beta$  phase is being properly observed versus the  $\gamma$  phase. Characteristic of the  $\beta$  phase are bands at  $840\text{cm}^{-1}$  and  $1279\text{cm}^{-1}$  as shown in Figure 3.16. This is consistent for all three electrospun samples, as well as the cast sample which was verified to be  $\beta$  phase by examination of the  $57^\circ$  angle in Figure 3.12.

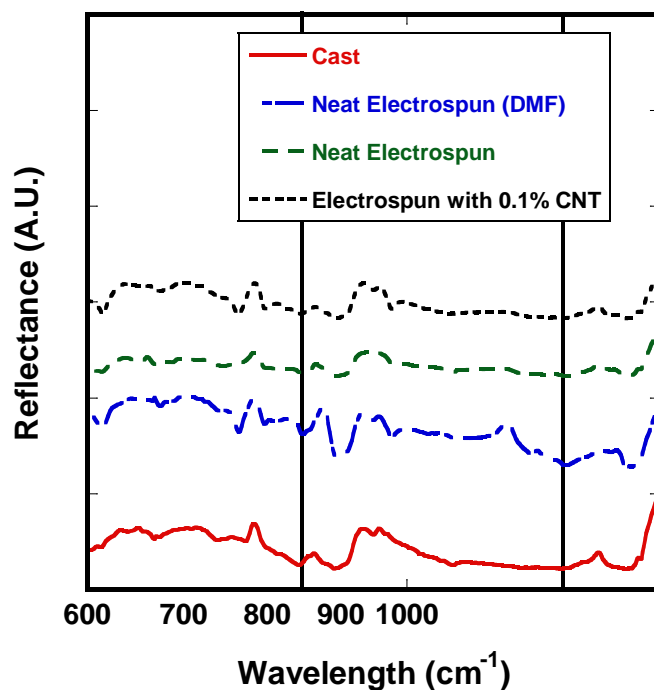


Figure 3.16 FTIR results confirming  $\beta$  phase PVDF with absorption peaks at  $840\text{cm}^{-1}$  and  $1279\text{cm}^{-1}$

### 3.4 Conclusions

In order to achieve the goal outlined in Chapter 2 of achieving sub percolation threshold high carbon nanotube content PVDF composite electrospinning is studied as a candidate manufacturing technique. The important characteristics are the ability to consistently spin carbon nanotube containing PVDF fibers with tight process control, and to ensure that the as processed PVDF had a crystal structure comprising of primarily  $\beta$  phase. The polymorph of PVDF with the strongest piezoelectric properties. This study was done across two generations of manufacturing apparatuses. First, the Mark II system addressed the challenge of producing very consistent high quality PVDF films by using engineering controls to eliminate or control all key process variables. Secondly the Mark III system, making improvements informed

from the Mark II system, was used to produce high quality carbon nanotube containing PVDF fiber mats. These mats were then tested to assess their candidacy as a suitable material for improvements in the piezoelectric effect.

The engineering controls used by the Mark II system consisted of computer controlled flow rates and voltage sources, monitored environmental conditions, and a Faraday cage which was used to reduce environmental noise and provide additional control of the electric field. These controls were instrumental in showing that a high level of consistency can be achieved with. It also showed that these controls allowed for production of high quality co-mingled fibers from twin-jet electrospinning. The Faraday cage was successfully used to manipulate the electric field. These experiments also showed, through careful monitoring of environmental conditions, that humidity is a very large contributor to variance in electrospun film morphology. This heavily influenced the design of the Mark III system.

The Mark III system improved on the engineering controls by adding temperature, humidity, and air velocity control and measurement and successfully produced consistent electrospun fabrics as predicted from experiments with the Mark II system. The Mark III system showed that the electrospinning of PVDF from DMF reliably produces a co-existence of both  $\alpha$  and  $\beta$ -phase crystallites; electrospinning also has the effect of partially poling the film due to the application of high voltages. Electrospinning from a 2:1 NMP:DMF solution produces much higher content of  $\beta$  crystallites, but is a difficult process to control, which requires more investigation. It was also found that there is a threshold between 0.1wt% and 0.25wt% carbon nanotubes, where the inclusion of the nanomaterial in the electrospun fibers promotes  $\beta$ -phase crystal growth

## **Chapter 4**

### **HIGH VOLTAGE CONSIDERATIONS**

Chapter 2 showed that a high quality dispersion of carbon nanotubes in PVDF is a key requirement in order to produce an improvement in piezoelectric strength and Chapter 3 demonstrated that a high quality distribution of carbon nanotubes is possible with electrospinning. Although this processing technique results in the production of the proper  $\beta$  phase PVDF, in its as-processed state, an electrospun film still cannot be used pragmatically in sensing or actuation applications because it cannot sustain a high voltage electric field. In this chapter the electrical breakdown and tracking behavior for nanocomposites are characterized.

This study uses an innovative test method to analyze the various failure mechanisms in the poling process for solution cast and electrospun films, as well as to propose design guidelines and material changes in order to inhibit failure. Poling system and film geometry design constraints are formulated in order to mitigate failure due to corona discharge and electrical surface tracking. In order to mitigate the effects of dielectric breakdown a material change was made to the electrospun films through a film consolidation technique. The consolidation is done using a novel micro-scale vacuum infusion system which allows for the production of a fully dense non-porous thin film while freezing the micro-structure in place to maintain the quality of the carbon nanotube dispersion.

#### 4.1 High Voltage Electrical Breakdown

A large barrier to the production of films using this method is the ability to electrically pole the material: the process of aligning the dipoles in the crystal phase of the structure in order to impart piezoelectric functionality. There are three ways the

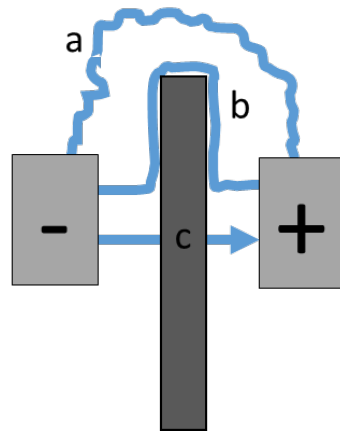


Figure 4.1 Illustration of the three possible ways of failing the poling process: (a) corona discharge occurs when the current passes through ionized air around the sample (b) electrical surface tracking is when the current conducts through the interphase between the sample and the air, and (c) dielectric breakdown is when the polymer itself fails under load and becomes conductive

sample can fail (illustrated in Figure 4.1): Corona discharge (a) is when ionization of the air around the sample is forms a conductive pathway between electrodes, Electrical surface tracking (b) is when the surface properties of the material allow for electrical conduction in the interphase between the material and the air, and dielectric breakdown (c) occurs when the electric field strength exceeds the materials dielectric strength and ionization and conduction occurs through the thickness of the material.



Corona discharge occurs when a fluid (typically air) ionizes between two electrodes due to the presence of high voltage. This creates a region of plasma around the electrodes – when the ionized region grows enough to stretch between anode and cathode a conductive path is formed and an electric arc can be sustained. In regards to poling a PVDF film this occurs when the electrode-to-edge length is smaller than the corona discharge conductive path length [62]. The arc distance is related several factors but has a logarithmic relationship with the electric voltage as described by Peek's law [63].

Electrical surface tracking is due to the formation of a conducting path on the surface of the material. This can be due to a variety of factors and is a rather complex process but the most common are breakdown of the material itself due to high field strengths or surface contaminants [64].

Dielectric breakdown is when an insulating material experiences failure of its insulating properties. When the material is subject to high enough electric field trapped electrons are liberated and a conducting path can be formed between the electrodes [65] – degradation of insulating properties subsequently results in heat generation and mechanical sample degradation. From an electrical standpoint, electrospun fiber mats can be treated as a PVDF-air composite, where the PVDF has a much higher dielectric breakdown strength than the air. In this case, dielectric breakdown is very similar to corona discharge – the air ionizes and forms conductive pathways through the air pockets in the material [52] at a much lower electric field strength because the breakdown strength of air is significantly lower than that of PVDF.

## **4.2 Experimental**

### **4.2.1 Materials**

In order to study these effects PVDF-based thin films were produced by three methods: solution casting, electrospinning, and a composite of the two. All three films types were produced both with and without carbon nanotube reinforcement. These samples were compared to a commercially produced PVDF thin film. The prepared samples were all produced using high molecular weight Kynar 761 PVDF and Dimethylformamide (DMF) purchased from Sigma Aldrich with a purity of 99.9% as the solvent system. Solution cast thin films were prepared by casting from a 20wt% solution of PVDF in DMF on a temperature controlled glass substrate at 40°C in a fume hood for 36 hours.

The electrospun samples were produced from a solution of 20 wt% PVDF. Solutions for all produced films were prepared through dissolution at 100°C in a glass hermetically sealed bottle with a magnetic stirrer on a temperature-controlled hot plate. In order to properly disperse carbon nanotubes they were added to a 20wt% PVDF in DMF solution at a rate of 0.1wt% carbon nanotubes in PVDF. This solution was then cast and pelletized. The carbon nanotube/PVDF pellets were processed with a DSM MICRO15 twin-screw extruder for 15 minutes at 300°C in order to de-agglomerate and obtain a high-quality dispersion and subsequently re-pelletized and processed in the same manner as the neat thin films. A Kynar/Solef comparable thin film was purchased from McMaster-Carr Supply for the commercially produced thin film.

#### **4.2.2 Electrospinning and Composite Processing**

The electrospinning process was conducted in an environmentally controlled chamber set to 25°C and a relative humidity of less than 1%. The injection voltage was set to 13kV at the needle and -13kV at the collector plate with a separation distance of 18cm with a grounded ring suspended at the midpoint in order to stabilize the electric field. The solution is pumped into the chamber at 0.03 ml/min through a 24 gauge steel needle and the air inlet pressure is kept at 550 kPa (80 psi) generating an average velocity of 15 m/s (50 ft/s), the exhaust is vented into a fume hood to prevent the release of DMF fumes.

In order to reduce the porosity of the thin films while maintaining the dispersive properties of the electrospinning process a novel composite processing technique was used to combine the properties of solution casting and electrospinning. A 20 wt% solution of PVDF in DMF was solution cast onto an electrospun sample and placed between an aluminum substrate and an aluminum caul plate. Porous media was placed on top and around the sample to allow the air to escape and the system was placed under a vacuum bag. Vacuum was drawn for 48 hours, followed by 24 hours out of vacuum for further drying. Films produced by this method were inspected and shown to be macroscopically homogenous. A more detailed discussion of the manufacturing process is included in Chapter 5.

#### **4.2.3 Electrical Property Characterization**

A system involving floating electrodes was designed and built to characterize different mechanisms of failure under the poling process. In order to electrically pole a PVDF thin film it is important to isolate the film from all other surfaces and the electrodes from each other. Corona discharge is a well-studied phenomenon but is

highly electrode geometry and thus needed to be studied with the same system that would do the poling. It was also very important to be able to characterize the electrical surface tracking properties of each material, as well as the dielectric breakdown, so the system was designed to be capable of running both experiments.

Two opposing electrode rods are suspended across from each other using a structure machined from GPO3 – an arc, track, and flame resistant fiberglass laminate. In order to test dielectric breakdown strength and corona discharge the test-stand is arranged horizontally (see Figure 4.2). For testing dielectric breakdown the sample is sandwiched in between two chamfered electrodes and suspended away from any other surface and the electric voltage is increased until a conducting path is formed through the material. In order to test the effect of corona discharge the sample is removed and the electrode distance adjusted and the voltage is increased until an arc forms.

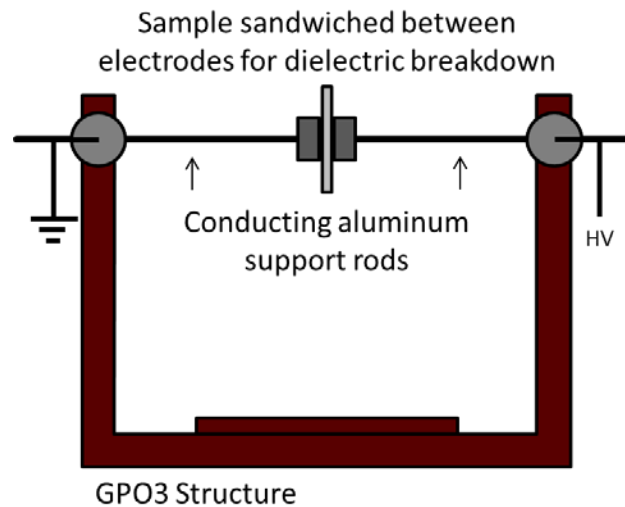


Figure 4.2 For testing of dielectric breakdown strength the electrodes of the custom electrical testing system support the sample horizontally. For corona discharge the sample is removed and the electrodes are tested at differing distances of separation.

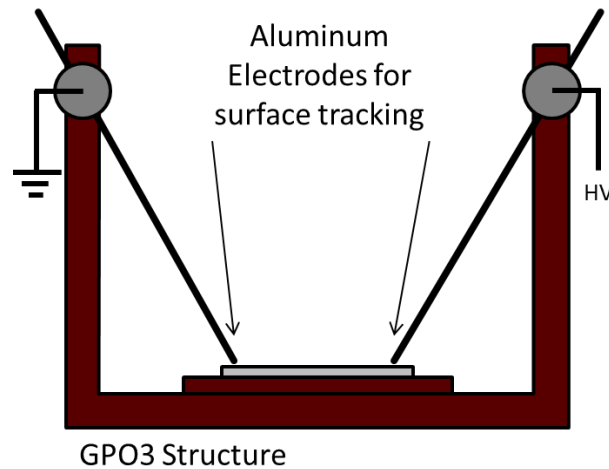


Figure 4.3 For testing of electrical surface tracking initiation voltage the electrodes of the custom electrical testing system support rest on the sample, which is attached to a GPO3 platform. The voltage at which tracking initiates is tested for differing electrode separation distances.

In order to test the electrical surface tracking pointed electrode ends are attached and the rods are lowered to a GPO3 platform which can hold the sample (see Figure 4.3). The electrical surface tracking test is a simplification of the ASTM D3638 test used to measure surface tracking due to surface contamination and degradation, however because this test is used to measure variance due to the surface structure of each thin film the application of contaminants is not required. The electrodes are placed on the surface of the sample with careful measurement of the distance between them and the voltage is increased until tracking is initiated.

For all tests the voltages are supplied and controlled by a high voltage power supply (ES-30 model from Gamma High Voltage) through a LabView software which starts the voltage at 0.5kV and increases by 0.25kV every 3 seconds until either the voltage drops (meaning a partially conductive condition has been reached) or the

current rises above a set tolerance indicating that it is conducting through the sample to signify failure.

#### **4.2.4 Microscopy**

Scanning electron microscopy (SEM) is used to image the surface of the composite sample, as well as a cross sectional image after freeze fracture. Images are taken with a Zeiss AURIGA™ 60 Crossbeam™ FIB-SEM using an accelerating voltage of 3kV with a SESI (secondary electrons secondary ions) detector. Prior to imaging the samples were sputter coated with 60:40 Au:Pd target for 1 minute. A Dino-Lite Pro AM413T USB desktop digital microscope was used to image surface of solution cast films with re-agglomerated carbon nanotubes.

### **4.3 Results and Discussion**

#### **4.3.1 Corona Discharge and Electrical Surface Tracking**

In testing it was observed that two methods of failure under poling – corona discharge and electrical surface tracking – can coexist implying that there is an inflection point between both mechanisms (Figure 4.4), thus by studying each mechanism separately it is possible to produce a design guideline for high voltage poling through the electrode method.

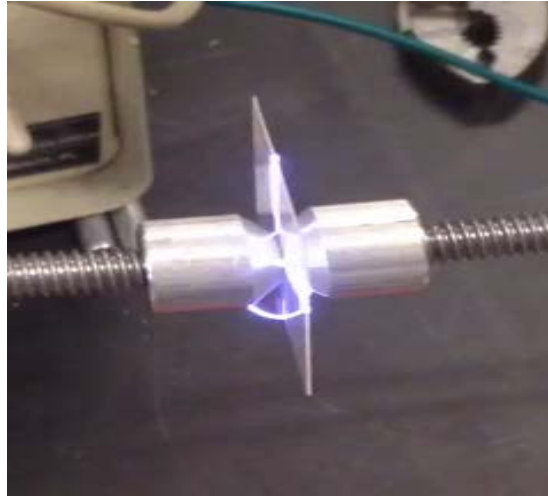


Figure 4.4 Demonstration of the transition point between electrical surface tracking and corona discharge when the sample is cut intentionally short and placed in the sample holder for poling.

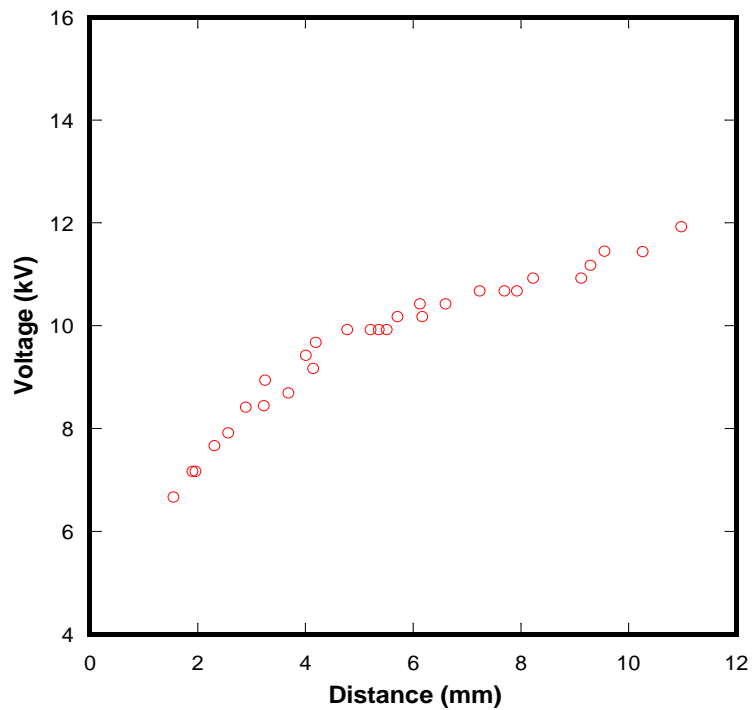


Figure 4.5 Corona discharge behaves in a logarithmic fashion as described by Peak's Law. Experimental testing confirms this and takes into account geometric variables such as electrode type.

Corona discharge is a well-studied effect, however because voltage rate-of-increase and electrode geometry have such a large effect on the initiation electric field strength the test is repeated with the modular HV test stand. Figure 4.5 shows the corona discharge of air using the HV test stand – this is important because corona discharge initiation voltages differ based on materials and geometries used. The data are logarithmic in nature with a slowly increasing voltage with electrode distance, this is well studied and verified by Peek’s law which the electric potential required to trigger corona discharge across a gap between two contacts is shown to be logarithmic with respect to distance between electrodes.

Electrical surface tracking happens on the interphase between the air and the surface of the material. Ionic conductive paths are formed until they fully connect both electrodes, after which the surface of the material carbonizes and sustains conduction. Electrical trees form between both electrodes and move back and forth along the surface generating carbon trails and destroying the sample. Electrical surface tracking initiation voltage was tested on all samples at various distances and is shown in Figure 4.6. It was found that both the solution cast and electrospun films had slightly higher minimum initiation voltages when infused with carbon nanotubes with the solution cast sample having the more dramatic effect.

For the other samples the minimum voltage required to initiate surface tracking was the same for each sample type and linear with respect to tracking distance. This line is calculated as the line which traces the bottom of the point cloud for all samples as  $y = 1.08x + 1.37 \frac{kV}{mm}$ . The amount of variance in the initiation voltage however, is different for each film type. This can be visualized by calculating the root-mean-



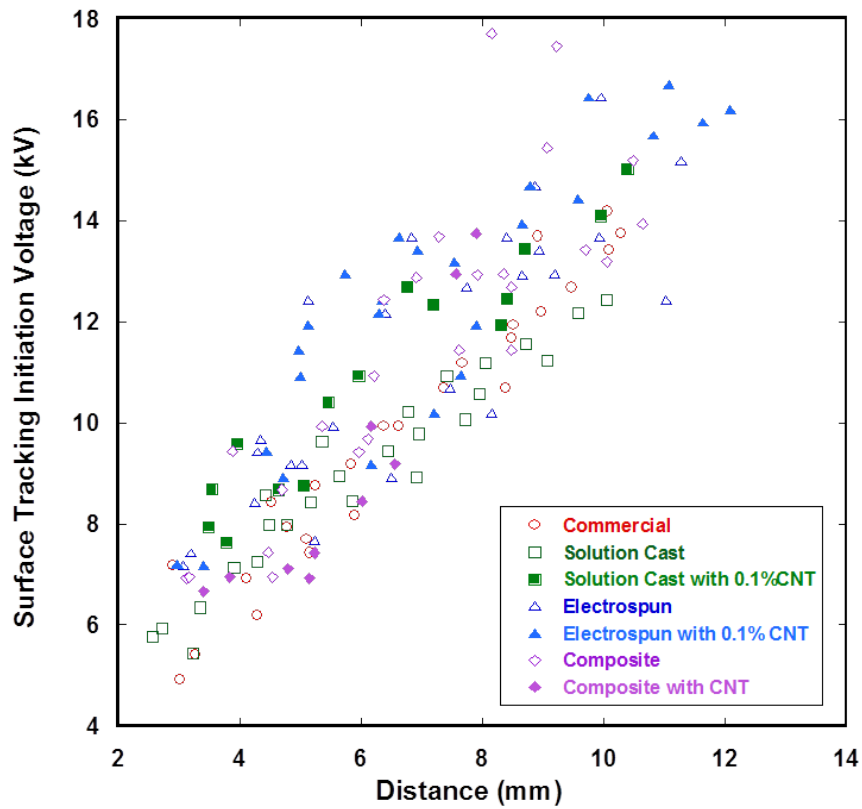


Figure 4.6 Electrical tracking initiation voltage for various distances for all samples. All samples demonstrate having the same minimum initiation voltage relationship with distance with the exception of the solution cast and electrospun samples containing carbon nanotubes. This increase is due to proximity of the carbon nanotubes to the surface of the materials, which is higher for the solution cast and lower for the electrospun films.

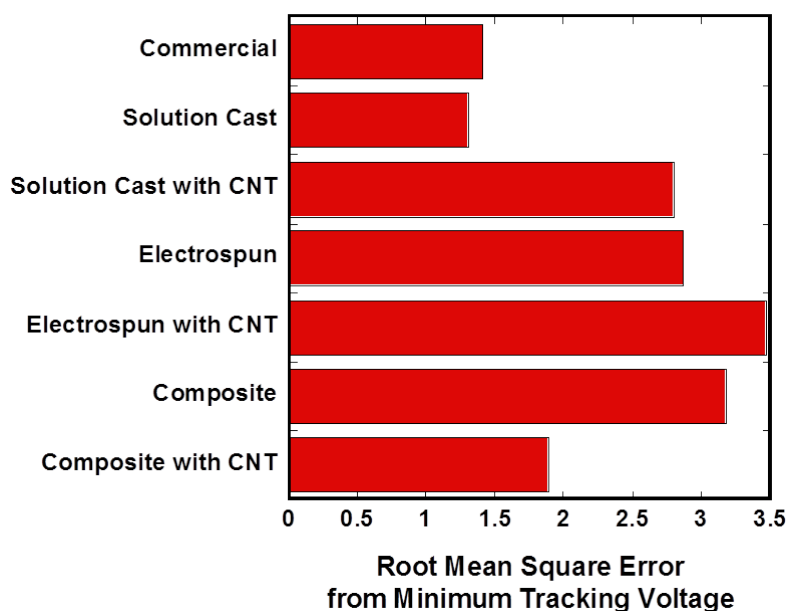


Figure 4.7 Root mean square error between the minimum surface tracking initiation voltage of neat PVDF and all samples – higher values denote higher statistical likelihood of surpassing the surface tracking initiation voltage of the material.

square error (RMSE) between for each sample against the calculated minimum surface tracking voltage, summarized in Figure 4.7. The commercial and solution cast films have the smallest amount of variation while the electrospun and composite films have much more incidence of heightened electrical surface tracking strength. When carbon nanotubes are added to the solution cast film the variance is much higher due to interaction between the carbon nanotubes and the surface of the material. The same effect boosts the variance of the electrospun film when carbon nanotubes are added though the effect is less pronounced due reduced carbon nanotube-surface proximity. Adding carbon nanotubes to the composite sample lowers the variance because the

carbon nanotubes have very little surface contact, and the composite has a higher wettability and thus higher surface quality.

This surface quality is correlated to how often the material is able to have a higher electrical surface tracking initiation voltage than the minimum and is highly dependent on the quality of the surface. The commercially drawn film is very smooth (see Figure 4.8) and homogenous and the solution cast film is slightly cleaner (see Figure 4.9) explaining the slight improvement in RMSE for the solution cast film.

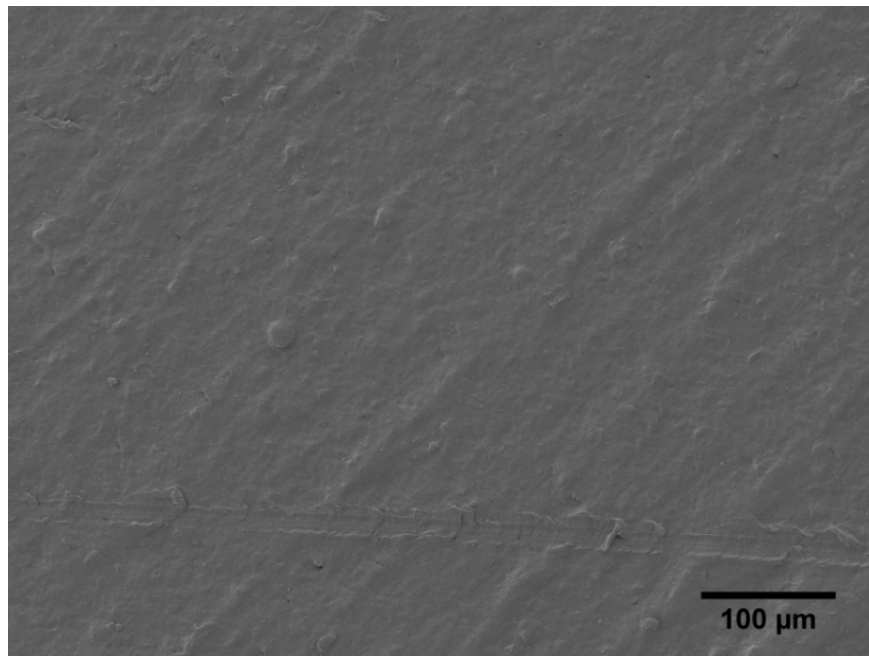


Figure 4.8 SEM micrograph of the surface of commercial PVDF showing a homogenous surface with some roughness from manufacture

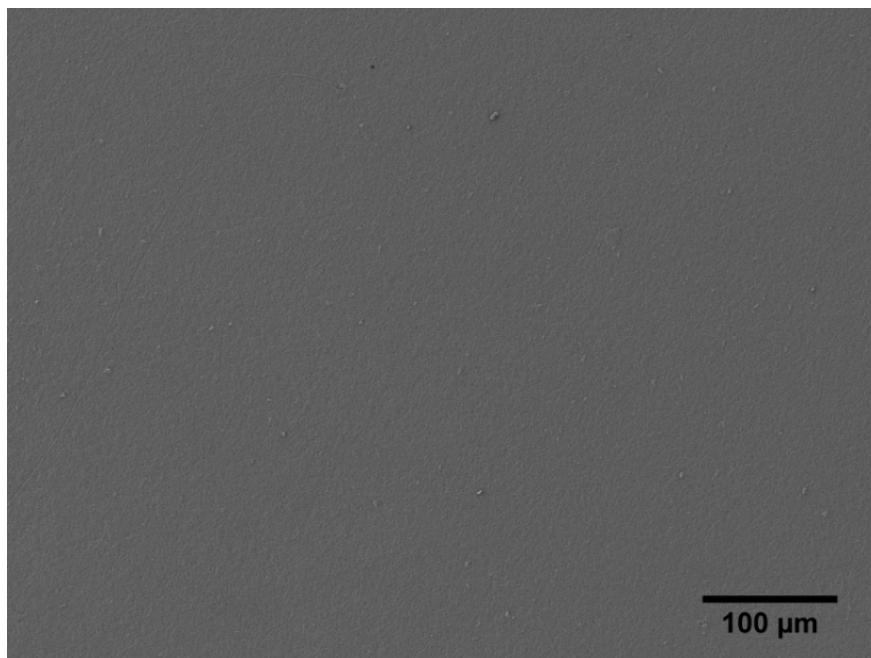


Figure 4.9 SEM of the surface of solution cast PVDF showing a very smooth surface with few defects.

The solution cast film with carbon nanotubes looks identical under SEM but shows large carbon nanotube agglomerates near the surface, shown in Figure 4.10 these agglomerates are close enough to the surface that they still drastically increase the scatter in the electrical tracking data. The electrospun samples with or without carbon nanotubes are near identical under SEM (see Figure 4.11) and they have a very heterogeneous surface. The increase in RMSE for the carbon nanotube sample is hypothesized to be due to some interaction between the carbon nanotubes and the surface, however because they are well segregated in the electrospun fibers the effect is minimal.

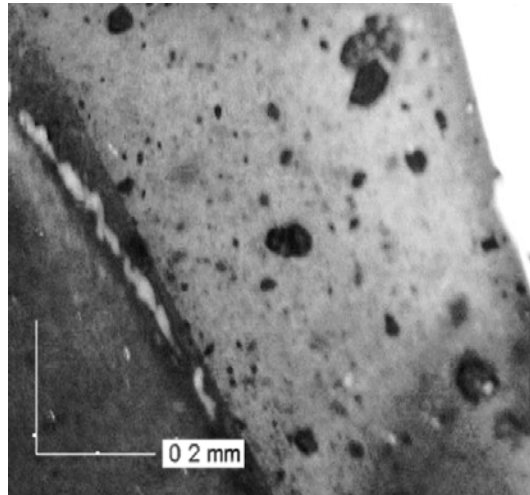


Figure 4.10 Optical micrograph showing the surface of solution cast PVDF with agglomerated carbon nanotubes.

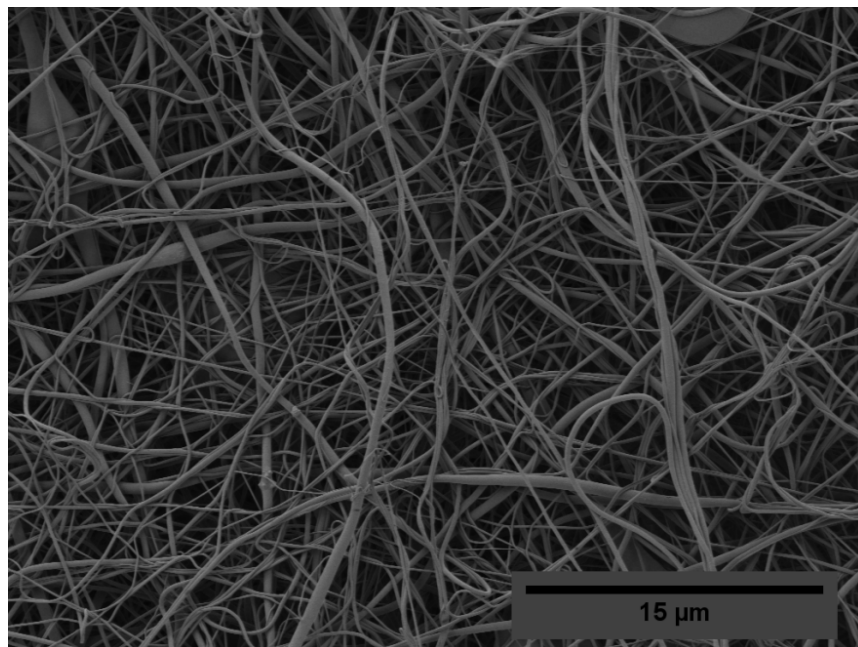


Figure 4.11 SEM micrograph of electrospun PVDF. The fibrous morphology is unchanged by the addition of carbon nanotubes,

The SEM micrographs show that surface quality is the reason for a reduction of the RMSE of the composite sample as well. Figure 4.12 shows an SEM micrograph of the composite sample without carbon nanotubes while Figure 4.13 is an SEM micrograph of a sample with carbon nanotubes included. These show that the carbon nanotube sample had much better wetting during the infusion process and as a result has a similar RMSE to the solution cast sample. It may be possible to achieve a similar result through modification of the processing parameters for the composite process; however in the current process the carbon nanotube content seems to improve the ability to achieve a fully dense infusion and allows better separation of the carbon nanotubes and surface; therefore the variability is much lower.

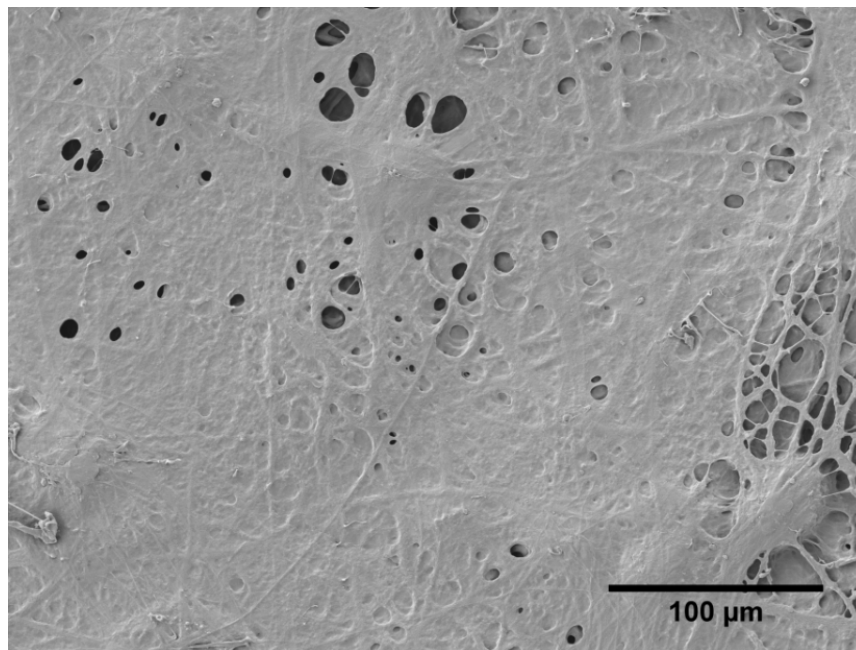


Figure 4.12 SEM micrograph of the electrospun/solution cast PVDF composite.

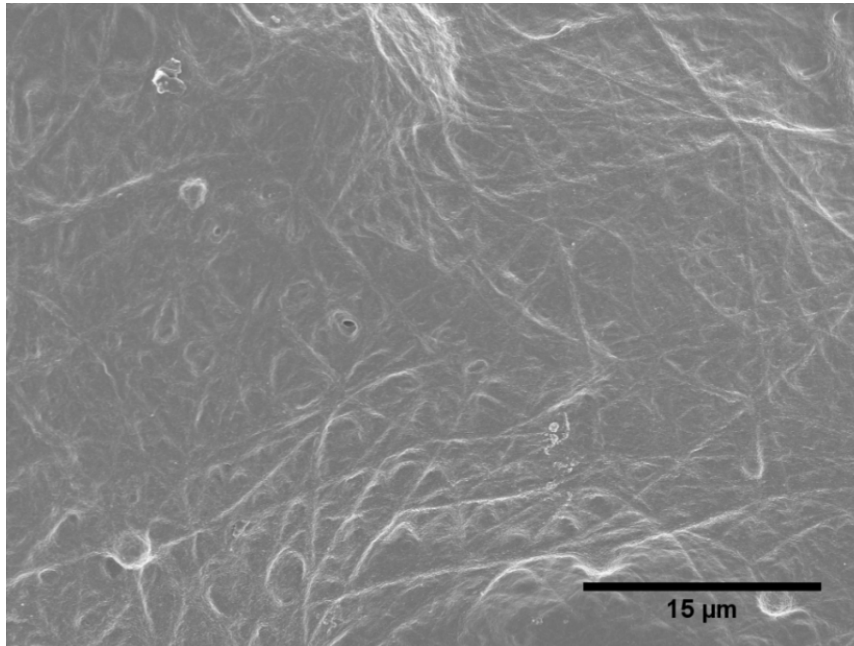


Figure 4.13 Electrospun/solution cast PVDF with carbon nanotubes integrated in the electrospun phase. The composite with carbon nanotubes has slightly better wetting and a more homogenous surface.

In order to create a design guideline for electrode placement, sample size, and voltage in the poling process the minimum electrical surface tracking line can be added to the corona discharge curve. The minimum path between both electrodes is around the surface of the material. This can be defined as the “overlap length” as illustrated in Figure 4.14. Figure 4.15 shows the combination of both data sets given in order to determine the safe minimum overlap length in the sample for any specified voltage, so knowing the thickness and electric field strength required the minimum sample geometry is prescribed.

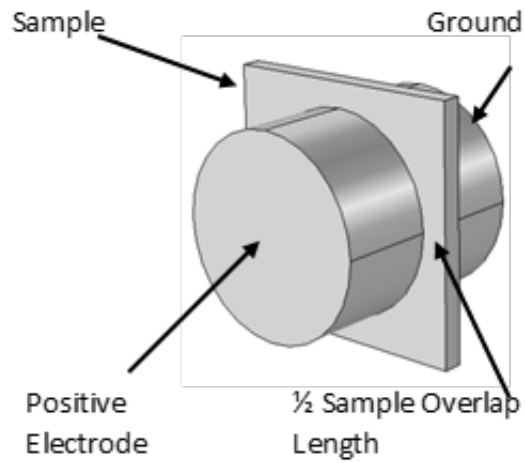


Figure 4.14 Illustration of the electrode/sample configuration

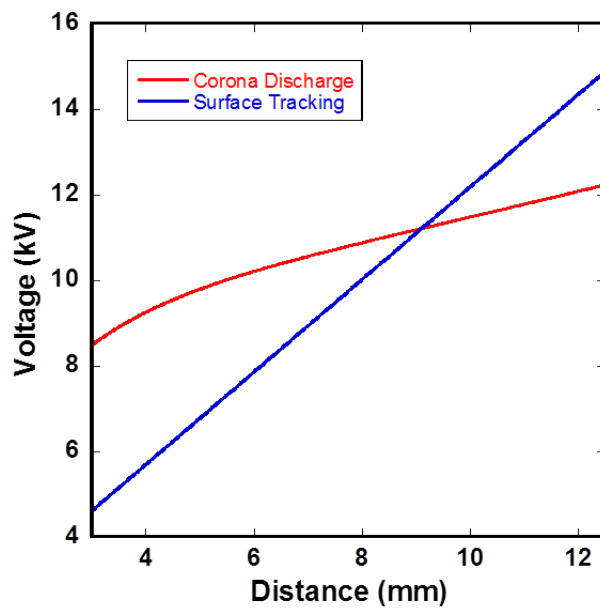


Figure 4.15 The results of corona discharge and electrical surface tracking initiation voltage. The minimum sample overlap length to prevent both effects can be determined by ensuring the distance is large enough that the voltage does not exceed either curve.



### 4.3.2 Dielectric Breakdown

In order for the poling process to succeed a high enough dielectric breakdown strength is a critical material property and is increasingly important when adding porosity (via electrospinning) or carbon nanotubes, which are both very conductive compared to the PVDF. An electric field strength of 30MV/m [66] is required in order to pole PVDF. Figure 4.16 shows the dielectric breakdown strength for the various PVDF films.

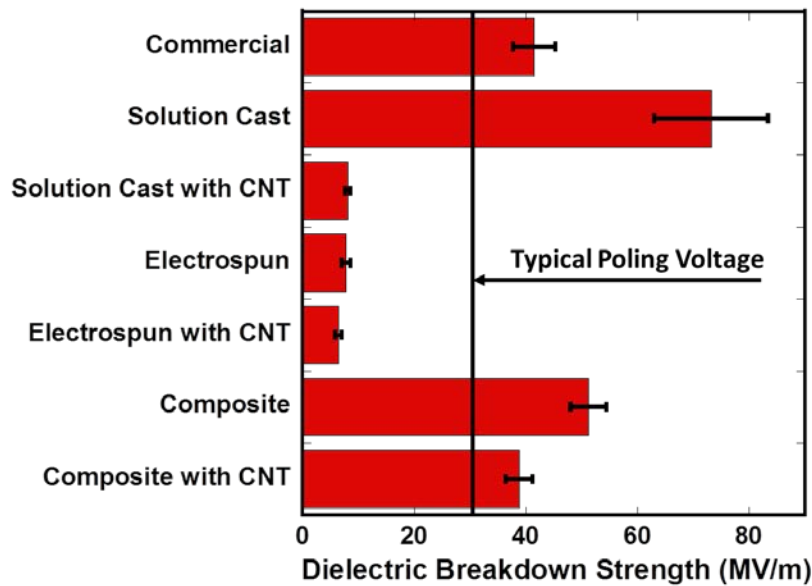


Figure 4.16 Measured dielectric breakdown of PVDF films compared to reported poling voltage. Both composite samples are above the threshold of dielectric breakdown strength and are able to be poled, whereas carbon nanotube infused solution cast samples and electrospun samples are below the threshold and cannot sustain a high enough electric field to pole. As expected both the commercial and solution cast exceed the poling threshold.

The  $\beta$ -phase polymorph of PVDF required for piezoelectric properties is thermodynamically favorable, but kinematically unfavorable; this means that during solution casting the polymer chains require greater mobility for longer periods of time while crystalizing and gives it a higher dielectric breakdown strength of the commercial film, which was processed from melt. When adding carbon nanotubes to a solution however, this time and mobility also induces long-term re-agglomeration of carbon nanotubes which creates spanning clusters allowing for the formation of percolating networks. The data show this as a drastic reduction in dielectric breakdown strength. The electrospun samples similarly degrade the dielectric breakdown strength through clusters of air – which has a much lower breakdown strength than the PVDF.

The composite process allows to keep the carbon nanotubes frozen in place while achieving a good dispersion during consolidation so that re-agglomeration does not occur and allows for a fully dense film. To image the morphology of the as-produced composite specimens were freeze fractured by dipping them into liquid nitrogen to cool below the glass transition temperature. Upon removal from the liquid nitrogen the specimen was immediately broken. Figure 4.17 shows the freeze fracture surface of a composite film demonstrating that a high degree of consolidation can be achieved while maintaining the microstructure of the electrospun morphology. The process of fracture splits the consolidated film into layers along planes formed by the persistent electrospun fiber morphology.

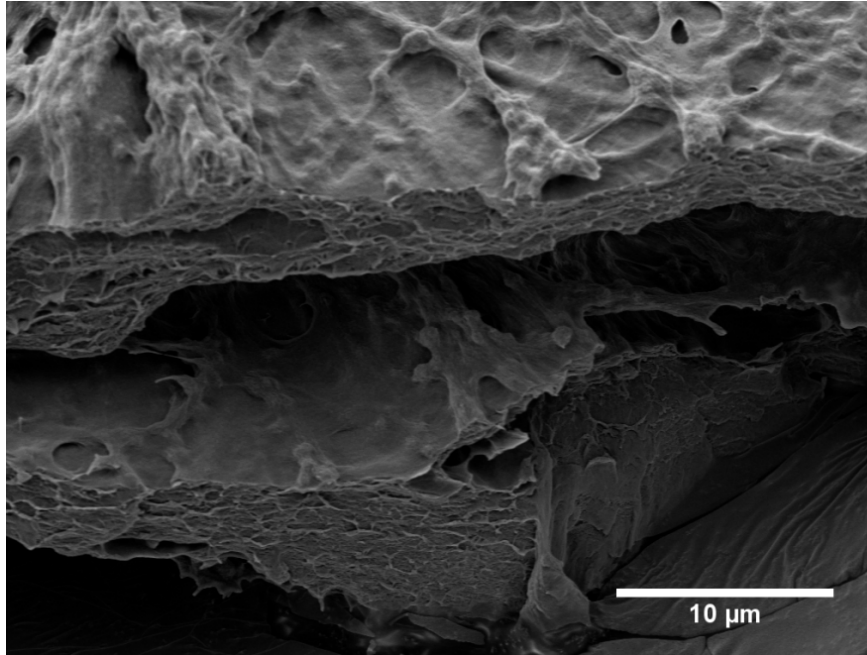


Figure 4.17 Freeze fracture SEM micrograph of the composite PVDF film with carbon nanotubes demonstrating the near-fully dense internal structure which allows the composite to sustain higher electric fields while maintaining the advantage of integrated carbon nanotubes.

#### 4.4 Conclusions

Chapter 2 studied the effects of adding carbon nanotubes to a PVDF matrix to determine the best method for improvements in the piezoelectric strength. This motivated the selection of the electrospinning process which was demonstrated to be able to produce sub percolation threshold carbon nanotube reinforced PVDF nanofiber films in Chapter 3. However, the inherent porosity of these films causes an inherently low dielectric strength. This is a key drawback to electrospinning as a method of manufacturing a high performing piezoelectric composite and motivated the study into the films interaction with high strength electric fields.

Corona discharge, electrical surface tracking, and dielectric breakdown were studied for PVDF thin films with and without carbon nanotubes added. The surface tracking mechanism was shown to be largely dependent on the quality of the surface quality of the thin film. The minimum required surface tracking initiation voltage was shown to be very similar across samples types; however the scatter showed that electrospun films have a much higher incidence of surpassing the minimum voltage. Combined with corona discharge tests to characterize the unique electrode setup this data are used to produce a set of design guidelines for use in the poling process for PVDF films showing a trade off in failure mechanism between surface tracking at lower overlap lengths, and corona discharge at higher overlaps. Dielectric breakdown strength tests proved that breakdown was the key failure mechanism for electrospun films, as well as solution cast films containing carbon nanotubes. The solution cast film failed because the carbon nanotubes formed agglomerates when processed which allowed for a conductive path between both electrodes. The electrospun films failed because of electrical discharge through the porosity in the material.

Next, a process of improving the dielectric strength of the electrospun fiber mats is investigated which is heavily inspired by traditional composites. Here the electrospun mat is re-infused with a PVDF solution in order to fill the porosity in the fabric. This resulted in a vast improvement in dielectric strength, and brought the carbon nanotube material over the threshold required to pole the PVDF. The dielectric breakdown strength of the composite was equivalent in magnitude to the strength of the neat solution cast films. This forms the motivation for Chapter 5, which thoroughly studies the carbon nanotube reinforced polymer-polymer composite films.

## Chapter 5

### **ELECTROSPINNING BASED POLYMER-POLYMER COMPOSITE WITH INTEGRATED CARBON NANOTUBES**

Chapter 3 introduced the concept of using electrospinning in order to achieve high quality dispersions of carbon nanotubes in electrospun PVDF. This material was shown to have a high  $\beta$  phase content which, combined with beneficial effects of the high electrical conductivity of the carbon nanotubes, (as discussed in Chapter 2) would allow for a significantly improved piezoelectric coupling behavior. However, as was studied in Chapter 4, the porosity of the electrospun fiber mat drastically reduces the dielectric strength of the material making it impossible to sustain a high electric field [52]. In order to solve this problem the electrospun fabric is used as a precursor to a novel self-reinforcing micro composite. The electrical breakdown behavior of these self-reinforced composites was discussed in Chapter 4. This chapter provides a detailed discussion of the processing approach and characterization of the as-processed morphology, crystal structure and mechanical properties.

In order to produce the PVDF polymer-polymer composite the electrospun PVDF with integrated carbon nanotubes is used as the fiber reinforcement, while the matrix is made up of PVDF cast from solution. The electrospun PVDF nanofibers provides a scaffold by which nanotubes are dispersed followed by infusion of a PVDF solution to form the polymer matrix. As highlighted in Chapter 4, nanotubes re-agglomerate when solution casting, resulting in poor surface tracking and dielectric breakdown. This process allows the nanotubes to be “frozen” in the structure of a high

$\beta$  phase electrospun fiber followed by solution forming of a high  $\beta$  phase matrix surrounding the nanocomposite fiber.

## **5.1 Experimental**

### **5.1.1 Materials and Processing**

All processing of PVDF was done using high molecular Kynar 761 of 20 wt% solution in Dimethyl Formamide (DMF) purchased from Sigma Aldrich with a purity of 99.9%. The PVDF was dissolved on a hot plate with a magnetic stir bar at 100°C in a glass hermetically sealed bottle and left to dissolve for 24 hours. This solution is then used for carbon nanotube stock preparation, solution casting, electrospinning and the micro infusion process.

For samples electrospun with carbon nanotubes a stock material of the specified nanotube loading was prepared by mixing carbon nanotubes into the same hermetically sealed bottle and stirred until roughly homogenous. In order to reduce agglomeration the material is then solution cast and pelletized; the pellets are used to feed a micro-scale twin screw extruder (DSM MICRO15) at 300°C for 15 minutes and extruded to yield highly dispersed non-agglomerated pellets. These pellets are re-dissolved into solution for the electrospinning process.

Electrospun films were produced in an environmentally controlled polycarbonate enclosure described in Chapter 3 and Appendix A. The solution is first loaded into an NE-1000 syringe pump (New Era Pump Systems) and pumped into the chamber via a sealed bulkhead at a flow rate of 0.03 ml/min. The electric field is applied between a 24 gauge stainless steel luer lock needle by and an aluminum collection plate at voltages of +13kV and -13kV respectively, a grounded ring is

placed between the two and surrounds the entire process to ensure electric field stability. The air supply is regulated to 80 psi and desiccated before flowing through a custom built diffuser at the base of the enclosure ensuring even and reliable flow of air conditioned to be under 3% relative humidity and 25°C.

A novel method of producing a micro-scale PVDF polymer-polymer composite was created in order to create fully consolidated films with the capacity of holding high quality dispersions of nano-scale reinforcement materials as a result of trying to improve the dielectric breakdown strength of the PVDF thin films without lowering the quality of the dispersion. The electrospun fabric acts as the fiber-phase scaffold holding the nano-particulate and a 20 wt% PVDF solution is used to fill the space between the fibers and layers.

As shown in Figure 5.1, the electrospun fabric is placed on top of a flat aluminum tool plate and the PVDF solution is dispensed on top of it of the electrospun film using a syringe so that a thin layer can be seen above the material. The capillary effect of the fibers causes the solution to be rapidly absorbed into the free space in the fabric. Next, a flat circular aluminum caul plate is placed on top of the composite with the dual purpose of exerting uniform pressure over the surface of the layup and creating a tool-quality surface for the composite thin film. A highly porous breather layer is then placed over both the sample and caul plate to aid in evacuating air around the sample and creating a path for solvent evaporation. A vacuum line is placed in direct contact with the breather and the entire layup is sealed under a vacuum bag with vacuum bag sealant. The assembly is then pulled under vacuum and allowed to dry for 48 hours. After the vacuum pressure was released and the composite is dried for an additional 24 hours in order to ensure evaporation of any remaining solvent.

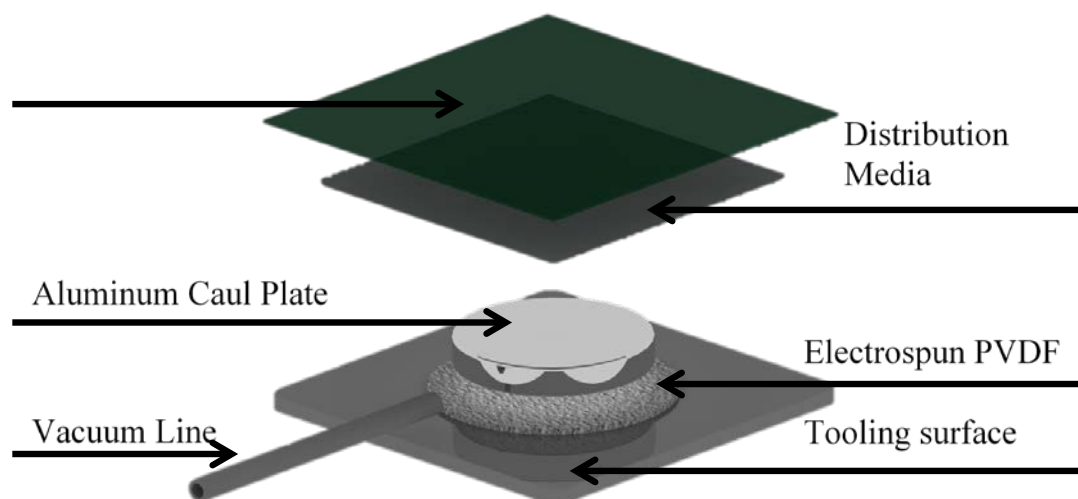


Figure 5.1 The composite processing layup for production of PVDF polymer-polymer thin films includes aluminum tooling and caul plate to produce tooling-quality finish on the film, distribution media connected to a vacuum line to vacate the air and solvents, and a vacuum bag to ensure a proper seal. The layup is left under vacuum for 48 hours and subsequently left in ambient pressure for 24 hours to ensure complete solvent evaporation.

The composite can also be heated during the casting process, this is done by placing the aluminum tooling surface on top of a digitally controlled hot-plate and set to 60°C for the entirety of the process. The resulting composite film is visually inspected to ensure that it is macroscopically homogenous. Solution cast films were also prepared for characterization, as discussed in Chapter 3, Section 4.1.

### 5.1.2 Crystal Structure Characterization

Information on the crystallinity was analyzed through both differential scanning calorimetry (DSC) and wide angle x-ray scattering (WAXS). In DSC the



melt endotherms give information on the crystal phases present and also the percent crystallinity. All samples were tested with a Mettler-Toledo™ DSC-1 with a heat ramp from 30 to 180 degrees at 5 degrees per minute. A second ramp was done for each sample after controlled cooling to ensure that they were identical for all samples.

X-ray scattering was used to identify the crystal phases present. Because there are distinct peak differences between the  $\alpha$  and  $\beta$  phase of PVDF it is possible to calculate the fraction of each component to the whole (ignoring peaks which are common to both polymorphs). A Bruker DAVINCI II diffractometer was used equipped with a 2-D VANTEC 500 detector. The x-ray source produced a  $\lambda_1$  of 1.54060 Å and a  $\lambda_2$  of 1.54439 Å at a voltage of 40kV and current of 35μA. The analysis technique and experimental parameters are discussed in Chapter 3, Section 4.2.1.

### **5.1.3 Electron Microscopy**

Scanning electron microscopy (SEM) was used to image the fracture surfaces. A Zeiss AURIGA™ 60 Crossbeam™ FIB-SEM is used with an accelerating voltage of 3kV in secondary electrons secondary ions (SESI) detection. In order to view the microstructure some samples were fractured using a freeze fracture technique by submerging the specimens under liquid nitrogen until they reach thermal equilibrium. This allows a brittle fracture. All samples were sputter coated with a 6:4 ratio of gold and palladium for 1 minute.

### **5.1.4 Mechanical Testing**

Specimens for mechanical characterization were prepared by cutting the as-processed films to width using a tool that holds two razor blades in parallel at a fixed

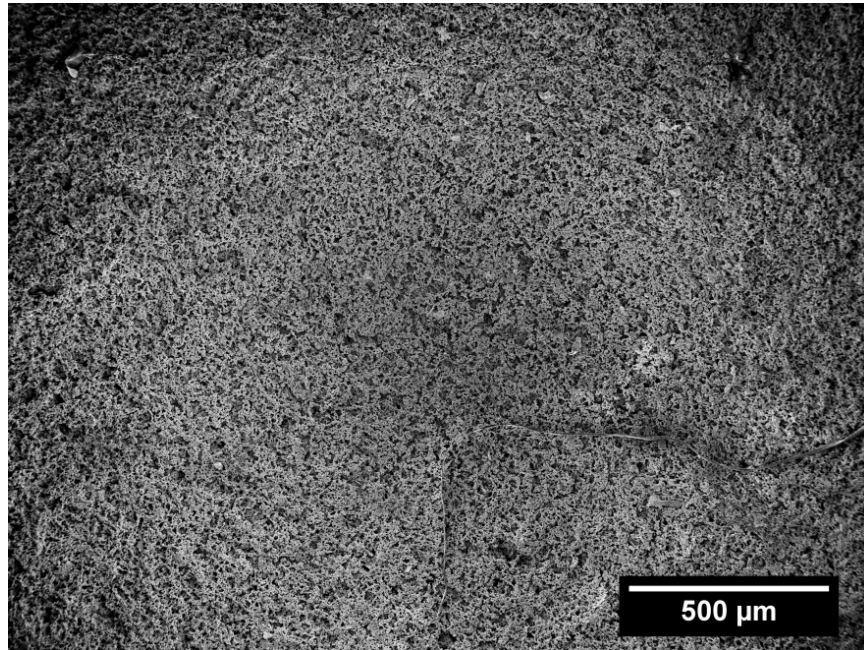
width of 3.2 cm and a length of 2.54 cm. Before testing, fiberglass tape was applied to the ends of the film to act as an end tab for mechanical testing. The films were tested in tension using a fixed displacement micro load frame equipped with mechanical grips at a displacement rate of 1 mm/min. Strain is measured from the displacement. Some error in the strain measurement may be possible due to the compliance of the fiberglass tape, but this compliance will be similar for all specimens.

## **5.2 Results and Discussion**

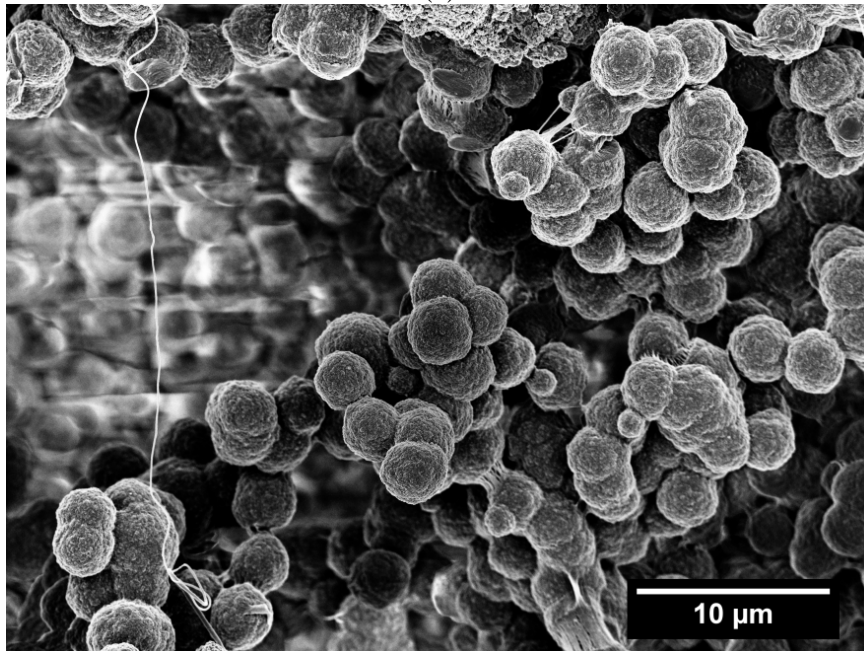
### **5.2.1 Physical Microstructure**

As a composite of both the electrospinning and solution casting process it is important to first examine each component independently. Solution cast PVDF is highly homogenous but has a micro-porous structure (Figure 5.2a). Upon closer examination of the micro-porous structure it is shown that the pores are formed because the PVDF creates spherulitic structures as the solvent evaporates (see Figure 5.2b).

The electrospun PVDF (Figure 5.3) has a completely different structure, very typical of electrospun fibers. Most of the fibers are in the 200 nm range and have a very smooth surface finish; however some larger fibers are formed as well as a small amount of beaded structures. Beaded structures can be produced depending on solvent evaporation rate during the electrospinning process [44].



(a)



(b)

Figure 5.2 Solution cast PVDF is shown to have an (a) micro-porous structure formed of (b)  $\beta$ -phase spherulites

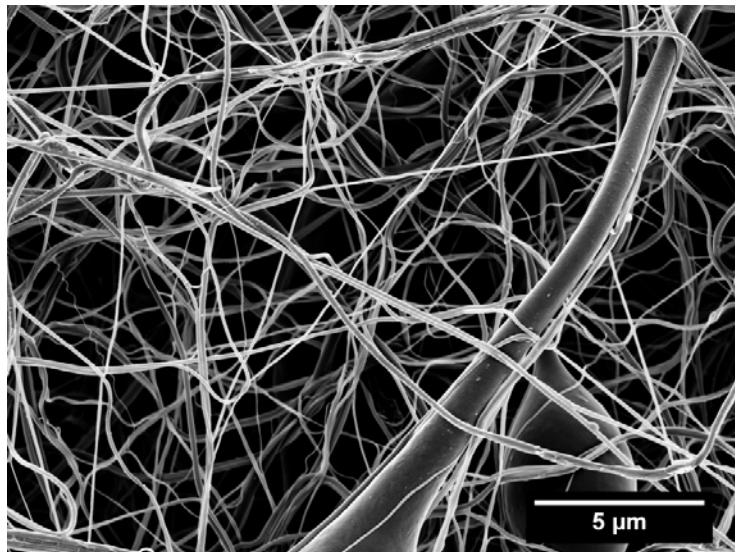
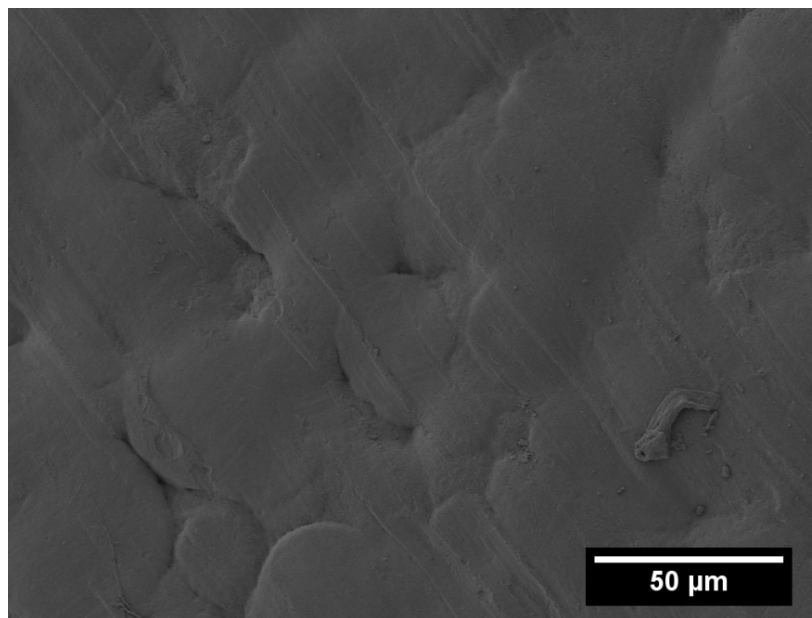
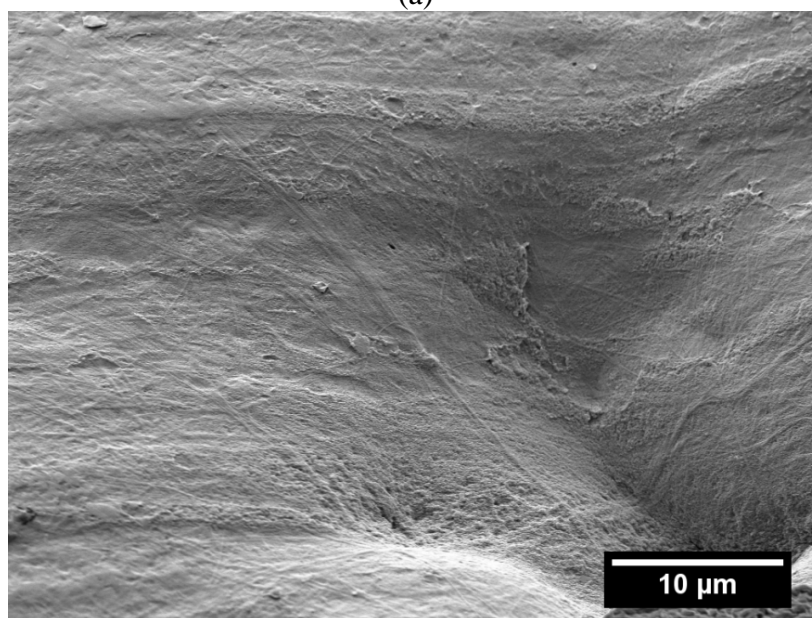


Figure 5.3      Electrospun morphology is nearly identical with or without carbon nanotubes with fibers approximately 200 nm, though some larger fibers and beads also exist.

Combining electrospinning followed by secondary consolidation using vacuum infusion followed by controlled drying results in a composite that has a textured surface. The SEM micrograph in Figure 5.4a shows a clearly visible imprint from the aluminum tooling surface. Some surface voids are also visible from air and solvent trapped during the infusion process. At higher magnifications (Figure 5.4b) the highly dense fibrous structure from the electrospun film is visible. The texture provides some evidence that the fibers do not dissolve during the solvent re-infiltration and drying of the PVDF matrix. The underlying structure of the composite appears to be fully dense, with little or no small-scale voids between the polymer nanofibers. This further indicates that there is good wetting between the electrospun fibers and the solution cast matrix.



(a)

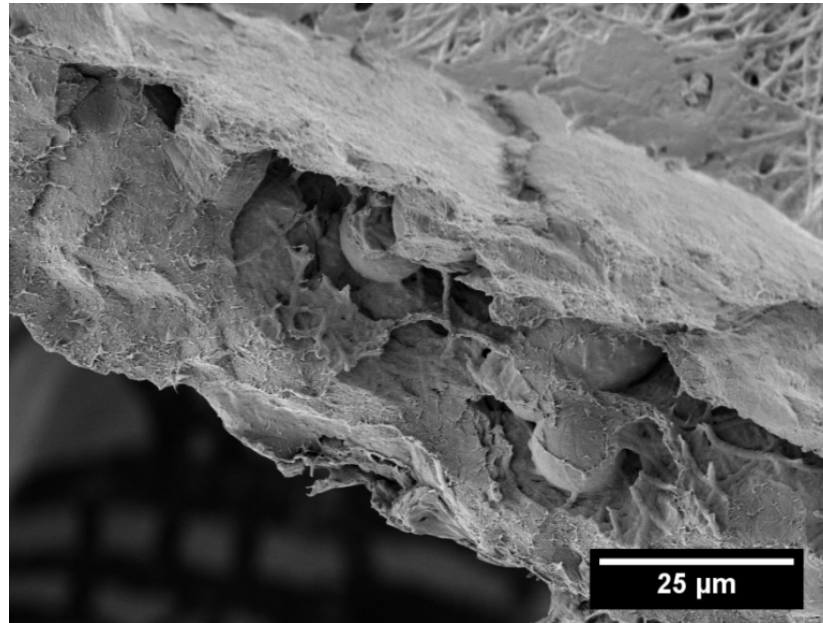


(b)

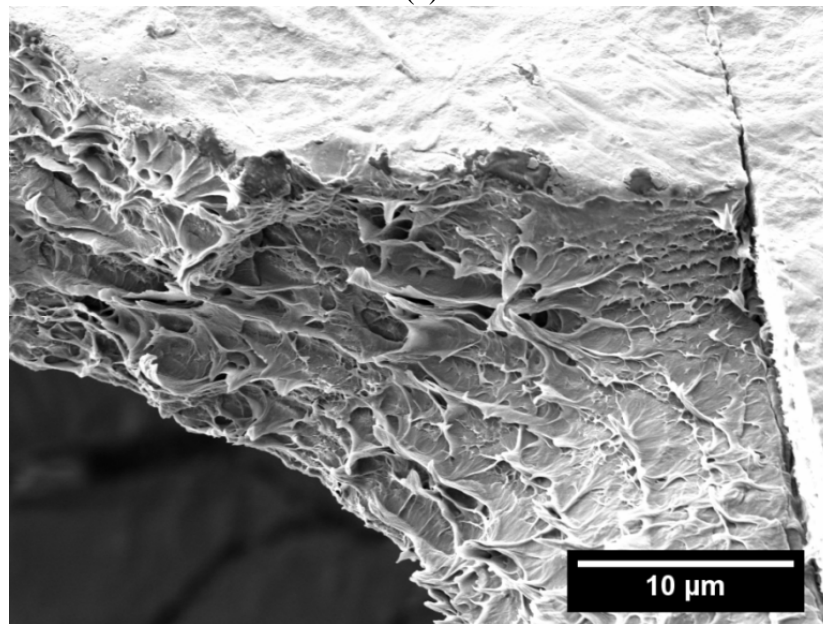
Figure 5.4 Surface of PVDF polymer-polymer composite showing (a) a textured surface and voids from trapped air and solvent and (b) evidence of fully dense electrospun composite structure just under the surface.

In order to examine the internal structure of the PVDF composite freeze fracture specimens were imaged. Figure 5.5a shows the fracture surface for a neat PVDF polymer-polymer composite with no process heat added – the fracture shows a layered structure with broken electrospun fibers in a matrix of PVDF. There is also the presence of visible beads in the electrospinning process. Figure 5.5b shows the composite sample that was cast at 60°C. It shows slightly higher consolidation and more fusion between the electrospun fibers and the matrix. Although there is some dissolution of the fibers at higher temperature the fibrous structure of the composite is still clearly visible.

Adding carbon nanotubes to the fibers stiffens the fiber phase and forces a slightly different mode of failure. While fracturing there is an internal delamination between planar sections of electrospun PVDF. Figure 5.6a shows the fracture for the composite with 0.1% carbon nanotubes in the fiber phase and Figure 5.6b shows the fracture for the composite with 0.25%. The 0.1% carbon nanotube composite's electrospun phase still has some visible beading but in the 0.25% composite the fibers are bead free. It is also known from Chapter 3 that the presence of more carbon nanotubes also promotes the formation of the  $\beta$  phase. Both samples show that the process achieves a fully dense film with only minor nano-scale voids. In all cases the fibrous structure of the electrospun film is preserved during the infusion and drying process. The combination of a high degree of dispersion of the nanotubes produced by the electrospun scaffold with the fully dense composite structure is important if future applications in sensing and actuation.

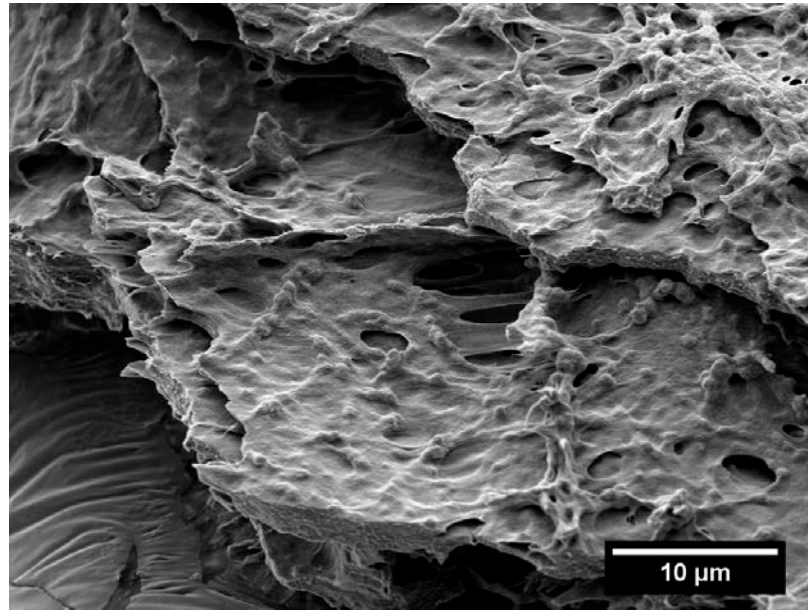


(a)

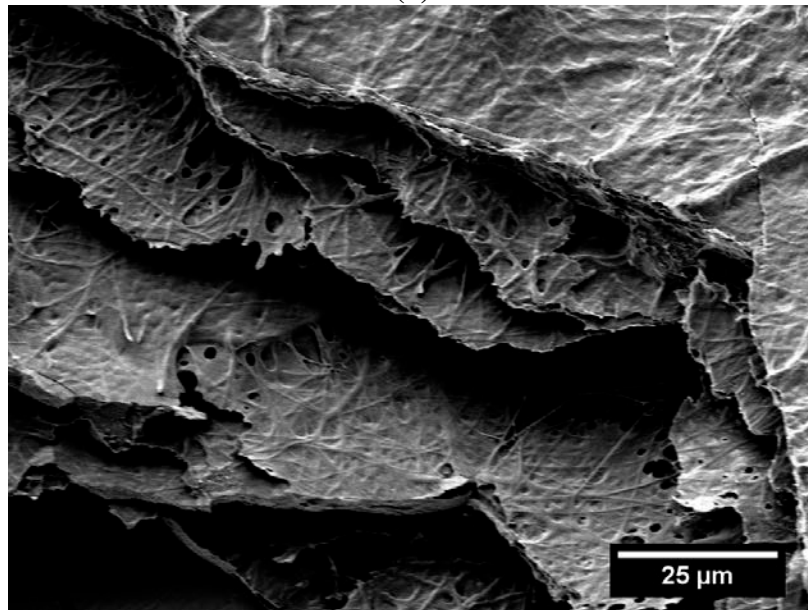


(b)

Figure 5.5 Freeze fracture of neat PVDF polymer-polymer composite processed at room temperature (a) having a layered brittle structure and very heterogeneous internal microstructure and processed at 60°C (b) demonstrating a higher degree of polymer chain diffusion between the matrix and fiber phase allowing for a more homogenous internal microstructure.



(a)



(b)

Figure 5.6 PVDF composite with electrospun phase containing 0.1wt% carbon nanotubes (a) and 0.25% carbon nanotubes (b). Both samples show a brittle fracture with layer by layer delamination along electrospun planes. The composites have very good consolidation and few small scale voids.



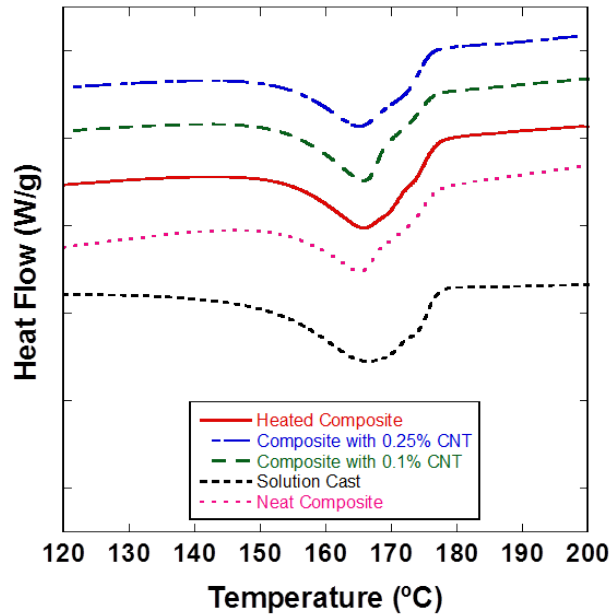


Figure 5.7 Thermal analysis of composite and solution cast PVDF films – DSC curves showing the onset of melting and peak endotherm positions are similar regardless of processing parameters.

### 5.2.2 Composite Crystal Structure Characterization

Understanding the crystal structure of the composite is critical to study of the capabilities of the PVDF films. In order to properly pole a PVDF film in order for it to exhibit piezoelectric properties first it must consist largely of the polar  $\beta$ -phase polymorph. Because the non-polar  $\alpha$ -phase is more thermally stable, production of the  $\beta$ -phase is non-trivial. DSC is used as a first step to understanding the crystal structure, and the integral is used to determine the crystallinity while WAXS is used to refine understanding of the crystal structure. Figure 5.7 shows the DSC curves for each of the composite samples as compared to the solution cast material while Figure 5.8 summarizes the peak areas for each endotherm representing crystallinity.

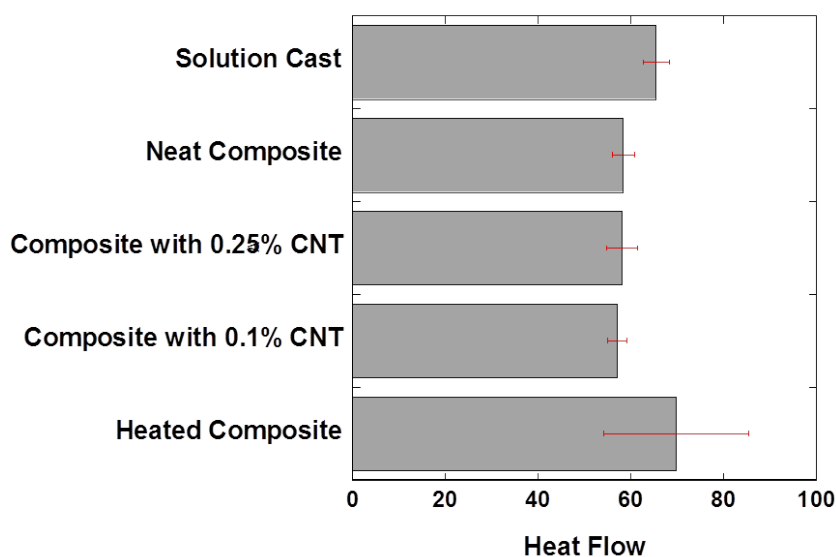


Figure 5.8 Integral of the melt endotherm showing that the heated composite process results in slightly higher crystallinity.

The DSC data show that all composite samples are very similar in crystal structure, with only subtle differences in heat flow and melting peaks. The integral shows that the heated composite film has the highest degree of crystallinity; however the carbon nanotubes have no effect on overall crystallinity when used in the composite process. The WAXS results, shown in Figure 5.9, agree with the DSC findings.

Regardless of carbon nanotube content or temperature the type of crystal structure is consistent. This can be further shown using peak fitting analysis – this involves using the ratio of the  $\beta$  peaks to the total crystal structure in order to calculate total  $\beta$ -phase crystal content (see Table 5.1). All of the polymer-polymer composite samples had  $\beta$ -fractions of between 0.85 and 0.87.

Table 5.1  $\beta$  fraction of the PVDF crystal structure

| Sample           | Baseline | Heated | 0.1%<br>nanotube | 0.25%<br>nanotubes |
|------------------|----------|--------|------------------|--------------------|
| $\beta$ Fraction | 0.87     | 0.86   | 0.87             | 0.85               |

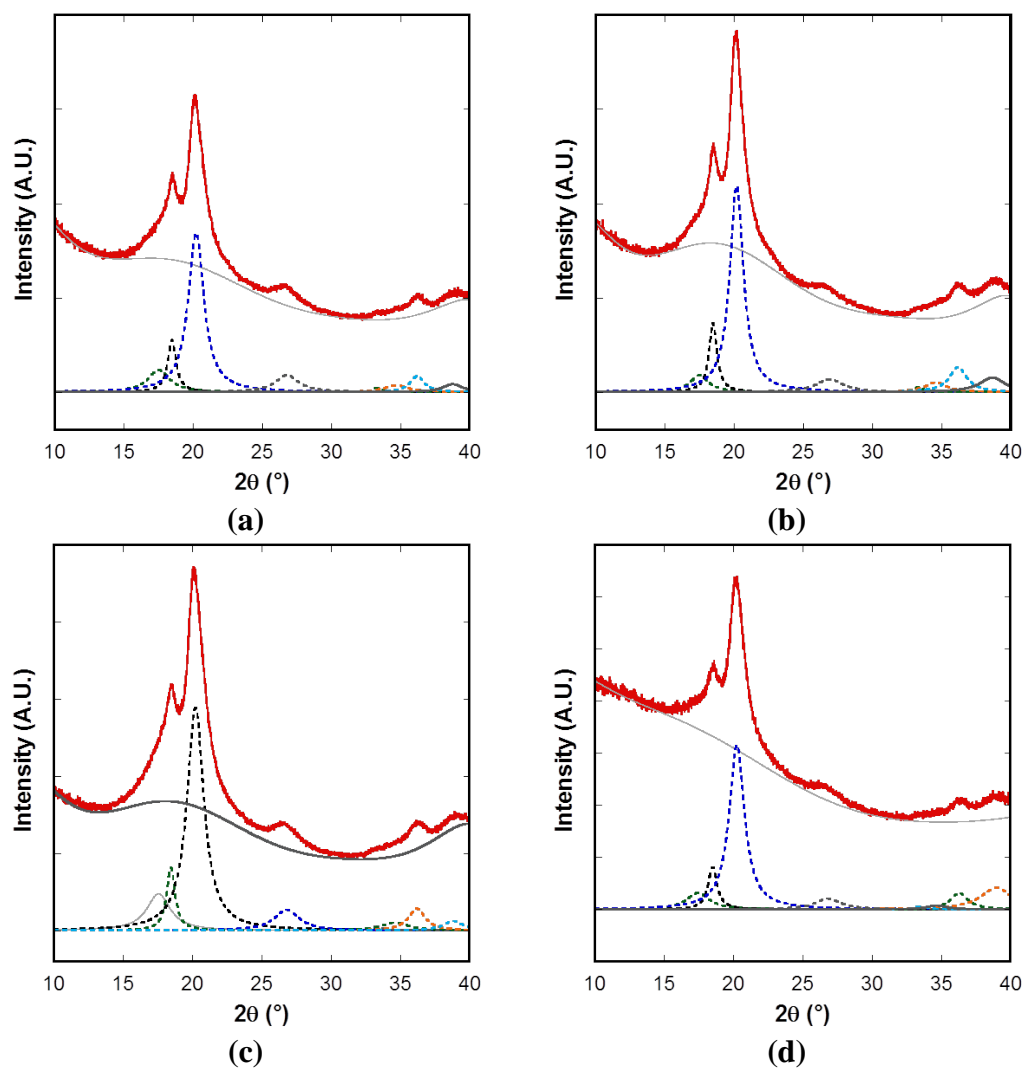


Figure 5.9 WAXS patterns for each type of composite film showing that regardless of process conditions the micro infusion system consistently produces films with high  $\beta$ -phase content. (a) Neat Composite (b) Heated Composite (c) Composite with 0.1% carbon nanotube (d) Composite with 0.25% carbon nanotube

Furthermore, the FTIR results from Section 3.4.3.3, Figure 3.16 can be appended with the data from the composite system. Figure 5.10 shows that the same  $840\text{cm}^{-1}$  and  $1290\text{cm}^{-1}$  peaks are confirmed in the composite film; confirming the presence of  $\beta$  phase PVDF. Similarly the DSC results in Section 3.4.3, Figure 3.10 can be appended to include results from the composite sample. In Figure 5.11 it is shown that it is nearly identical to the solution cast film.

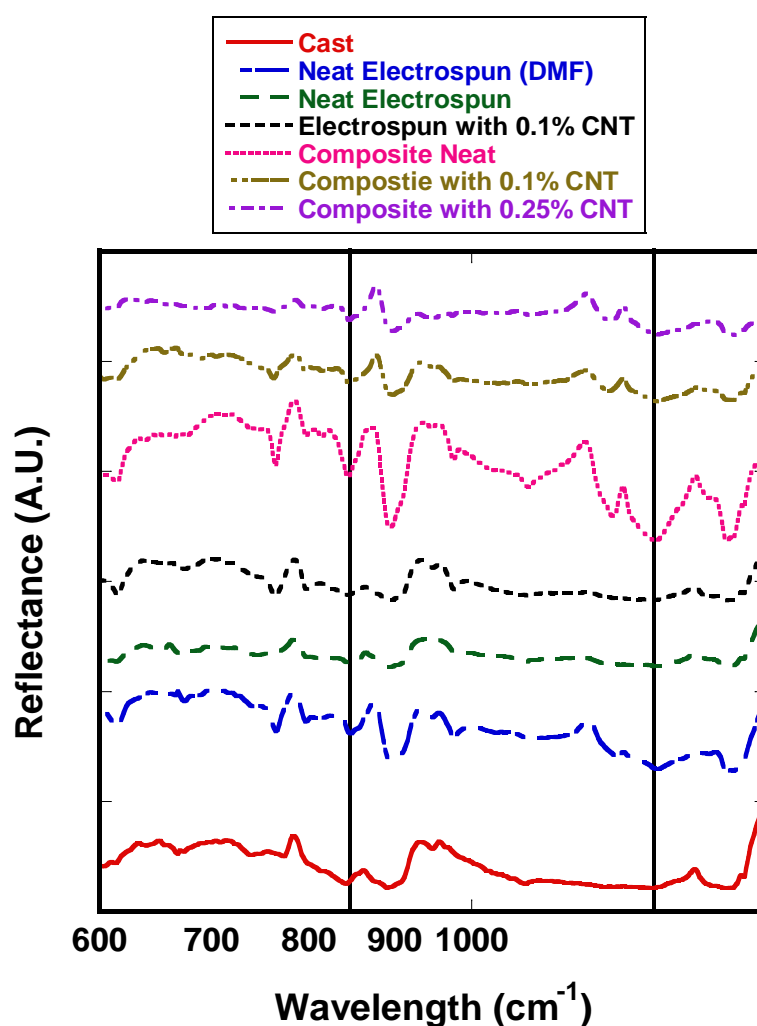


Figure 5.10 FTIR data confirming the existence of  $\beta$  phase PVDF

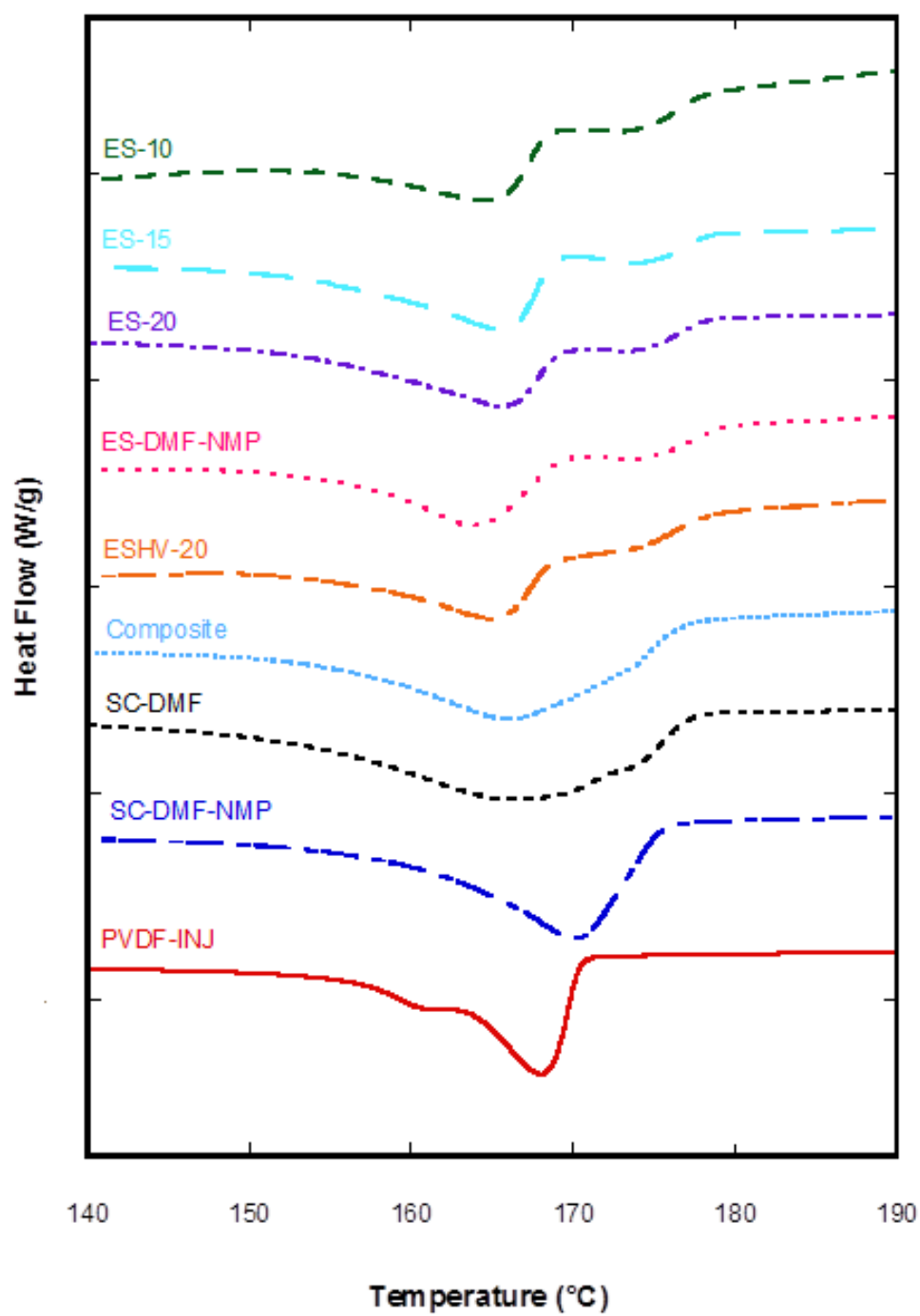


Figure 5.11 DSC results appended with the composite data. Note that the DSC curve of the composite is almost identical to that of the solution cast film.

### 5.2.3 Mechanical Properties

In order to evaluate the polymer-polymer composite films, the effect of processing on stiffness and strength was examined (see Figure 5.12). As expected the strongest of the films is a standard solution cast film – the films homogeneity means that it contains much fewer sources of the stress concentrations which accelerate failure.

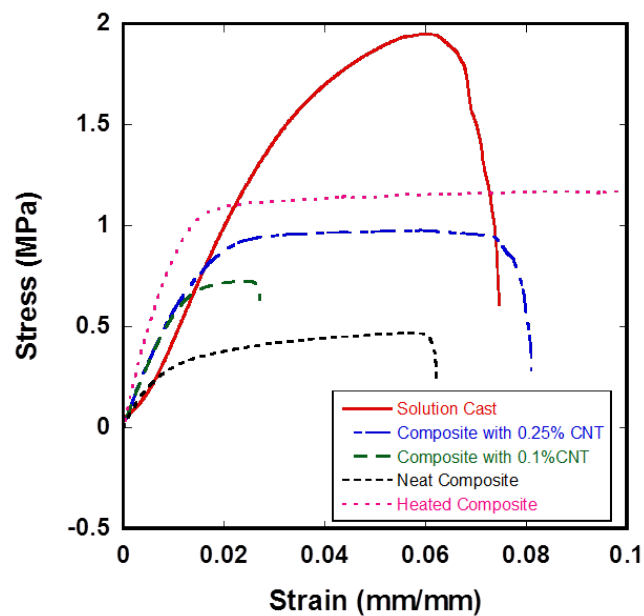


Figure 5.12 Stress-strain curve for composite samples

The differences in stress strain curves between the solution cast and composite reveal very different failure mechanisms. The solution cast film fails in a very classical plastic failure mode, increasing until a peak load is reached and demonstrating ductile failure. The composite films behave very differently, showing a failure mechanism more similar to high elongation composites. The peak load is reached and

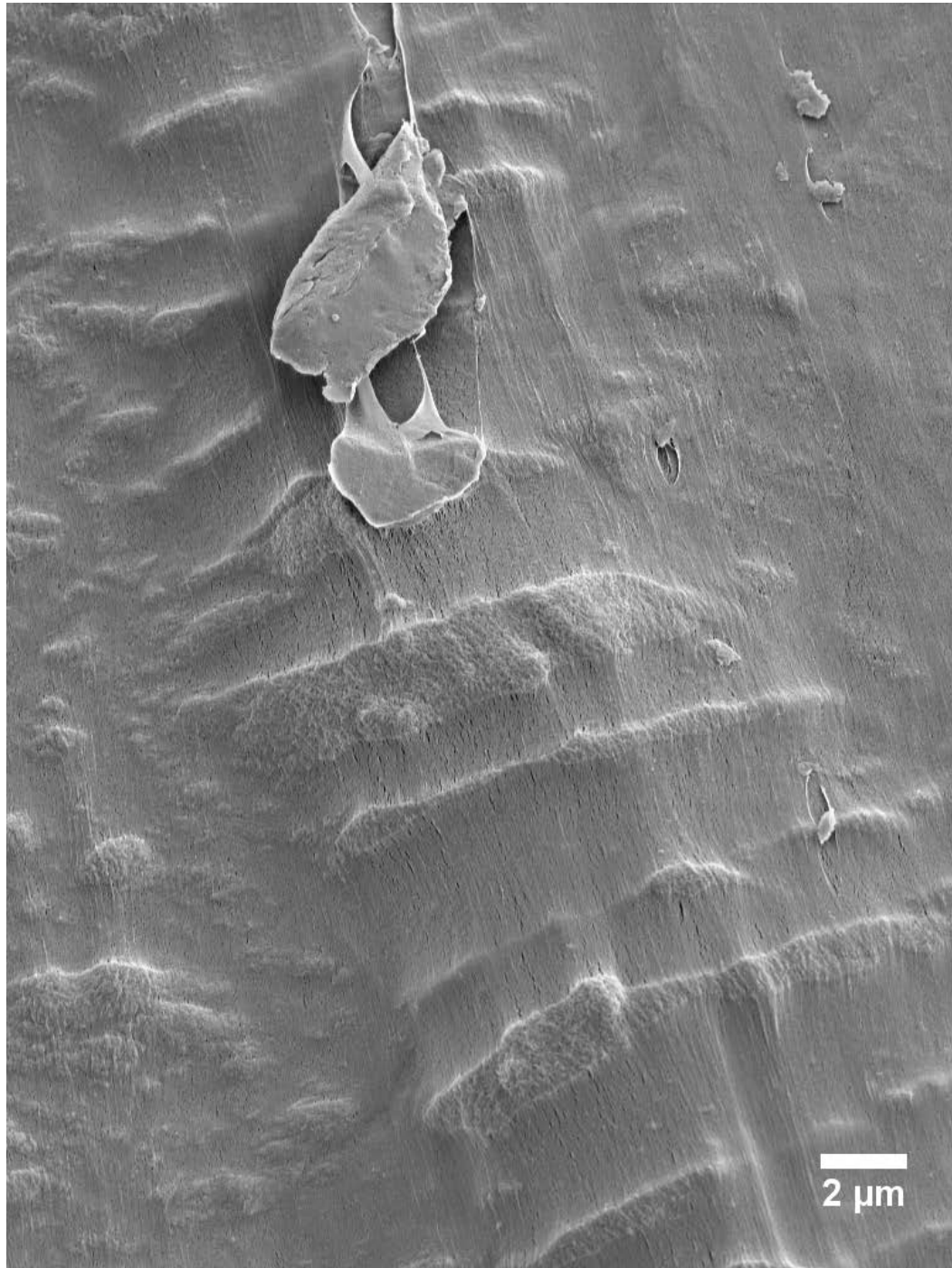


Figure 5.13 SEM micrograph showing a composite polymer-polymer film containing 0.25wt% carbon nanotube reinforcement in the fiber phase. The micrograph shows fibers spanning the cracks formed in the matrix prior to failure.

stress is redistributed within the composite as fibers shear from the matrix and cracks propagate. Figure 5.13 shows a composite film with 0.25wt% carbon nanotube reinforcement just before failure. It is possible to see cracks beginning to form in transverse direction in the matrix, however the electrospun fibers are aligned and bridging the cracks resisting further strain. This is consistent with the classical composite pull-out type failure mechanism where fibers must individually shear and fail in their interface with the matrix before the composite is no longer capable of sustaining load. Here the very high stiffness of the carbon nanotubes plays a very important role, with the 0.25wt% carbon nanotube reinforced samples showing a doubling of peak load compared to the neat composite.

Of key interest is the film processed under heated conditions, which is demonstrably the strongest and stiffest having nearly double the stiffness of the unheated composite films (see Figure 5.14). This is because the temperature allows for diffusion between the polymer chains in the fiber phase and matrix of the material. Figure 5.5b shows a large degree of adhesion between the fiber phase and the matrix. Even though the samples were freeze fractured the failure the micrograph still reveals micron scale deformation before failure. Manufacture at elevated temperature while under vacuum allows for a much larger degree of mobility between the fiber and matrix phases while still slowing the evaporation rate and reducing the micro porosity typically associated with elevated temperature casting. This allows the outer shell of the electrospun fiber phase to dissolve slightly and fuse with the matrix – however because it is under vacuum the degree of freedom is well enough restricted that the core function of the fiber phase, acting as a scaffold, is maintained.



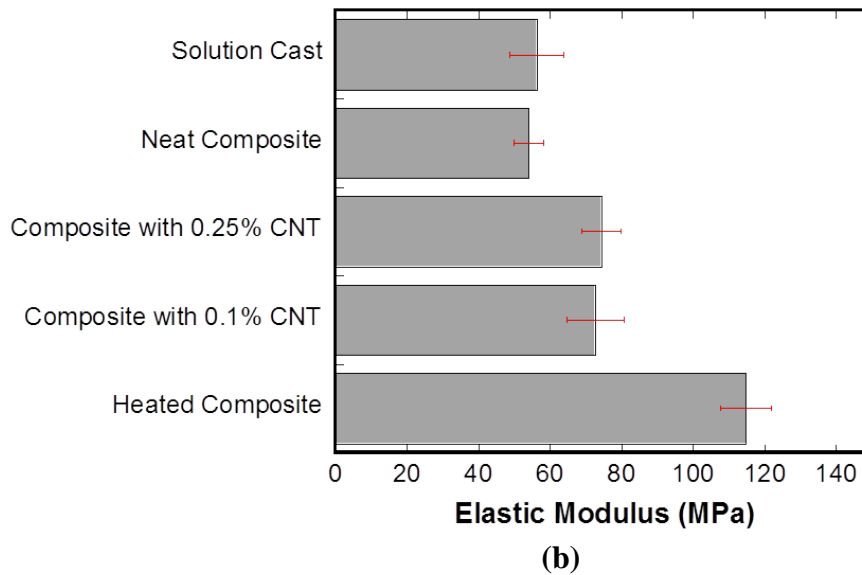


Figure 5.14 Calculated elastic modulus for each film.

### 5.3 Conclusions

Adding conductive nanoscale reinforcement is an attractive way to impart new mechanical and electrical properties to a material; in the case of PVDF carbon nanotubes are added in order to affect the electric field in order to improve the piezoelectric properties. Chapter 2 revealed that the optimal configuration for improving the piezoelectric strength of PVDF would be to have a large amount of carbon nanotubes while staying below the percolation threshold. Electrospinning (Chapter 3) was investigated as a manufacturing process capable of producing nanofiber films with large carbon nanotube content while avoiding electrical percolation. However, as demonstrated in Chapter 4 the high porosity of electrospun films reduces their dielectric breakdown strength by allowing for short circuits to form through the air gaps, stopping the film from sustaining the high strength electric field required for piezoelectric applications.

The proposed solution is to fill the porosity in the electrospun fiber phase with a PVDF solution and allow for the slow evaporation of the solvent. This causes a slight dissolution of the surface of the fibers in order to form a well bonded polymer-polymer composite which acts as a fully dense PVDF thin film with carbon nanotubes well dispersed in an electrospun scaffold. This work describes the process and investigates the combination of crystallographic, microstructural, and mechanical properties of this composite material and the impact of the integration of carbon nanotubes.

These films are shown to contain a high degree of the  $\beta$  phase polymorph of PVDF which is required for imparting piezoelectric properties on the composite. The microstructure was examined and shown to be a consolidated fully dense film while preserving the microstructure of the carbon nanotube containing fiber phase. This allows the fiber phase to act as a scaffold, effectively “freezing” the carbon nanotubes in place and arresting the formation of both agglomerates and percolating networks. Mechanical properties were also studied, showing that the addition of carbon nanotubes vastly improves the strength and stiffness of the polymer-polymer composite, as well as changing the failure mechanism from a traditional polymer ductile failure to a classical composite-type failure, indicative of fiber loading and shearing between the fiber and matrix phases.

## **Chapter 6**

### **CONCLUSIONS AND RECOMMENDATIONS FOR FUTURE WORK**

#### **6.1 Major Conclusions**

This work has focused on understanding the fundamental role of using carbon nanotube reinforcement in PVDF as a platform for piezoelectric composites. Prior to this work PVDF had been studied in great depth in order to understand the influence of crystal structure and piezoelectric properties, however only preliminary work had been done in exploring the potential benefits of using carbon nanotubes distributed within PVDF to improve the piezoelectric properties.

In order to understand the governing phenomenon in using carbon nanotube reinforcement in a PVDF composite, Chapter 2 describes two finite element analysis studies designed to investigate the mechanisms by which carbon nanotube reinforcement impacts the piezoelectric strength of the material. It was found that the phenomenon responsible for improvements in piezoelectric coefficient was the end effects and the electric field interactions between carbon nanotubes. It was shown that the most important factor in improving the piezoelectric coefficient was an increase in the number of carbon nanotubes, resulting in more ends and thus more interactions between nanotubes. These simulations also showed the detrimental effects of carbon nanotube short circuits, which are formed when the nanotubes bridge and form percolating networks. These two goals are naturally opposing because of the ease of which low dispersions of carbon nanotubes form percolating networks which by creating conductive paths within the material, thus requiring a unique solution.

Chapter 3 proposes the use of electrospinning as a manufacturing platform which has the ability to increase the number of carbon nanotubes added, while simultaneously increasing the percolation threshold and limiting the formation of short circuits within the material. This is possible because the diameter of the electrospun fibers is smaller than the length of the carbon nanotubes, forcing them to be segregated during processing. Because it is of key importance to the development of an improved piezoelectric platform, Chapter 3 also verifies that the electrospun fiber mats contain the proper  $\beta$  base polymorph of PVDF required for actuation and sensing. It was shown that adding carbon nanotubes past a threshold between 0.1wt% and 0.25% greatly increases the ratio of  $\beta$  phase crystallites in the film.

The major drawback in using carbon nanotube reinforced electrospun fiber mats is their poor dielectric strength. The porosity of the material makes it unable to sustain the high strength electric field required to pole the material, or to be practical in many piezoelectric applications. Chapter 4 studies various phenomenon associated with high voltage physics. Electrical surface tracking, corona discharge and dielectric breakdown are all failure mechanisms associated with the poling process. Here, design guidelines are given with which to avoid failure due to electrical surface tracking and corona discharge; and a solution is proposed with which to improve the dielectric strength of the carbon nanotube reinforced PVDF. Inspired by traditional composites processes a solution of PVDF is re-infused into the electrospun mat to form a polymer-polymer composite. This process fills the voids in the material resulting in the formation of a fully dense film. The dielectric strength of the new composite films is shown to be as high as solution cast films, also implying that the percolation threshold has not been surpassed.

Chapter 5 develops the process further and investigates the properties of the carbon nanotube reinforced polymer-polymer composite. The composite is shown to contain a high degree of the  $\beta$  phase PVDF required for the piezoelectric effect. The microstructure was studied in depth and was shown to be a consolidated fully dense film, while preserving the microstructure containing the carbon nanotubes. The electrospun fiber mat is shown to act as a “scaffold” for the carbon nanotubes, effectively segregating them and artificially increasing the percolation threshold while still allowing for high quality dispersion. The mechanical properties were also studied; showing that the carbon nanotubes had a significant impact on the strength and stiffness of the composite. The electrospinning process produces a polymer-polymer composite with a failure mechanism akin to fiber pullout in traditional fiber composites versus the simple plastic failure experienced by the solution cast PVDF films.

In summary, the carbon nanotube reinforced composite was shown to have many key attributes including:

- High carbon nanotube content
- Significantly increased percolation threshold
- Improved strength and stiffness
- High  $\beta$  phase polymorph content

This makes these films a very strong platform for future work in improving the piezoelectric properties of PVDF and other similar polymer ferroelectrics.

## **6.2 Recommendations for Future Work**

There are several paths forward for using the composite platform as a vehicle for improvements in piezoelectric coefficient. The first step would be a comparison

study of the piezoelectric properties of solution cast PVDF, neat polymer-polymer composite PVDF, and carbon nanotube reinforced composite PVDF. It may be possible for this study to be done by using a piezoelectric analyzer, however these are typically used to study PZT and other piezoelectric ceramics and may not work for PVDF films, which have much different mechanical characteristics. Alternative test methods have a key barrier – development of a flexible electrode system for use with the PVDF composite. Once an efficient electroding system is developed the films can be tested both in tension and in bending modes using a standard small scale Instron. Measurement of sensing capabilities will require a high sample rate high gain analog voltage measurement system. Measurement of actuation response will require implementing a proper piezoelectric control system for supplying high frequency voltages to the composite film. This would allow for the study of the hysteresis loop associated with the PVDF films and a full characterization of their piezoelectric properties.

Key improvements can be made to the processing of these films in the future by combining the carbon nanotube infused composites with lessons learned from processing the neat composite at elevated temperatures. If this study is undertaken it will be necessary to re-evaluate the crystal structure and morphology of the film to ensure the  $\beta$  phase is still present, because thermal history can greatly affect the formation of various crystal phases. It is suspected that depending on length of cure and temperature it may be possible to form  $\gamma$  phase PVDF polymorph, which also has piezoelectric attributes.

Chemical improvements may also yield gains in piezoelectric strength. It would be of interest to construct carbon nanotube reinforced polymer-polymer

composites using co-polymers of PVDF and evaluating the resulting performance. Likewise it may be possible to functionalize the carbon nanotubes to better interact with the PVDF. Because of the success of the multi-jet electrospinning described in Chapter 3, it may also be possible to blend two different polymers, each containing different nano-fillers. Because the Mark III electrospinning system allows for computer control of each injection port, it would be possible to vary the through thickness morphology of the electrospun films.

Another very interesting set of work is to evaluate other applications for high carbon nanotube reinforced sub-percolation threshold composites. In fuel cells, for example, the polymer Nafion is used as a proton exchange membrane placed between both electrodes. A common problem with Nafion membranes in fuel cells is their poor stiffness and fatigue life – however Nafion must remain nonconductive for proper operation of the fuel cell. A composite similar to the one developed in this work could be used to integrate a high carbon nanotube content thereby significantly improving the stiffness and strength of the Nafion without altering its electrically insulative characteristics. It is very likely that similar applications of this composite architecture could be found in the energy industry for use with lithium ion battery cells.

The sub percolation threshold carbon nanotube reinforced polymer-polymer composite is a novel platform with very important benefits for improving the piezoelectric strength of PVDF, but is also a strong candidate for many other applications requiring the benefits of carbon nanotube reinforcement without the typically imparted conductivity.

## REFERENCES

- [1] Zhang S, Zhang N, Huang C, Ren K, Zhang QM. Microstructure and Electromechanical Properties of Carbon Nanotube/ Poly(vinylidene fluoride—trifluoroethylene—chlorofluoroethylene) Composites. *Adv Mater* 2005;17:1897–901. doi:10.1002/adma.200500313.
- [2] Laxminarayana K. Functional Nanotube-based Textiles: Pathway to Next Generation Fabrics with Enhanced Sensing Capabilities. *Text Res J* 2005;75:670–80. doi:10.1177/0040517505059330.
- [3] Lucibella M. This Month In Physics History. *Am Phys Soc* n.d. <http://www.aps.org/publications/apsnews/201403/phy> (accessed April 1, 2015).
- [4] Curie J, Curie P. Development, via compression, of electric polarization in hemihedral crystals with inclined faces. *Bull La Soc Minerol Fr* 1880;24:90–3.
- [5] Lippman G. Principal of the conservation of electricity. *Comptes Rendus* 1881;93:1137–40.
- [6] Curie J, Curie P. Contractions and expansions produced by voltages in hemihedral crystals with inclined faces. *Comptes Rendus* 1881:1137–40.
- [7] Haertling GH. Ferroelectric Ceramics: History and Technology. *J Am Ceram Soc* 1999;82:797.
- [8] Wilson AJC. Piezoelectric properties of wood by V. A. Bazhenov. *Acta Crystallogr* 1963;16:235–235. doi:10.1107/S0365110X63000645.
- [9] Kawai H. The piezoelectricity of poly (vinylidene fluoride). *Jpn J Appl Phys* 1969;975.
- [10] Lyshevski S. *MEMS and NEMS: Systems, Devices, and Structures*. 1st ed. CRC Press; 2002.



- [11] Spreafico M, Cojocaru P. PVDF Latex As a Binder for Positive Electrodes in Lithium-Ion Batteries. Ind ... 2014.
- [12] Aslan M, Weingarth D, Jäckel N, Atchison JS, Grobelsek I, Presser V. Polyvinylpyrrolidone as binder for castable supercapacitor electrodes with high electrochemical performance in organic electrolytes. J Power Sources 2014;266:374–83. doi:10.1016/j.jpowsour.2014.05.031.
- [13] Summers F, Mason R, Ehrenshaft M. Development of immunoblotting techniques for DNA radical detection. Free Radic Biol Med 2013;56:64–71. doi:10.1016/j.freeradbiomed.2012.10.550.
- [14] Lang SB, Muensit S. Review of some lesser-known applications of piezoelectric and pyroelectric polymers. Appl Phys A 2006;85:125–34. doi:10.1007/s00339-006-3688-8.
- [15] Scheinbeim JI, Chung KT, Pae KD, Newman B a. The dependence of the piezoelectric response of poly(vinylidene fluoride) on phase-I volume fraction. J Appl Phys 1979;50:6101. doi:10.1063/1.325779.
- [16] Sessler GM. Piezoelectricity in polyvinylidene fluoride. J Acoust Soc Am 1981;70:1596–608.
- [17] Hasegawa R, Takahashi Y, Chatani Y, Tadokoro H. Crystal structures of three crystalline forms of poly (vinylidene fluoride). Polym J 1972.
- [18] Li M, Wondergem HJ, Spijkman M-J, Asadi K, Katsouras I, Blom PWM, et al. Revisiting the  $\delta$ -phase of poly(vinylidene fluoride) for solution-processed ferroelectric thin films. Nat Mater 2013;12:433–8. doi:10.1038/nmat3577.
- [19] Gregorio R. Effect of crystalline phase , orientation and temperature on the dielectric properties of poly ( vinylidene fluoride ) ( PVDF ) 1999;4:4489–500.
- [20] Davis GT, McKinney JE, Broadhurst MG, Roth SC. Electric-field-induced phase changes in poly(vinylidene fluoride). J Appl Phys 1978;49:4998. doi:10.1063/1.324446.
- [21] T Kaura, R Nath MMP. Simultaneous stretching and corona poling of PVDF films. J Appl Phys 1990;24:1848–52.

- [22] Hasegawa R, Kobayashi M, Tadokoro H. Molecular conformation and packing of poly (vinylidene fluoride). Stability of three crystalline forms and the effect of high pressure. *Polym J* 1972.
- [23] Gregorio R. Determination of the  $\alpha$ ,  $\beta$ , and  $\gamma$  crystalline phases of poly(vinylidene fluoride) films prepared at different conditions. *J Appl Polym Sci* 2006;100:3272–9. doi:10.1002/app.23137.
- [24] Satapathy S, Gupta PK, Pawar S, Varma KBR. Crystallization of  $\beta$  - phase Poly ( vinylidene fluoride ) films using dimethyl sulfoxide ( DMSO ) solvent and at suitable annealing condition n.d.:1–18.
- [25] Tao M, Liu F, Ma B, Xue L. Effect of solvent power on PVDF membrane polymorphism during phase inversion. *Desalination* 2013;316:137–45. doi:10.1016/j.desal.2013.02.005.
- [26] Chang J, Dommer M, Chang C, Lin L. Piezoelectric nanofibers for energy scavenging applications. *Nano Energy* 2012;1:356–71. doi:10.1016/j.nanoen.2012.02.003.
- [27] Huang S, Yee WA, Tjiu WC, Liu Y, Kotaki M, Boey YCF, et al. Electrospinning of polyvinylidene difluoride with carbon nanotubes: synergistic effects of extensional force and interfacial interaction on crystalline structures. *Langmuir* 2008;24:13621–6. doi:10.1021/la8024183.
- [28] Ramaratnam A. Reinforcement of Piezoelectric Polymers with Carbon Nanotubes: Pathway to Next-generation Sensors. *J Intell Mater Syst Struct* 2006;17:199–208. doi:10.1177/1045389X06055282.
- [29] Dillon DR, Tenneti KK, Li CY, Ko FK, Sics I, Hsiao BS. On the structure and morphology of polyvinylidene fluoride–nanoclay nanocomposites. *Polymer (Guildf)* 2006;47:1678–88. doi:10.1016/j.polymer.2006.01.015.
- [30] Thostenson E, Li C, Chou T. Nanocomposites in context. *Compos Sci Technol* 2005;65:491–516. doi:10.1016/j.compscitech.2004.11.003.
- [31] Thostenson E, Chou T. Processing-structure-multi-functional property relationship in carbon nanotube/epoxy composites. *Carbon N Y* 2006;44:3022–9. doi:10.1016/j.carbon.2006.05.014.

- [32] Li C, Thostenson E, Chou T. Sensors and actuators based on carbon nanotubes and their composites: A review. *Compos Sci Technol* 2008;68:1227–49. doi:10.1016/j.compscitech.2008.01.006.
- [33] Thostenson ET, Ziaee S, Chou T-W. Processing and electrical properties of carbon nanotube/vinyl ester nanocomposites. *Compos Sci Technol* 2009;69:801–4. doi:10.1016/j.compscitech.2008.06.023.
- [34] Sandler JKW, Kirk JE, Kinloch IA, Shaffer MSP, Windle AH. Ultra-low electrical percolation threshold in carbon-nanotube-epoxy composites. *Polymer (Guildf)* 2003;44:5893–9. doi:10.1016/S0032-3861(03)00539-1.
- [35] Li C, Thostenson ET, Chou T-W. Effect of nanotube waviness on the electrical conductivity of carbon nanotube-based composites. *Compos Sci Technol* 2008;68:1445–52. doi:10.1016/j.compscitech.2007.10.056.
- [36] Gao L, Thostenson ET, Zhang Z, Chou T-W. Sensing of Damage Mechanisms in Fiber-Reinforced Composites under Cyclic Loading using Carbon Nanotubes. *Adv Funct Mater* 2009;19:123–30. doi:10.1002/adfm.200800865.
- [37] Gao L, Chou T-W, Thostenson ET, Zhang Z. A comparative study of damage sensing in fiber composites using uniformly and non-uniformly dispersed carbon nanotubes. *Carbon N Y* 2010;48:3788–94. doi:10.1016/j.carbon.2010.06.041.
- [38] Owens F, Jayakody J, Greenbaum S. Characterization of single walled carbon nanotube: Polyvinylene difluoride composites. *Compos Sci Technol* 2006;66:1280–4. doi:10.1016/j.compscitech.2005.10.027.
- [39] Almasri A, Ounaies Z, Kim YS, Grunlan J. Characterization of Solution-Processed Double-Walled Carbon Nanotube/Poly(vinylidene fluoride) Nanocomposites. *Macromol Mater Eng* 2008;293:123–31. doi:10.1002/mame.200700229.
- [40] Li Y, Yan L, Shrestha R, Yang D, Ounaies Z, Irene E. A study of the optical and electronic properties of poly (vinylidene fluoride–trifluoroethylene) copolymer thin films. *Thin Solid Films* 2006;513:283–8. doi:10.1016/j.tsf.2006.01.058.
- [41] Doshi J, Reneker DH. Electrospinning process and applications of electrospun fibers. *J Electrostat* 1995;35:151–60.

- [42] Taylor G. Disintegration of Water Drops in an Electric Field. *Proc R Soc A Math Phys Eng Sci* 1964;280:383–97. doi:10.1098/rspa.1964.0151.
- [43] Deitzel J. Controlled deposition of electrospun poly(ethylene oxide) fibers. *Polymer (Guildf)* 2001;42:8163–70. doi:10.1016/S0032-3861(01)00336-6.
- [44] Eda G, Shivkumar S. Bead-to-fiber transition in electrospun polystyrene. *J Appl Polym Sci* 2007;106:475–87. doi:10.1002/app.
- [45] Huang Z. A review on polymer nanofibers by electrospinning and their applications in nanocomposites. *Compos Sci Technol* 2003;63:2223–53. doi:10.1016/S0266-3538(03)00178-7.
- [46] Kalayci VE, Patra PK, Kim YK, Ugbolue SC, Warner SB. Charge consequences in electrospun polyacrylonitrile (PAN) nanofibers. *Polymer (Guildf)* 2005;46:7191–200. doi:10.1016/j.polymer.2005.06.041.
- [47] He J-H, Wan Y-Q. Allometric scaling and instability in electrospinning. *Int J Nonlinear Sci Numer Simul* 2004;5:243–525.
- [48] Reneker DH, Yarin AL, Fong H, Koombhongse S. Bending instability of electrically charged liquid jets of polymer solutions in electrospinning. *J Appl Phys* 2000;87:4531. doi:10.1063/1.373532.
- [49] Choi SW, Kim JR, Ahn YR, Jo SM, Cairns EJ. Characterization of Electrospun PVdF Fiber-Based Polymer Electrolytes. *Chem Mater* 2007;19:104–15. doi:10.1021/cm060223+.
- [50] Wang YR, Zheng JM, Ren GY, Zhang PH, Xu C. A flexible piezoelectric force sensor based on PVDF fabrics. *Smart Mater Struct* 2011;20:045009. doi:10.1088/0964-1726/20/4/045009.
- [51] Gopal R, Kaur S, Ma Z, Chan C, Ramakrishna S, Matsuura T. Electrospun nanofibrous filtration membrane. *J Memb Sci* 2006;281:581–6. doi:10.1016/j.memsci.2006.04.026.
- [52] Wang X, Wang W, Li X, Carlberg B. Investigation of dielectric strength of electrospun nanofiber based thermal interface material. ... , 2007 HDP'07 ... 2007.

- [53] Xie X, Mai Y, Zhou X. Dispersion and alignment of carbon nanotubes in polymer matrix: A review. *Mater Sci Eng R Reports* 2005;49:89–112. doi:10.1016/j.mser.2005.04.002.
- [54] Capiati NJ, Porter RS. The concept of one polymer composites modelled with high density polyethylene. *J Mater Sci* 1975;10:1671–7. doi:10.1007/BF00554928.
- [55] Pornnimit B, Ehrenstein GW. Extrusion of self-reinforced polyethylene. *Adv Polym Technol* 1991;11:91–8. doi:10.1002/adv.1991.060110202.
- [56] Bigg DM, Smith EG, Epstein MM, Fiorentino RJ. High modulus semi-crystalline polymers by solid state rolling. *Polym Eng Sci* 1982;22:27–33. doi:10.1002/pen.760220105.
- [57] Ward IM. Developments in oriented polymers, 1970–2004. *Plast Rubber Compos* 2004;33:189–94. doi:10.1179/174328904X4864.
- [58] Advani S, Sozer M. *Process Modeling in Composites Manufacturing*. 2nd ed. CRC Press; 2010.
- [59] Thostenson ET, Chou T-W. Aligned multi-walled carbon nanotube-reinforced composites: processing and mechanical characterization. *J Phys D Appl Phys* 2002;35:L77–80. doi:10.1088/0022-3727/35/16/103.
- [60] Bruker-AXS. TOPAS: Total Pattern Analysis Software 2011. [http://www.bruker.com/fileadmin/user\\_upload/8-PDF-Docs/X-rayDiffraction\\_ElementalAnalysis/XRD/Flyers/TOPAS\\_Flyer\\_DOC-H88-EXS013\\_V2\\_en\\_high.pdf](http://www.bruker.com/fileadmin/user_upload/8-PDF-Docs/X-rayDiffraction_ElementalAnalysis/XRD/Flyers/TOPAS_Flyer_DOC-H88-EXS013_V2_en_high.pdf).
- [61] Martins P, Lopes a. C, Lanceros-Mendez S. Electroactive phases of poly(vinylidene fluoride): Determination, processing and applications. *Prog Polym Sci* 2014;39:683–706. doi:10.1016/j.progpolymsci.2013.07.006.
- [62] Kuffel E, Zaengl W. *High Voltage Engineering Fundamentals*. Pergamon Press; n.d.
- [63] Peek FW. *Dielectric Phenomena in High Voltage Engineering*. 1st ed. McGraw Hill; 1929.
- [64] Arora R, Mosch W. *High Voltage and Electrical Insulation Engineering*. Wiley IEEE Press; 2011.

- [65] Fothergill JC. Electrical Degredation and Breakdown in Polymers. P. Peregrinus; 1992.
- [66] Furukawa T. Ferroelectric properties of vinylidene fluoride copolymers. Phase Transitions 1989;18:143–211. doi:10.1080/01411598908206863.

## **Appendix A**

### **EQUIPMENT DESIGN**

In order to manufacture and test the electrospun carbon nanotube reinforced polymer-polymer composite, several custom pieces of equipment were necessary for production of the electrospun fibers and for high voltage testing of the finished samples.

#### **A.1 Electrospinning Apparatus**

There were several iterations in the design of the electrospinning apparatus. The first (Mark I) electrospinning system was very simple; It included a grounded collection platform, a single high voltage power supply, and a jig used to hold the injection needle (see Figure A.1). These are the most basic components required of an electrospinning system.



Figure A.1     Mark I, very rudimentary electrospinning apparatus

The Mark II was the first major improvement in the electrospinning system. An adjustable scaffold allowed for changing the distance between the collector and the injection needles. The needles themselves were held on carriages so the distance between both needles could be adjusted (see Figure A.2). Instead of a single power supply, another was added of opposite polarity. Here each injection needle had a positive voltage applied, the collection plate had a negative voltage applied, and the ground was attached to a faraday cage which was placed around the electrospinning apparatus in order to create a stable ground (see Figure A.3). This setup reduces ground interference (ground points in the nearby environment attracting charged fibers) and allows for consistent ground plane tuning, which improves electrospinning consistency and assists in multi-jet electrospinning. Solution is fed using a pair of NE-1000X syringe pumps and high voltage is provided by a pair of Gamma HV ES-30 units; all of these components are wired to a NI-USB6000 data acquisition board for control and data acquisition via an RS-232 connection.

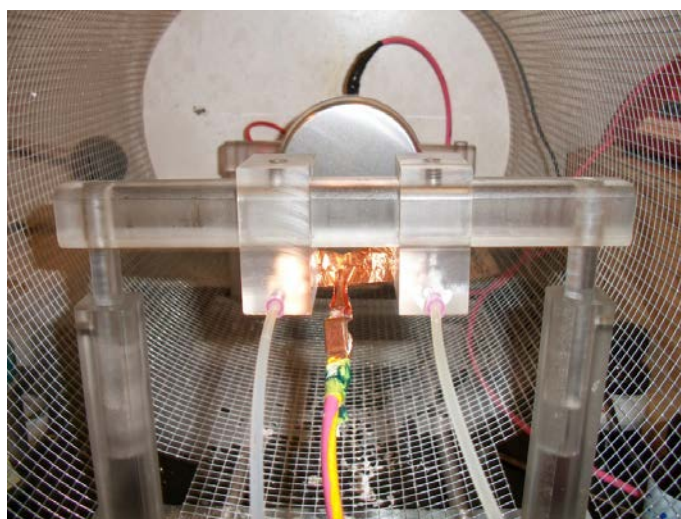


Figure A.2 Carriages for electrospinning injection needles





Figure A.3 Mark II electrospinning apparatus with Faraday cage

The Mark III system was a significant improvement on the Mark II system. The entire electrospinning apparatus was enclosed in a transparent polycarbonate environmental chamber (see Figure A.4). A conditioning system was engineered to condition air from the facility after which it was regulated (pressure), desiccated (negation of humidity), heated (optional), and the volume flow rate was adjusted (see Figure A.5). After this the air was fed into a porous base panel which allowed it to diffuse and flow evenly upwards through the chamber. The air was allowed to escape through a vent port in the ceiling of the chamber, where it was plumbed into the fume hood for safe removal. An Omega HX94 sensor was installed in the roof of the chamber in order to gather real time data on humidity and temperature inside the chamber.

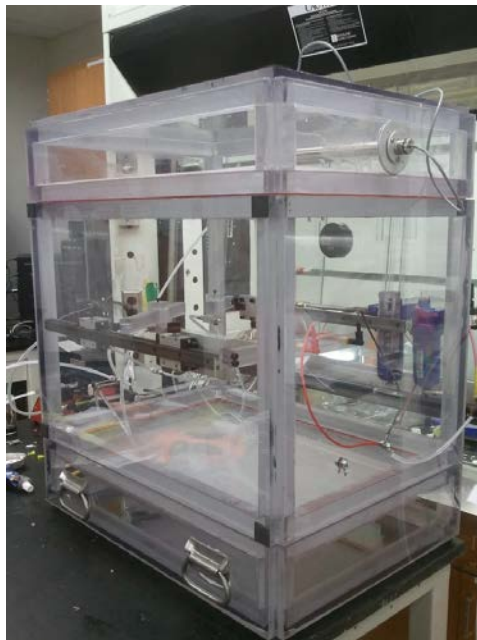


Figure A.4 Polycarbonate environmental chamber enclosing Mark III electrospinning system

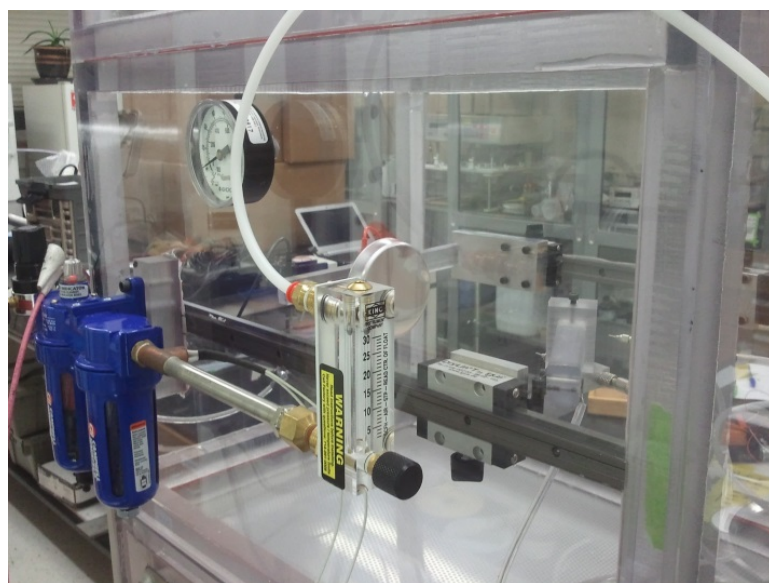


Figure A.5 Desiccation, heating, and air flow regulation in support of the Mark III electrospinning system

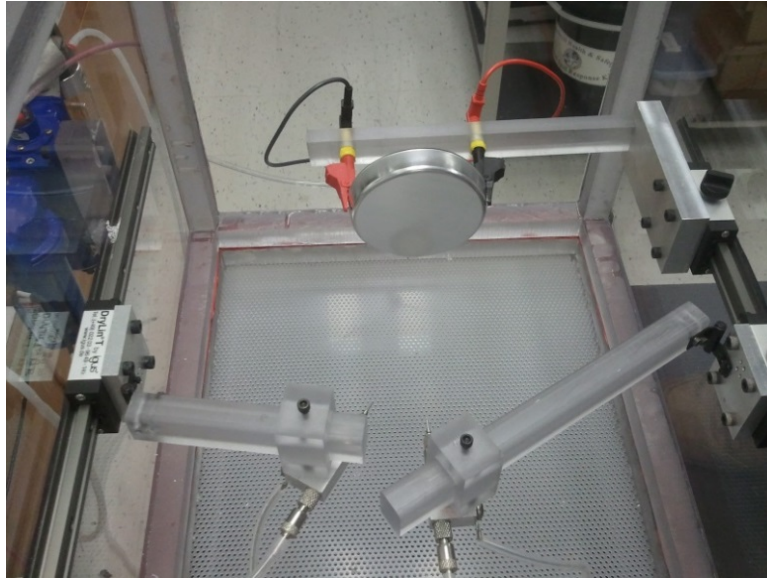


Figure A.6 The Mark III electrospinning system is equipped with articulated arms for injection needles held to the chamber by gantry sliders. The collection plate is also suspended by the gantry system and is fully adjustable

In order to provide the greatest degree of flexibility possible, the Mark III was equipped with a highly modular internal gantry system. The collector plate was mounted off of a gantry arm on one end of the chamber while the injection needles are both mounted on highly articulating slider arms on the opposite end. A ground plane ring was mounted in between the collector plate and injection needles to supplant the Faraday cage used in the Mark II system. The articulating arms for the injection needles each have 3 degrees of freedom - because the electric field is cylindrically symmetric this allows for every possible electric field configuration (see Figure A.6).

All electrical connections to the injection needles and collector plates were ported through the chamber wall using sealed stainless steel screws with washers to ensure a good electrical connection while maintaining a tight seal to maintain

good/sufficient environmental control. Pumping was similarly fed in to the chamber through a set of bulkheads in order to provide PVDF solution to the injection needles. This was accomplished with bored out and threaded steel bolts with luer lock connections screwed in to either end and sealed with thread sealant. They are easily removed and re-sealed for cleaning purposes.

As a further improvement to the Mark II system, a third (positive polarity) power supply is added in order to achieve a higher degree of control over the electric field. All three power supplies, the syringe pumps, and the HX94 temperature and humidity sensor interface with an NI-6000USB data acquisition system. A custom built Labview program monitors all variables and controls outputs for the system.

A further upgrade to the MARK III system is the addition of external infrared heating to allow for heating of the collector plate (see Figure A.7). Controlling the temperature of the collector plate allows for improved solvent evaporation as the fibers collect on the plate. This feature is expected to be especially useful for electrospinning polymer solutions where the solvent has a slower evaporation rate. This was developed for future work in the electrospinning of Nafion – a polymer commonly used as a proton exchange membrane in fuel cells.

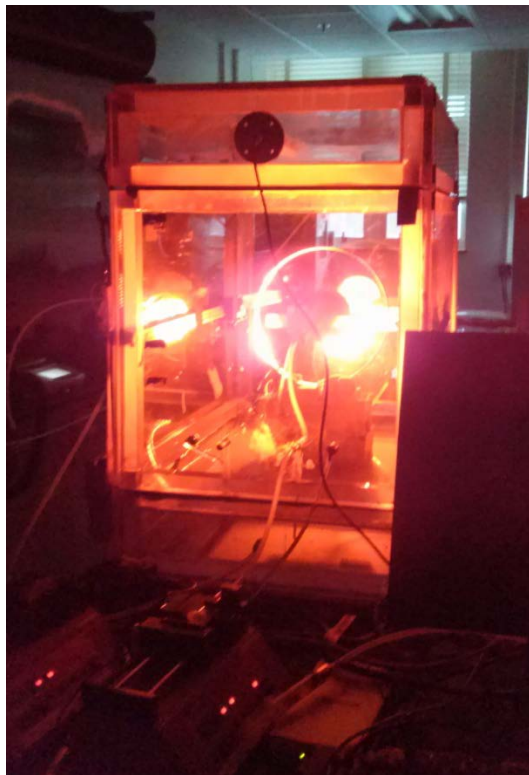


Figure A.7 External thermal management of the collector plate using infrared heat

## A.2 High Voltage and Poling

In order to impart piezoelectric properties on a PVDF film it must be polarized using a high strength electric field. The first system used for this was two simple flat electrodes placed on either face of the film. This worked well for neat PVDF films purchased directly in their rolled state; however for solution cast and electrospun films the electrode system shorted out rapidly. The Gen 1 high voltage system was designed to solve some of the problems associated with poling (see Figure A.8). A pair of precision machined aluminum electrodes was engineered to sandwich a pair of Teflon frames. The Teflon frames were integrated with a boss and pocket system which fit together with a slight offset, this way a plastic feeler gauge could be placed in the

pocket to control electrode displacement. This would allow for precise control over the distance between electrodes, and concurrently accurate control and measure of electric field strength.

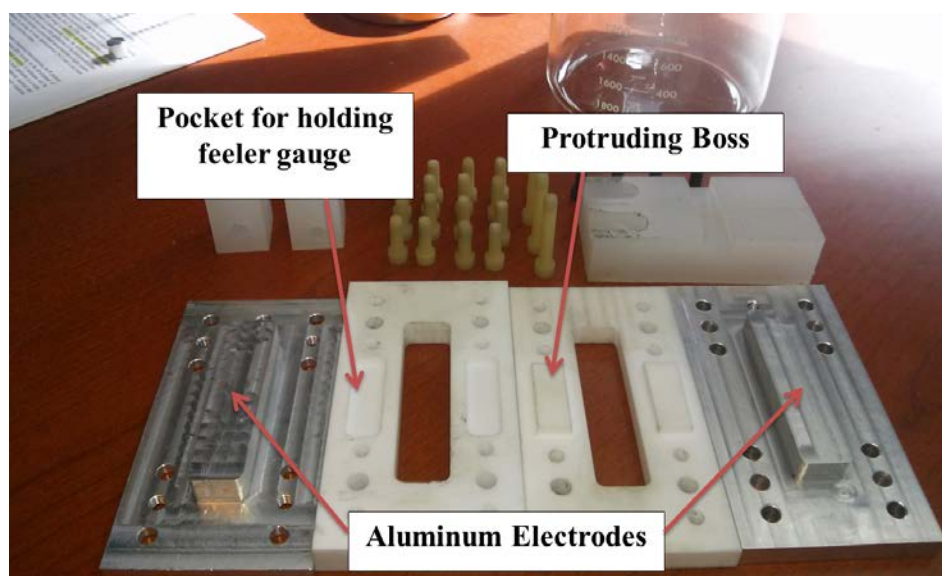


Figure A.8 High Voltage system, engineered to precisely control the distance between both electrodes for accurate measurement and control of electric field strength

This system, once assembled, was suspended in a mineral oil bath which could be heated for thermal management (see Figure A.9). It was hypothesized that the high dielectric strength of the oil would prevent corona discharge and premature short circuit when poling material. However, the oils that were trialed were not of a high enough dielectric strength or purity and consistently failed.



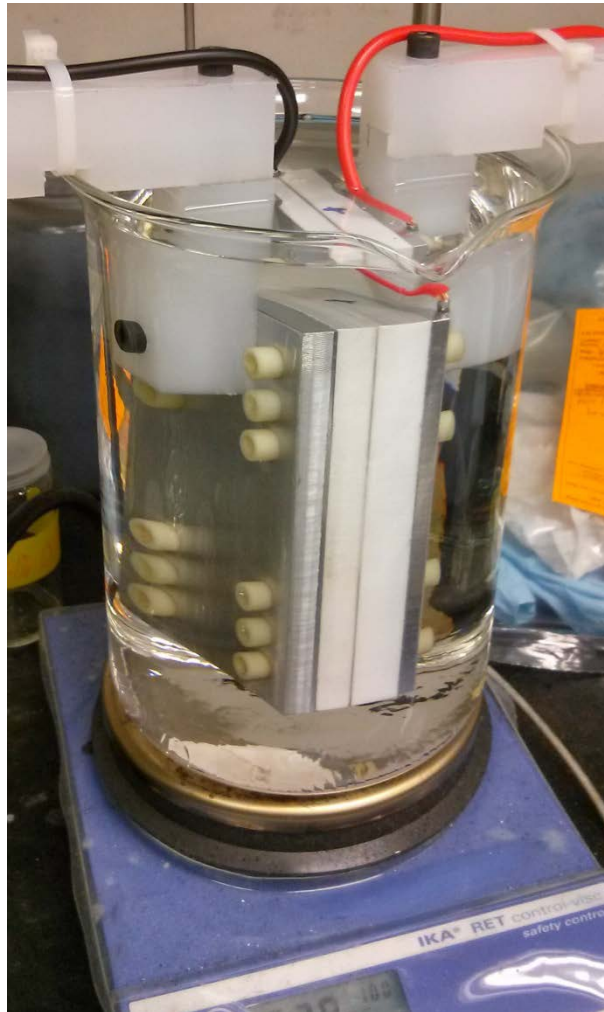


Figure A.9 High Voltage system suspended in oil for thermal management and prevention of short circuits

The Gen 2 system was designed after a great deal of study in high voltage physics. As a result, it was built to accommodate and measure all three modes of failure: corona discharge, electrical surface tracking, and dielectric breakdown. It was engineered to have two configurations – an elevated configuration which would suspend samples in the air for dielectric breakdown testing, corona discharge analyses,

and poling of PVDF (see Figure A.10) as well as a lowered position informed by standard methods of testing electrical surface tracking (see Figure A.11).

In order to reduce the risks associated with high voltage, the Gen 2 system was constructed from carefully machined GPO3 – an electrical grade fiberglass composite which is designed specifically for higher voltage applications. The electrodes were machined from aluminum with flat modular ends for dielectric breakdown and poling and pointed ends for use in corona discharge and electrical surface tracking studies. The base platform (also machined from GPO3) is built on a sliding platform to accommodate multiple tests on the same film specimen. All fillets were carefully designed to further reduce the risks inherent in operation with high voltages.

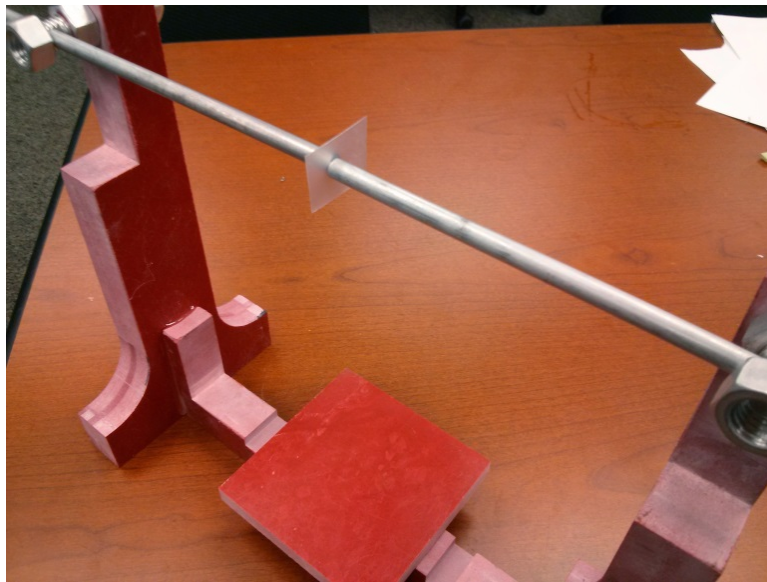


Figure A.10 Gen 2 high voltage system positioned horizontally for dielectric breakdown, corona discharge or poling



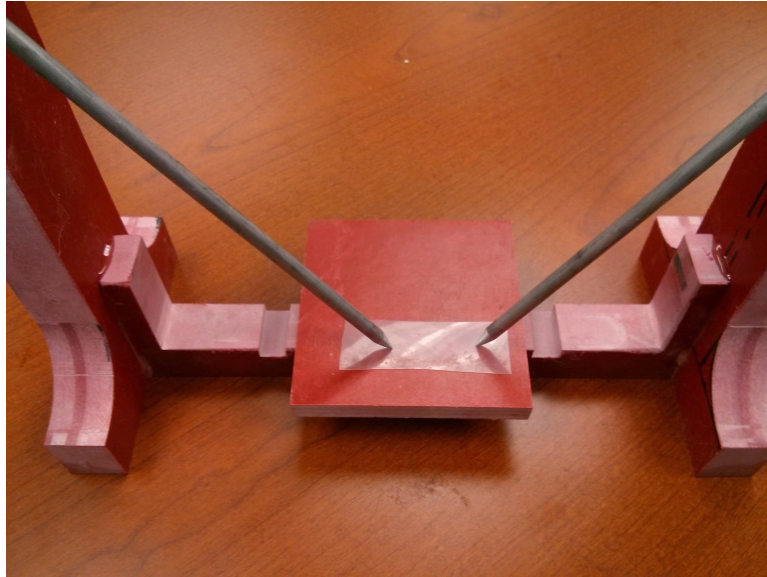


Figure A.11 Gen 2 high voltage system positioned for electrical surface tracking test

## **Appendix B**

### **DEVELOPMENT OF COMPUTER VISION FOR FIBER IMAGE ANALYSIS**

There are a few ways to geometric results (fiber diameter and orientation) of the electrospinning process – earlier research focused heavily on manual measurements; however, for future work a process was developed in order to identify the metrics through an image analyses algorithm. This avoids the pitfalls of computer assisted human based measurements: there is a component of human error and error due to fatigue after a great number of measurements, it is very time consuming, and there is an artificial sub pixel accuracy which can be deceptive. This algorithm was coded in MATLAB® using the image analyses toolkit.

Figure B.1 shows an example of the input image used for the image processing and analytics software. The image file has two components – the image itself, as well as the metadata that accompanies it. The metadata includes all of the information about the SEM as well as different settings such as electron voltage, working distance, magnification, and most importantly pixel size.

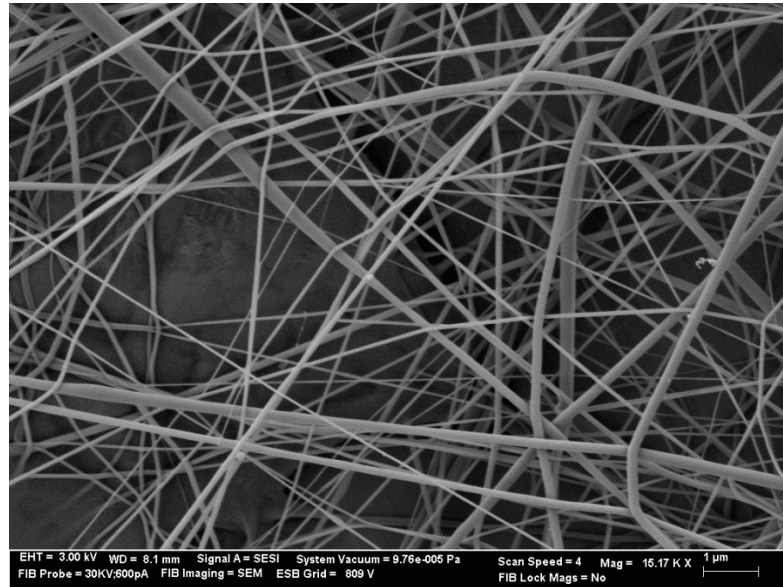


Figure B.1 Example SEM micrograph used as input for the computer vision code

The first part of the analyses code parses the metadata stored in the header of the TIFF file and extracts the pixel size.

```
file = fopen(filename);
tline = fgets(file);
k = strfind(tline, 'Pixel Size');
while isempty(k)
    tline = fgets(file);
    k = strfind(tline, 'Pixel Size');
end
fclose(file);
[number unit] = strtok(tline, 'Pixel Size =');
number = str2double(number);
```

This begins the basis for interpreting the image numerically. Next, a histogram is formed which represents the number of pixels for each contrast ratio and is critical to further image analyses (see Figure B.2). It is an important basis for discovering the proper threshold for converting the grayscale image into a binary image so that more advanced algorithms can be used for feature detection.

```

Igray = mat2gray(Image);
I2 = reshape(Igray,1,numel(Igray));
[n, xout] = hist(I2,numel(Igray));
hist(I2, numel(Igray))
xlabel('pixel contrast level')
ylabel('number of pixels')
axis([0 1 0 1.5E4])

```

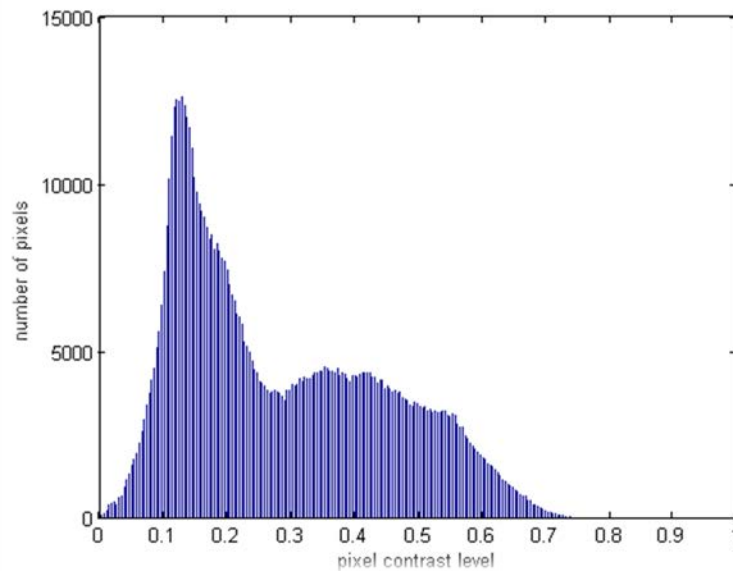


Figure B.2 Histogram generated from image

Next it's possible to find the appropriate roots by using simple mathematics.

Two arrays (Dplus and Dminus) both duplicate D, but Dplus is slid to the right.

Multiplying them together element wise reveals the roots where the derivative changes from negative to positive.

```

Dplus = D > 0;
Dminus = D < 0;
Dplus = [Dplus(2:end); 0];
Intercepts = Dplus .* Dminus;
n = (find(Intercepts));
level = xout(find(Intercepts));
hold on; plot(cont(n(1)),level(1),'o','color','r')

```

Figure B.3 shows the smoothed histogram derivative as well as the calculated first negative to positive y-intercept. This is the number that will be used for the thresholding. This means that the portion of the histogram to the right of it will be white (fibers) while the portion to the left is black (background). This was selected as a technique to replace the more typically used Cauchy edge detection because it was observed to be more efficient for the purposes of fiber detection.

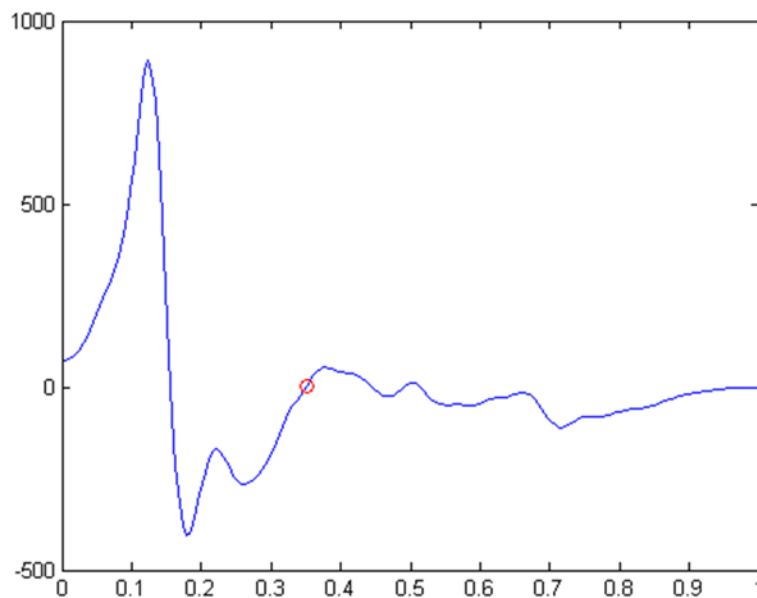


Figure B.3 Smoothed histogram derivative used for finding the correct threshold

Creating a shape image is now easy. Using the feature detected in the previous step as the threshold, and converting the image to black and white (Figure B.4). Next, find the perimeter of this image and use it as the edge map (Figure B.5).

```
BW = im2bw(Image, level(1));  
BW2 = im2double(BW);  
SHAPE = im2double(BW);  
EDG = bwperim(BW2);  
EDGE = +EDG;  
  
figure ; imshow(Image)  
figure ; imshow(BW2)  
figure ; imshow(EDGE)
```

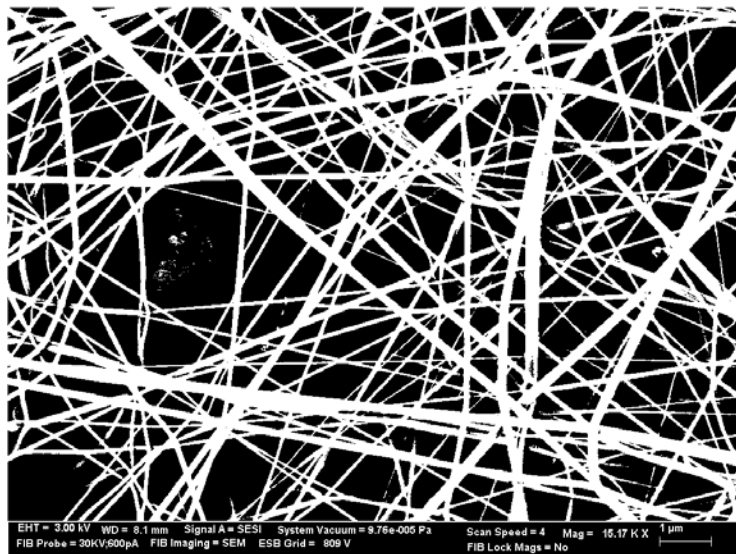


Figure B.4 Adaptive thresholding to convert to shape image

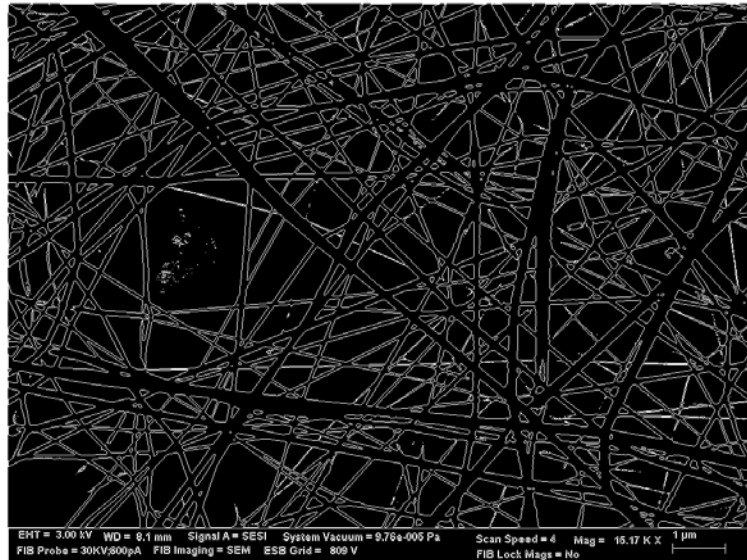


Figure B.5 Perimeter detection used to find edges in shape image

The next step is to subdivide the image into a grid. One measurement will be taken from each grid in order to compute the data. Both the edge image and the shape image are divided into a collection of cells so that all the spatial data is preserved.

Figure B.6 shows an example of one cell of data.

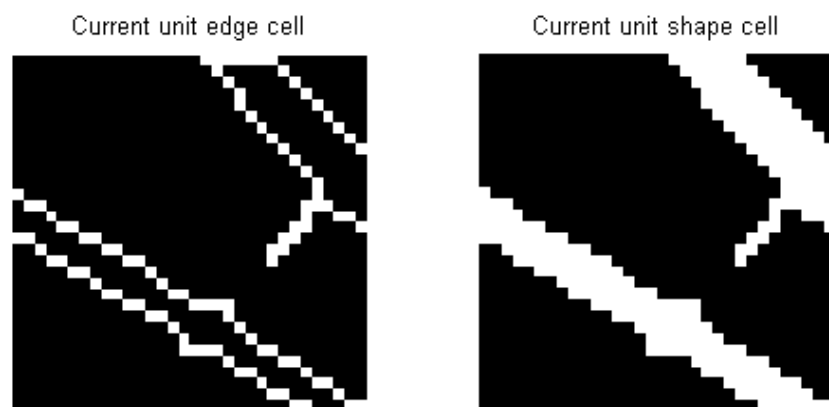


Figure B.6 Unit edge cell vs. unit shape cell

Each subcell is next analyzed. Before doing anything clever, the simpler cases are identified and discarded. If a particular cell doesn't have enough information in it to yield a good line, it is removed. This test removes any cells which are more than 90% empty.

Now that the image is prepared for feature detection the characteristics that are being detected must be identified. In this case the goal is to detect parallel lines and report their orientation and distance from one another. For the purpose of image analyses the standard description of a line  $y = mx + b$  tends to misbehave – when numerical error and round-off is introduced this mathematical characterization is not bounded, so it can generate infinities and zeros. Instead a parameterization is used such that:

$$y = \left(-\frac{\cos \theta}{\sin \theta}\right)x + \frac{\rho}{\sin \theta} \quad \text{A.1}$$

This is easily illustrated in Figure B.7

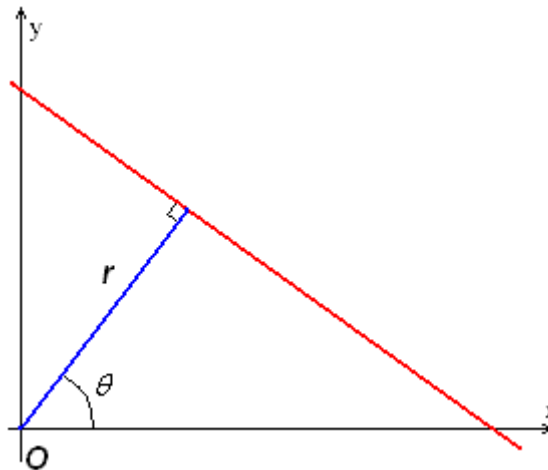


Figure B.7 Illustration of line parameterization



Next, every possible line is matched with the above edge bitmap. Every white pixel lying on any  $R-\theta$  line is added into an "accumulator bin" and plotted as a grayscale brightness in  $R-\theta$  space (more commonly referred to as "Hough Space"). The result in Hough Space can easily be visualized as in Figure B.8.

```
B1 = (sum(sum(shape)) > .1*numel(shape));
B2 = (sum(sum(shape)) < .5*numel(shape));
B = B1 && B2;
if B
    h3 = figure;
    [H, T, R] = hough(edge);
    P = houghpeaks(H, 8, 'threshold', ceil(0.1*max(H(:)))));
    theta = T(P(:,2));
    rho = R(P(:,1));
    imshow(flipud(H), [], 'XData', T, 'YData', R, ...
            'InitialMagnification','fit');           % Plot Hough
Transform
    axis on; axis normal; hold on;                 % Configure plot
    plot(theta,-rho,'s', 'color','red');           % Plot peaks
```

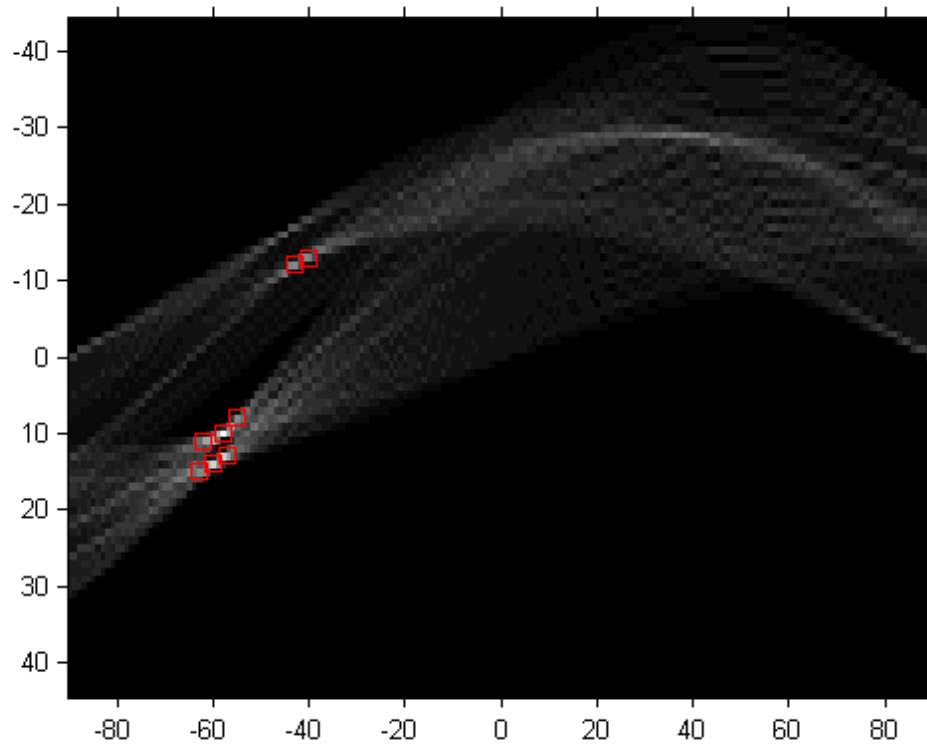


Figure B.8 Unit edge cell transformed into Hough Space and rendered

The peaks in the Hough Space represent the most powerful lines in the image. These points can be extracted and lines that correspond to them plotted. Next, the  $\theta$  and  $\rho$  values corresponding to each line can be extracted, as well as their midpoints and endpoints. This result is depicted in Figure B.9.

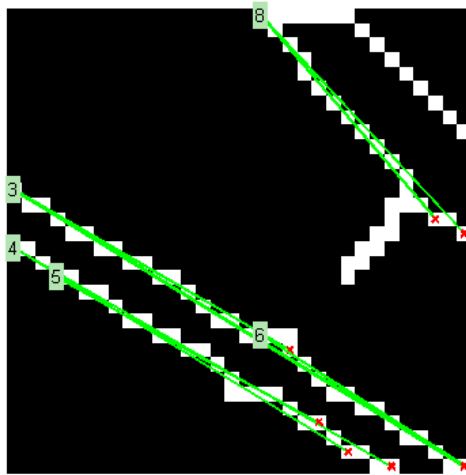


Figure B.9 Depiction of unit edge cell line detection

Next it needs to be determined which of these lines are the boundaries of the same fibers. This is a completely non-trivial problem, and requires some “clever mathematics”. Generally it would make sense to characterize the lines that had just been extracted, however this is notoriously difficult. Computers have a really hard time with Cartesian representation of lines, notably because depending on the line both the slope and y intercept can approach zero or infinity, making the system inherently unstable.

The solution then, is to complete as much of the analysis as possible in the Hough space. Any pair of lines who’s combination of  $\rho$  and  $\theta$  values are too close most likely represent the same physical line. Any line pairs who diverge too greatly are also not fiber candidates, Figure A.10 depicts this concept mathematically in a Hough space plot.

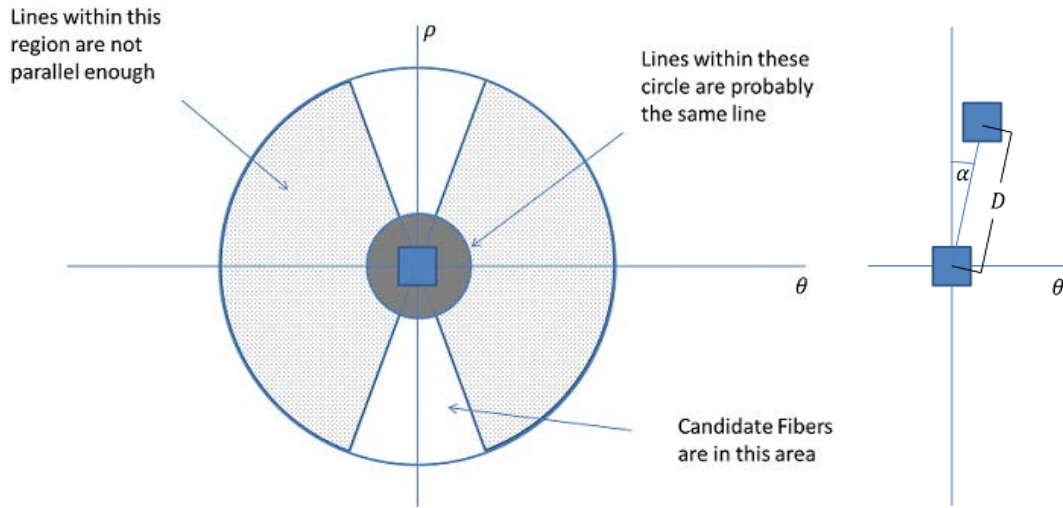


Figure B.10 Depiction of analyses for determining fiber candidates and graphical representation of new variables  $\alpha$  and  $D$

This is done by forming two difference matrices:

$$\Delta\Theta = \Delta\theta_{i-j} \quad \text{A.2}$$

$$\Delta P = \Delta\rho_{i-j} \quad \text{A.3}$$

Next, two new variables (see Figure A.10) are defined,  $\alpha$  and  $D$ , such that:

$$\alpha = \arctan \frac{\Delta P}{\Delta\Theta} \quad \text{A.4}$$

$$D = \sqrt{\Delta\Theta^2 + \Delta P^2} \quad \text{A.5}$$

The results can be filtered by  $D$  and  $\alpha$  values. For this analysis  $\alpha$  is allowed to deviate by 40 degrees in either direction and  $D$  is allowed to be anything larger than two pixels (this can be reduced to one depending on image magnification but if the image is high enough magnification 2 pixels is more appropriate.) The candidates are then organized into a matrix where their column and row numbers are their line

numbers. Boolean operators are processed using the above filters and the row and column numbers for the upper triangular portion are processed.

```
theta_difference = (repmat(THETA',1,length(THETA)) ...
    - repmat(THETA,length(THETA),1));
rho_difference = (repmat(RHO',1,length(RHO)) ...
    - repmat(RHO,length(RHO),1));
D = (theta_difference.^2 + rho_difference.^2).^5;
ALPHA = atan(theta_difference./rho_difference);
alpha_delta = 80;
D_min = 2;
D_max = 100;

Pizza = (abs(rad2deg(ALPHA)) < (alpha_delta/2));
Annulus = (D > D_min).*(D < D_max);
Candidates = Annulus.*Pizza;
[col row] = find(triu(Candidates) == 1);
k = 1;
```

Using the shape matrix cells, we can check for connectedness between any two lines. This is another custom algorithm which will be described more in detail later. The idea, however, is to check that any two lines have a path in the straight-line between them which is all fiber. This reduces errors due to the space in between fibers being falsely identified as fibers.

First solve the equation for the line which intersects the two. A simple matrix calculation  $Ax = b$  gives the resulting slope and intersect. Because of the quantized nature of this test however --- it isn't practical to use this representation of a line. We borrow the same hack we used before and parameterize it in terms of  $\rho$  and  $\theta$ .

```
lineA = [L1(1) 1; L2(1) 1];
lineB = [L1(2); L2(2)];
VEC = lineA\lineB;
SLOPE = VEC(1);
INTERSECT = VEC(2);
TT = acot(-SLOPE);
RR = INTERSECT*sin(TT);
```

Next, a line is constructed such that the "new line" in the same image space as the original cell. Create an appropriate mesh and build a new black and white image

containing the line (white in figure). Next mask the line to limit it to the range where it is between the midpoint of the two lines it intersects (red section in Figure B.11).

```
empty = zeros(size(shape));
[Xlength Ylength] = size(shape);
[XX, YY] = meshgrid(linspace(1,Xlength,Xlength),
linspace(1,Ylength,Ylength));

char = YY*sin(TT) + XX*cos(TT);
linematrix = (floor(char) == floor(RR));

XS = sort([L1(1) L2(1)]);
YS = sort([L1(2) L2(2)]);
Xzero = ((XX >= XS(1)).*(XX <= XS(2)));
Yzero = ((YY >= YS(1)).*(YY <= YS(2)));
ZeroMask = Xzero.*Yzero;
bool = linematrix.*ZeroMask;
figure; imshow(cat(3,linematrix,linematrix-bool,linematrix-bool), ...
'InitialMagnification','fit')
```

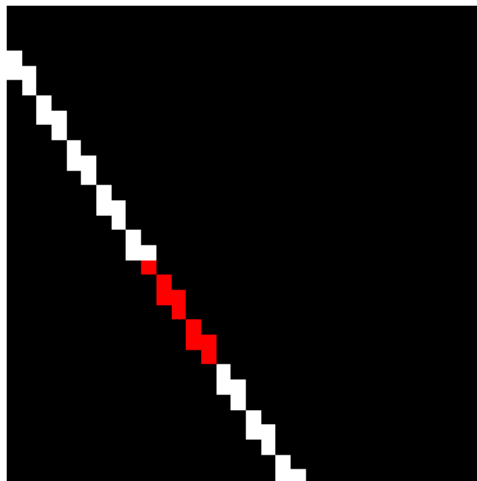


Figure B.11 Parameterized line (red) overlaid on unit edge cell

Subsequently the analysis can be done through some simple element wise boolean matrix operations. The boolean test checks if the line segment, when

multiplied by the black and white shape bitmap – still returns the original line segment matrix. If this is true (within tolerance, to account for overlap) the line pair passes the connectedness test. Figure B.12 shows each component. The blue shows the full constructed intersect line and the magenta shows the line segment with (a) showing a passing case (meaning a fiber was detected) and (b) showing a failing case (not a fiber).

```
test = (bool.*shape) == bool;
testsum = sum(sum(test));

if sum(sum(linematrix)) <= 1
    ANS = 0;
elseif testsum >= Xlength*Ylength - 2
    ANS = 1;
else
    ANS = 0;
end

figure
NI = cat(3, edge + bool, edge, edge + linematrix);
imshow(NI, 'InitialMagnification','fit')
```

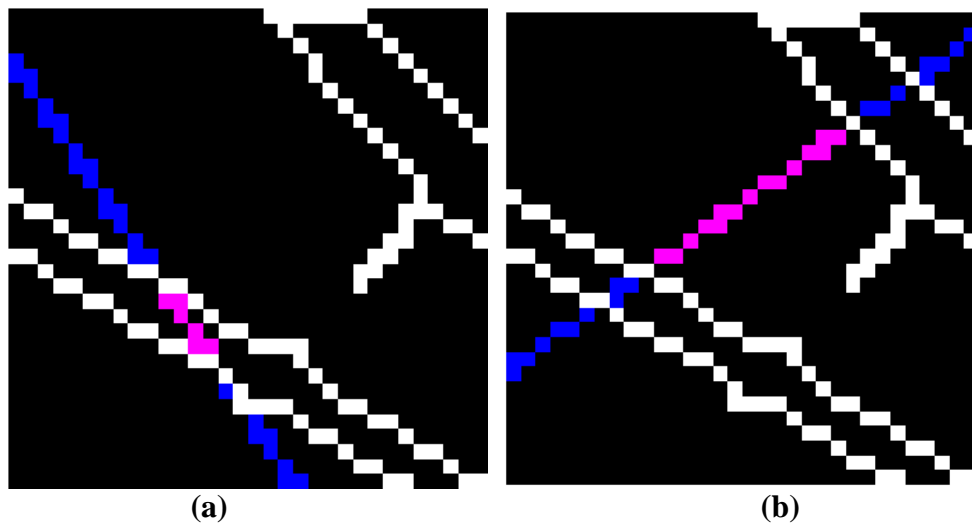


Figure B.12 Visualization of boolean test for connectedness. (a) shows a passing case while (b) shows a failing case.

Finally, the best fiber candidate, after all the filters, is measured by minimizing  $\alpha$ . This gives the two most parallel lines. The Hough space peaks for these fibers are identified and the fiber diameters and orientations can be fairly accurately approximated using the parameterized values:

$$r = |\rho_{peak1} - \rho_{peak2}| \quad A.6$$

$$\phi = \sqrt{\theta_{peak1} + \theta_{peak2}} \quad A.7$$

and the resulting lines can be plotted for visual verification (see Figure B.13).

Diameter and Angle are outputted for each cell.

```

if exist('col2')
    h5 = figure;
    imshow(shape, 'InitialMagnification','fit'); hold on;
    Evaluation = [col2' row2' diag(ALPHA(col2,row2))];
    [a b] = min(Evaluation(:,3));
    PEAK1 = col2(b);
    PEAK2 = row2(b);

    DIA(ii,jj) = abs(RHO(PEAK1) - RHO(PEAK2));
    ANGLE(ii,jj) = .5*(THETA(PEAK1) + THETA(PEAK2));
    xy = [lines(PEAK1).point1; lines(PEAK1).point2];
    plot(xy(:,1),xy(:,2),'LineWidth',2,'Color','green');
    xy = [lines(PEAK2).point1; lines(PEAK2).point2];
    plot(xy(:,1),xy(:,2),'LineWidth',2,'Color','green');
else
    disp('no proper enough fibers detected')
end
else
    disp('number of pixels in "shape" are less than 10% or greater
    than 50% of available pixels')
end
end

```



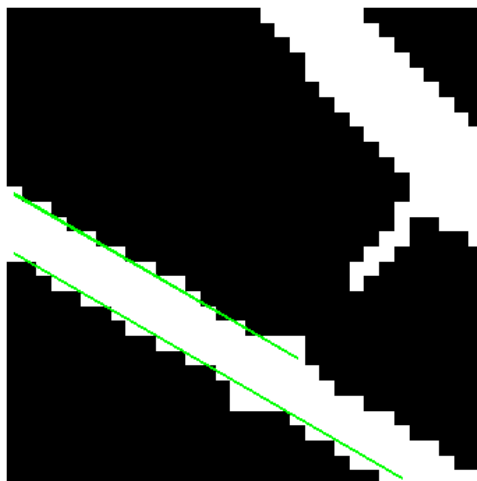


Figure B.13 Correct identification of lines overlaid over the unit shape cell

The process is then repeated for each grid cell until all the data are tabulated. Once collected a diameter histogram can be constructed, such as Figure B.14.

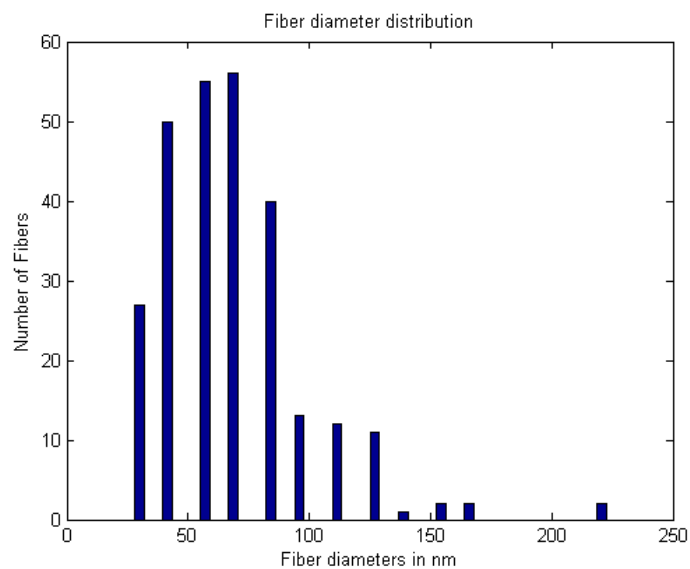


Figure B.14 Fiber diameter histogram as outputted by the computer vision code